Megathrust Heterogeneity, Crustal Accretion, and a Topographic Embayment in Western Nepal Himalaya: Insights from the Inversion of Thermochronological Data

Suoya Fan[1]; Michael A. Murphy[1]; David M. Whipp[2]; Joel E. Saylor[3]; Peter Copeland[1]; Andrew K. Hoxey[4]; Michael H. Taylor[4]; Daniel F. Stockli[5]

[1]Department of Earth and Atmospheric Sciences, University of Houston, Houston, Texas 77204, USA

[2]Institute of Seismology, Department of Geosciences and Geography, University of Helsinki, Helsinki, Finland

[3]Department of Earth, Ocean and Atmospheric Sciences, University of British Columbia, Vancouver, British Columbia, Canada

[4]Department of Geology, University of Kansas, Lawrence, Kansas 66045, USA

[5]Department of Geological Sciences, Jackson School of Geosciences, University of Texas at Austin, Austin, Texas 78712, USA

Corresponding author: Suoya Fan (sfan2@uh.edu)

Key Points:

- Thermochronologic data and thermokienmatic modeling results suggest a complex 3D geometry of the megathrust in the western Nepal Himalaya
- Crustal accretion along the mid-lower crustal ramp in the megathrust is a mechanism of maintaining the edge of a plateau-like landscape
- The development of the 3D megathrust geometry may have controlled the first-order evolution of an embayment and regional drainage system

Abstract

Between 81°30' E and 83°E the Himalayan range's "perfect" arcuate shape is interrupted by an embayment. We hypothesize that thrust geometry and duplexing along the megathrust at mid-lower crustal depths plays a leading role in growth of the embayment as well the southern margin of the Tibetan plateau. To test this hypothesis, we conducted thermokinematic modeling of published thermochronologic data from the topographic and structural embayment in the western Nepal Himalaya to investigate the three-dimensional geometry and kinematics of the megathrust at mid-lower crustal depths. Models that can best reproduce observed cooling ages suggest that the megathrust in the western Nepal Himalaya is best described as two ramps connected by a long flat that extends further north than in segments to the east and west. These models suggest that the high-slope zone along the embayment lies above the foreland limb of an antiformal crustal accretion zone on the megathrust with lateral and oblique ramps at mid-lower crustal depths. The lateral and oblique ramps may have initiated by ca. 10 Ma. This process may have controlled along-strike variation in Himalayan-plateau growth and therefore development of the topographic embayment. Finally, we analyze geological and morphologic features and propose an evolution model in which landscape and drainage systems across the central-western Himalaya evolve in response to crustal accretion at depth and the three-dimensional geometry of the megathrust. Our work highlights the importance of crustal accretion at different depths in orogenic-wedge growth and that the mid-lower crustal accretion determines the location of plateau edge.

1 Introduction

For large orogens, the roles of the geometry and kinematics of the megathrust in controlling strain accumulation and the feedback mechanisms between deformation and erosion are keys to understanding the growth of the orogenic wedge and the evolution of its morphology. The Himalayan orogenic wedge is a classical natural laboratory to study this, because it exhibits both along-strike consistency in first-order tectonic-morphologic framework and pronounced along-strike segmentation. Early studies show that the tectonostratigraphy, major shear zones, deformation styles, and morphologic features are generally continuous along the strike of the > 1500 km orogen (Heim and Gansser, 1939; Gansser, 1964; Le Fort, 1975; Burg and Chen, 1984; Pêcher, 1989; Yin, 2006) (Fig. 1). Along with these features, concentrated micro-seismicity, maximum horizontal strain rate, zones of high river gradient, and zones of high relief are interpreted to be collocated along a small circle or "perfect arc" (Seeber and Gornitz, 1983; Bendick and Bilham, 2001). This arc is interpreted to represent the active-uplift front of the high Himalaya based on geological, geophysical, and geomorphological observations and to mark the plateau margin, the transition between a taper-shaped outer wedge and inner-wedge plateau (Fan and Murphy, 2021 and references therein). It is thought to form through deformation associated with a mid-lower crustal ramp in the megathrust, which connects an upper-crustal flat below the outer wedge and a flat seismic reflector extending beneath Tibet (Hauck et al., 1998; Nábělek et al., 2009).

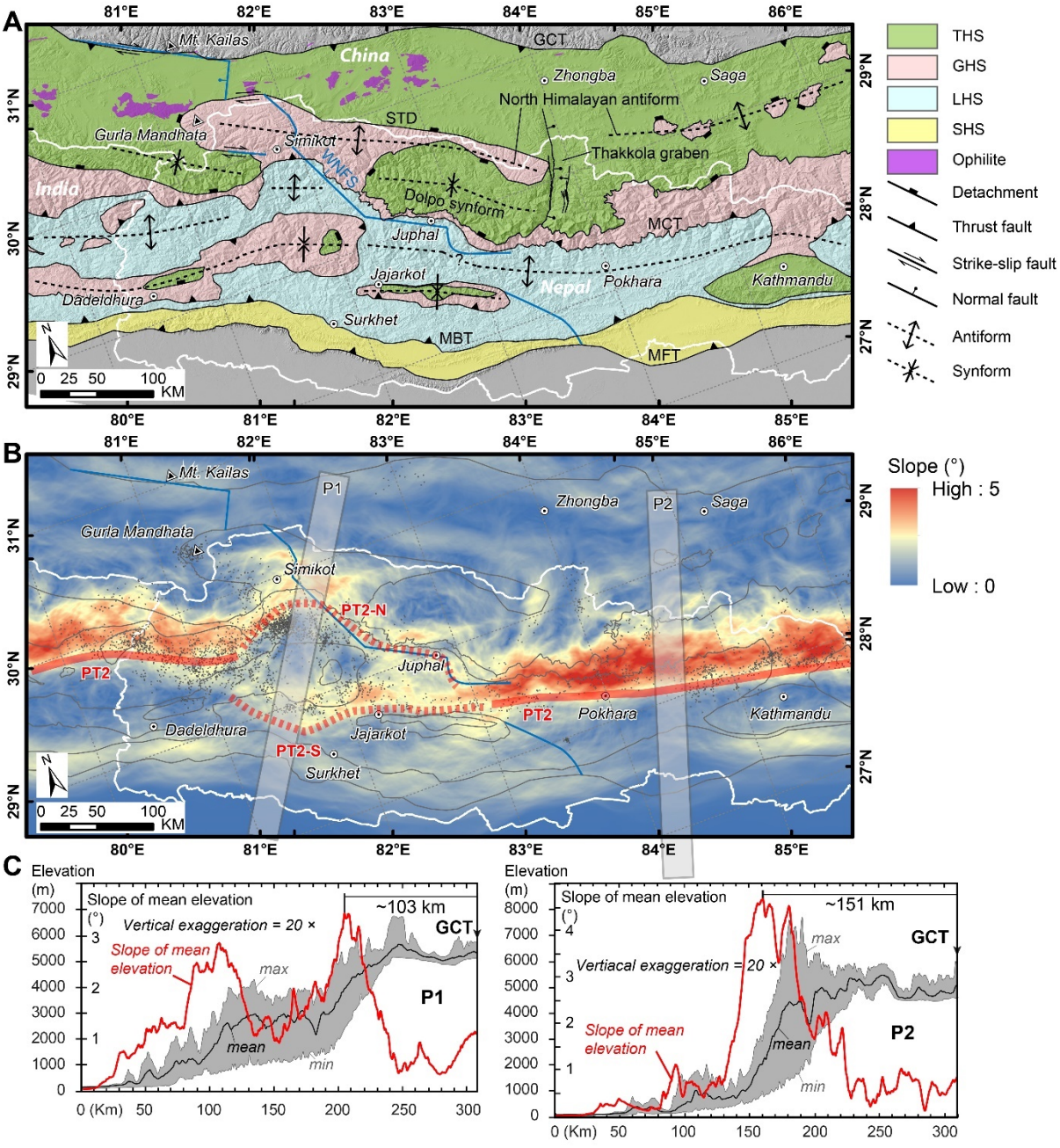

Figure 1 Geological map (A) and slope of mean elevation map (B) of central-western Nepal and adjacent areas and (C) topographic swath profiles and slope of mean elevation profiles of western and central Nepal Himalaya. Grey dots in (B) show earthquake hypocenters from 1995 to 2004, relocated by Ader et al. (2012). Gray lines in (B) are major faults shown in (A). Slope of mean elevation was calculated by first smoothing the topography by taking the mean within a 25 km moving window and then calculating the slope of the resulting grid. THS – Tethyan Himalayan Sequence; GHS – Greater Himalayan Sequence; LHS – Lesser Himalayan Sequence; SHS – Sub-Himalayan Sequence; GCT – Great Counter Thrust; STD – South Tibet Detachment; MCT – Main Central Thrust; MBT – Main Boundary Thrust; MFT – Main Frontal Thrust; WNFS – Western Nepal Fault System.

Megathrust kinematic models can be classified into three main groups (Fig. 2); (1) thrusting of the orogenic wedge over a crustal ramp (Gansser, 1964; Jackson and Bilham, 1994; Cattin and Avouac, 2000; Lavé and Avouac, 2001; Robert et al., 2009; Robert et al., 2011; Coutand et al., 2014; Elliott et al., 2016), (2) thrusting of the orogenic wedge over a crustal ramp accompanied by localized transfer of material from the footwall to hanging wall via duplexing or accretion (Avouac, 2003; Bollinger et al., 2004; Bollinger et al., 2006; Herman et al., 2010; Grandin et al., 2012; Cannon and Murphy, 2014; Adams et al., 2016; Landry et al., 2016; Stübner et al., 2018; Fan and Murphy, 2021), and (3) out-of-sequence thrusting (Harrison et al., 1997; Wobus et al., 2003; Hodges et al., 2004; Thiede et al., 2004; Thiede et al., 2005; Wobus et al., 2005; Wobus et al., 2006; Whipple et al., 2016) or a hybrid of out-of-sequence and duplex model (Morell et al., 2017). Besides the dispute over the kinematics controlling the active-uplift zone, an increasing number of studies challenge the notion of a "perfect arc" orogenic system with evidences of non-cylindricity in surface geology, wedge morphology, and the deep megathrust geometry (Duncan et al., 2003; Yin, 2006; Hetenyi et al., 2016; Cannon et al., 2018; Eugster et al., 2018; Dal Zilio et al., 2020a; Fan and Murphy, 2021). One pronounced deviation from the "perfect arc" shape of the Himalaya is the bifurcation of several features defining the active-uplift front in western Nepal Himalaya (Fig. 1) (Harvey et al., 2015). The northern branch of the bifurcation has been interpreted to represent the active-uplift zone, implying that there is a recession or embayment in the active-uplift front of the wedge (Cannon et al., 2018; Fan and Murphy, 2021). Some studies have ascribed this along-strike anomaly to an along-strike difference in the number and location of ramps in the Himalayan megathrust, the Main Himalayan Thrust (MHT) (Robert et al., 2011; Harvey et al., 2015; van der Beek et al., 2016; Fan and Murphy, 2021). This conceptual interpretation is consistent with the observation of a longer upper-crustal flat in the megathrust in western Nepal than in some other sectors (Subedi et al., 2018) and the pattern of microseismicity (Ader et al., 2012; Hoste-Colomer et al., 2018). However, different from the well-studied MHT upper-crustal flat and the structures above it in the outer wedge (DeCelles et al., 2020 and references therein), the geometry and kinematics of the MHT at aseismic slip depths in western Nepal are not well understood.

A better understanding of the geometry of the megathrust in western Nepal Himalaya is also crucial to assess seismic hazard in the region. Beneath a thickened continental crust, the downdip limit of the seismogenic zone along a megathrust should be located where the megathrust intersects the temperature-controlled transition between seismic and aseismic slip depths (Hyndman et al., 1997). The geometry of the megathrust therefore should be the determining factor for the along-strike variation in the location of the downdip limit of the seismogenic zone. The along-strike complexity of this limit in the Himalaya is implied by the heterogeneity shown in coupling models derived from geodetic data (Ader et al., 2012; Stevens and Avouac, 2015; Marechal et al., 2016; Jouanne et al., 2017; Li et al., 2018; Sreejith et al., 2018; Yadav et al., 2019; Dal Zilio et al., 2020a). The potential along-strike changes in the geometry of the MHT require the existence of lateral or oblique ramps. These ramps, including frontal ramps at the front of the wedge could act as barriers to rupture propagation during large earthquakes as suggested by studies on the 2015 Mw 7.8 Gorkha earthquake in central Nepal (Duputel et al., 2016; Elliott et al., 2016; Hubbard et al., 2016; Kumar et al., 2017; Wang et al., 2017; Zhang et al., 2017; Bai et al., 2019; Wang et al., 2019). In western Nepal Himalaya, the along-strike extent of the embayment approximately corresponds to the region devastated in the 1505 AD earthquake (Bollinger et al., 2016), and other large historical earthquakes have been reported (Murphy et al., 2014; Hossler et al., 2016; Ghazoui et al., 2019). These observations

122 suggest significant seismic hazard for western Nepal and that the megathrust lateral ramps may
123 control rupture propagation.

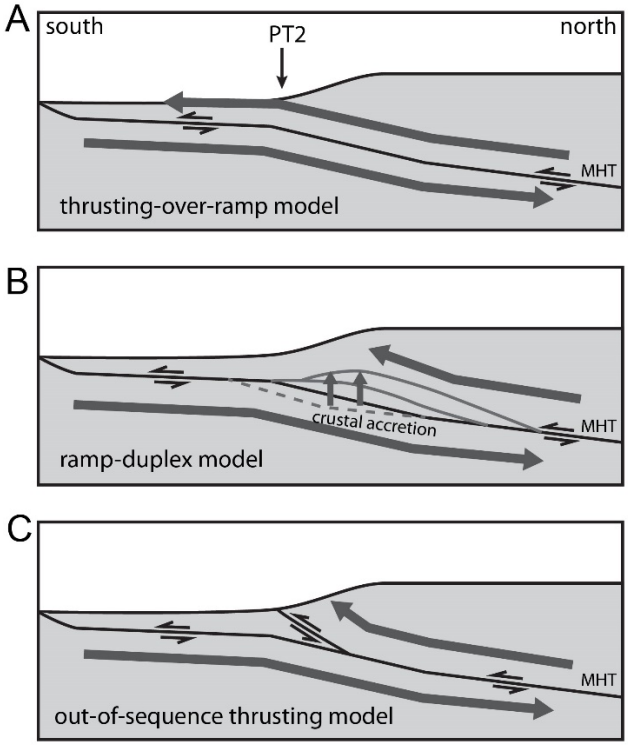

124

Figure 2 Simplified sketch of the kinematic models of MHT explains the formation of physiographic transition (PT2) between outer wedge and inner wedge. (A) Overthrusting and underthrusting along the MHT ramp. (B) Crustal accretion in the form of duplexes along MHT ramp. (C) Out-of-sequence thrusting at the physiographic transition.

125

126 To address these issues, we investigate the geometry and kinematics of the megathrust
127 from the perspective of thermokinematics. In this contribution we report new zircon (U-Th)/He
128 ages. Most of our samples are located in the eastern limb of the embayment. The rest of the
129 samples are located in the hinterland of the Himalayan plateau. Previously published
130 thermochronologic data are used to inform inversion models with different megathrust
131 kinematics. We also take this opportunity to discuss the general evolution of crustal ramps and
132 topography in western Nepal by comparing our study with observations in adjacent areas. We
133 conclude by summarizing sedimentary studies across the Himalaya orogen and propose a
134 conceptual model for the landscape and drainage system evolution that highlights the role of
135 deep crustal accretion in the development of the Himalayan orogenic plateau.

136 **2 Geological Setting**

137 2.1 Tectonostratigraphy and Structures

138 The Himalayan orogen is characterized by several rock sequences juxtaposed by major
139 east-west-striking shear zones (Gansser, 1964; Le Fort, 1975; Yin, 2006). From structurally high
140 to low levels in the thrust wedge, these rock sequences include the Tethyan Himalayan Sequence

(THS), the Greater Himalayan Sequence (GHS), the Lesser Himalayan Sequence (LHS), and the Siwalik Group (SG) (Fig. 1). The THS is a deformed package of unmetamorphosed to low-grade metasedimentary rocks that experienced greenschist to amphibolite facies metamorphism (Gaetani and Garzanti, 1991; Burchfiel et al., 1992; Liu and Einsele, 1994; Murphy and Yin, 2003; Myrow et al., 2009). The THS primarily crops out from the Indus-Yarlung suture zone to the South Tibet Detachment (STD), a north-directed normal-sense shear zone or passive roof thrust that juxtaposes the THS against the GHS (Burg et al., 1984; Burchfiel et al., 1992; Hodges et al., 1992; Coleman, 1996; Edwards et al., 1996; Carosi et al., 1998). The GHS is composed of middle amphibolite facies to lower granulite facies meta-sedimentary and meta-igneous rocks (Pêcher, 1989; Vannay and Hodges, 1996; Murphy et al., 2002; Searle and Godin, 2003; Martin et al., 2009; Kohn, 2014; Iaccarino et al., 2017). It is juxtaposed against the LHS along the Main Central Thrust (MCT), a top-to-south shear sense thrust fault (Burg and Chen, 1984; Brunel, 1986; Schelling, 1992; Robinson et al., 2003). The MCT is primarily active during the Late Oligocene - Middle Miocene (e.g. Hubbard and Harrison, 1989; Kohn et al., 2005; Yin, 2006; Montomoli et al., 2013; Cottle et al., 2015a; Larson et al., 2015; Carosi et al., 2018; Catlos et al., 2018; Braden et al., 2020). Some segments of the MCT are known to have been reactivated in the Late Miocene - Pliocene (e.g. Catlos et al., 2001; Braden et al., 2018; Catlos et al., 2018; Montemagni et al., 2019; Braden et al., 2020). The STD is usually interpreted to be coeval with the main active stage of the MCT and ceased moving in the Early Miocene in the western Nepal Himalaya (Hodges et al., 1992; Hodges et al., 1998; Murphy and Harrison, 1999; Searle and Godin, 2003; Godin et al., 2006; Cottle et al., 2015b). Between the STD and MCT, within the GHS, some studies report tectonic or metamorphic discontinuities, which have been interpreted to accommodate in-sequence thrusting prior to the initiation of the MCT (e.g. Larson et al., 2015; Montomoli et al., 2015; Carosi et al., 2018). Toward the end of the time that the STD-MCT system was active (ca. 19–13 Ma), a series of mid-crustal culminations referred to as the North Himalayan antiform developed in the central Himalayan hinterland and expose the high-grade orogenic core (e.g. Lee et al., 2000; Godin et al., 2006; Lee and Whitehouse, 2007; Larson et al., 2010) (Fig. 1). In the western Nepal Himalaya, the Northern Himalyan antiform is characterized by an east-west-trending belt of dome-shaped outcrops of GHS rocks from 81ºE to 90ºE (Fig. 1). The Thakkhola graben is bounded by several steeply dipping north-south striking normal faults (Hurtado et al., 2001; Baltz, 2012), and the Gurla Mandhata area is a metamorphic core complex bounded by the Gurla Mandhata-Humla fault system (Murphy et al., 2002; Murphy and Copeland, 2005). They both developed mainly starting from middle-late Miocene and accommodated orogen-parallel extension (Coleman and Hodges, 1995; Murphy et al., 2002; Murphy and Copeland, 2005; McCallister et al., 2014; Brubacher et al., 2020). Fan and Murphy (2021) reconciled the coeval orogen-normal shortening and orogen-parallel extension and the difference in the amount of extension of these two features in a 3D conceptual model of oblique convergence in an arcuate orogen. The LHS consists of lower greenschist- to lower-amphibolite-facies metasedimentary rocks and is deformed by a duplex system that formed in the Late Miocene after ca. 10 Ma within the outer wedge (e.g. Srivastava and Mitra, 1994; DeCelles et al., 2001; Robinson et al., 2006; Webb, 2013). Growth of the duplex led to folding of the MCT thrust sheet structurally above, which is presently exposed in synformal klippen in the outer wedge (DeCelles et al., 2001; Pearson and DeCelles, 2005). The antiformal LHS duplex and Northern Himalayan antiform usually make the region between them form synformal half-klippe, for example the Dolpo THS synform (Fig. 1). The Main Boundary Thrust (MBT) juxtaposes the LHS against the SG, which are foreland basin deposits of the wedge since middle Miocene and

then incorporated into the thrust wedge (Mugnier et al., 1999; Bernet et al., 2006; van der Beek et al., 2006; Baral et al., 2015). It is separated from the undeformed foreland by the Main Frontal Thrust (MFT). The MFT is the surface trace of the MHT. The MBT and MCT sole into the MHT at depth. In central-western Himalaya, the surface geology suggests the existence of MHT lateral or oblique ramps that affect foreland-ward propagation. Between the Thakkhola graben and the Gurla Mandhata area, the trace of the MCT, LHS duplex, and the axis of the folded Almora-Dadeldhura klippe, all shift toward the hinterland (north) in western Nepal. This results in the alignment of antiformal features, such as LHS duplexes, and synformal features, such as GHS klippen and THS half-klippen, along their strike (DeCelles et al., 2020; Fan and Murphy, 2021) (Fig. 1).

2.2 Topography and Landscape

The topography of the Himalayan wedge is characterized by a sharp physiographic transition characterized by an abrupt transition from high slopes between the high-elevation hinterland plateau and the lower slopes that mark the low-elevation frontal wedge (PT2 of Hodges et al., 2001). It is located at the base of a narrow high-slope zone connecting the inner wedge characterized by high-elevation, low-relief plateau landscape, and the outer wedge characterized by a taper-shaped regional slope (Fig. 1). PT2 exhibits along-strike variations and is usually collocated with features that define the active-uplift front of the Himalaya (e.g. Duncan et al., 2003; Harvey et al., 2015; Morell et al., 2015). The young cooling ages along this zone suggest rapid exhumation (e.g. Copeland et al., 1991; Wobus et al., 2003; Blythe et al., 2007; Johnston et al., 2020), which is thought to facilitate extrusion of high-grade rocks from lower crust in some models (e.g. Beaumont et al., 2001; Hodges et al., 2001). The above-mentioned bifurcation of the high slope zone in western Nepal Himalaya obscure the plateau-taper pattern of the topography there (Fig. 1). The northern and south branches of PT2 in western Nepal are referred to as PT2-N and PT2-S (Harvey et al., 2015).

2.3 Megathrust Models

Although some MHT models explain the specific location of the active-uplift front of the high Himalaya and supporting datasets in other areas in Himalaya, no such model exists for western Nepal. Several conceptual models are proposed suggesting an upper-crustal flat extends further to the north compared along-strike were proposed based on low-temperature thermochronologic ages and geomorphology (Harvey et al., 2015; van der Beek et al., 2016). Based on the better understanding of the MHT in the area ruptured by the Gorkha earthquake, Hubbard et al. (2016) proposed a three-dimensional model for the MHT across Nepal. Similarly, by integrating various datasets and a thickness model of the Himalayan high grade core, Fan and Murphy (2021) introduced lateral and oblique ramps to the 2D conceptual model of the MHT in western Nepal and proposed a 3D conceptual model explaining the embayment of the active-uplift front and the along-strike change in the surface geology. Several studies focusing on the fold and thrust belt in the outer wedge of the Himalaya propose MHT models based on a structural restoration (DeCelles and DeCelles, 2001; Robinson, 2008; Robinson and McQuarrie, 2012; Olsen et al., 2019; DeCelles et al., 2020) (Fig. 3). These models can well explain the detailed structures in the outer wedge to the south of the PT2 but cannot resolve the structures in the inner wedge and the mid-lower crustal ramp in the MHT. They also fail to explain the first-order landscape because the northern MHT ramp in these models is usually located below the

area between the PT2-S and PT2-N, where the landscape is relatively flat and of low relief (Fig. 3).

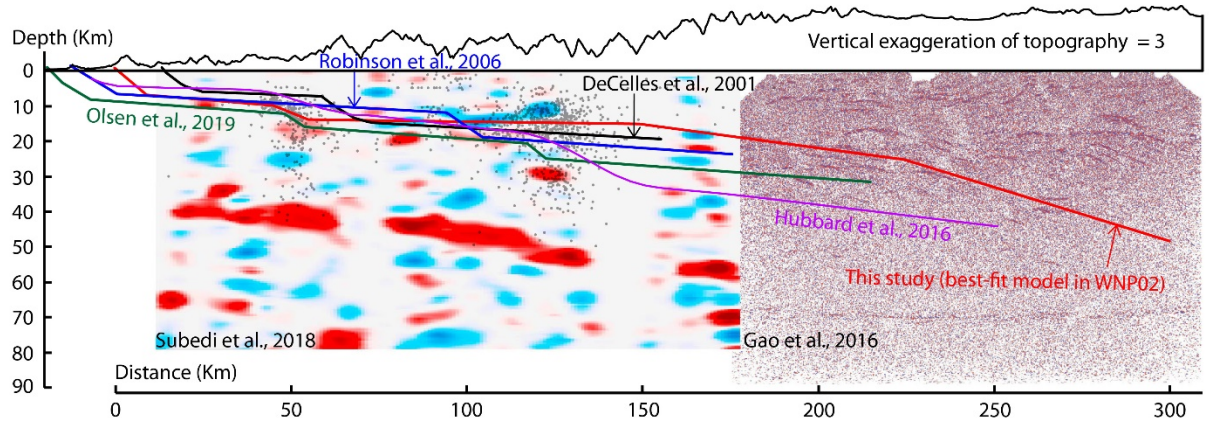

Figure 3 A comparison between different models of the MHT in the western Nepal Himalaya. The red line shows the geometry of preferred model in this study. Gray dots show the earthquake hypocenters projected to the profile from within 20 km. The data includes earthquakes from December 2014 to November 2015 reported by Hoste-Colomer et al. (2018) and earthquakes from 1995 to 1999 recorded by National Seismic Center and relocated by Ader et al. (2012). Image in the left is P-to-S receiver function migration image reported by Subedi et al. (2018) in which the red and blue represent high and low PS/P amplitude respectively. The seismic reflection profile image in the right is reported by Gao et al. (2016). For original interpretation of the images, refer to the original papers. Notice the reflector along the upper crustal flat of the MHT and the duplexes in the hinterland.

Receiver function analysis of teleseismic waveforms in western Nepal suggests a longer upper-crustal flat in MHT compared to central Nepal. This flat in the MHT connects to a long, gently dipping ramp that extends northward to lower-crustal depths (Subedi et al., 2018) (Fig. 3). However, using the available data, the geometry of this ramp is not precisely located. Subedi et al. (2018) interpret the ramp geometry based on the change in depth between the upper-crustal reflectors and several short reflectors at the northern end of the profile. The reflectors at the northern end are consistent with lower-crustal reflectors on the other receiver function profile image that extends from to the west of the Gurla Mandhata metamorphic core complex to the south of South Tibet (Xu et al., 2017). A deep seismic reflection profile along a transect close to the profile in Xu et al. (2017) also shows a middle-lower crustal duplex structurally above the mid-lower crustal reflector (Gao et al., 2016). The locations of foci of earthquakes in western Nepal also suggest the seismogenic part of the MHT extends further to the north compared to areas along strike (Ader et al., 2012; Hoste-Colomer et al., 2018). However, none of these models are based on a geophysical data along a complete transect from the lower Himalaya to the higher Himalaya of the embayment in western Nepal area and none have been tested with geologic data.

3 Thermochronologic Data

3.1 Sample and Methods

In order to investigate the geometry and kinematics of the MHT in western Nepal and the correlation between 3D geometry of the MHT (e.g. lateral and oblique ramp locations) with the

254 embayment, we carried out thermokinematic modeling along a transect that extends across the
255 apex of the embayment. We then compare the modeling results with our new thermochronologic
256 data along the eastern limb of the embayment. The data used in the modeling is from published
257 studies and is described later.

258 Zircon (U-Th)/He (ZHe) dating was carried out because of the sensitivity of ZHe ages to
259 active and new tectonics over a time span of several million years. The closure temperature of
260 the ZHe thermochronometer is affected by several factors, such as chemical composition of the
261 crystals, concentration of radiation damage, grain size, and cooling rate (Reiners et al., 2004;
262 Reiners, 2005). For typical plutonic cooling rates and crystal sizes, the closure temperature is
263 about 170-190 °C (Reiners et al., 2004). Therefore, it can record the exhumation history through
264 the upper about 5-8 km of the crust. In an active region, such as the Himalaya, where the highest
265 exhumation rate close to the PT2 can reach several mm/yr, the ZHe ages can record cooling
266 history in the past less than 3 million years.

267 We analyzed 12 samples. Seven are from the northern branch of PT2 (Fig. 4). These data
268 fill a data gap between far-western Nepal along the Karnali river transect and western Nepal. The
269 other samples are from the inner wedge. The locations, lithology, and units of the samples are
270 listed in Table S1.

271 Samples were processed for ZHe dating at thermochronology lab in University of Texas,
272 Austin (refer to Text S1 for analytical procedure). For each sample, we usually analyzed three
273 grains, but from DG-10 and DF-3 we analyzed four grains and two grains respectively. Some
274 aliquots were discarded on the basis of anomalous isotopic values and others because they
275 yielded outlier ages defined as being more than 30% older or younger than the rest of the grains
276 in their respective samples.

277 3.2 Results

278 Analytic results of our samples are reported in Table 1. Samples from south of the Dolpo
279 synform have ZHe ages that range from 3.1 – 7.4 Ma. Two samples among them are 3.1 and 3.3
280 Ma. These young ages are consistent with or slightly older than the ages reported at the active-
281 uplift front, though they are closer to the front of the orogen compared with the young cooling
282 ages reported at the apex of the topographic embayment in western Nepal Himalaya (Fig. 4). The
283 samples from the inner wedge have ZHe ages that range from 9.5 – 12.2 Ma, significantly older
284 than the samples from the southern Dolpo area and from the apex of the topographic embayment,
285 though they approximately align well with the samples of young cooling ages at the apex of the
286 topographic embayment along the strike of the northern Himalayan anticline (Fig. 4). These old
287 ages are consistent with recently reported ages close to the northern Himalayan antiform in the
288 inner wedge along the Thakkhola graben (Brubacher et al., 2020).

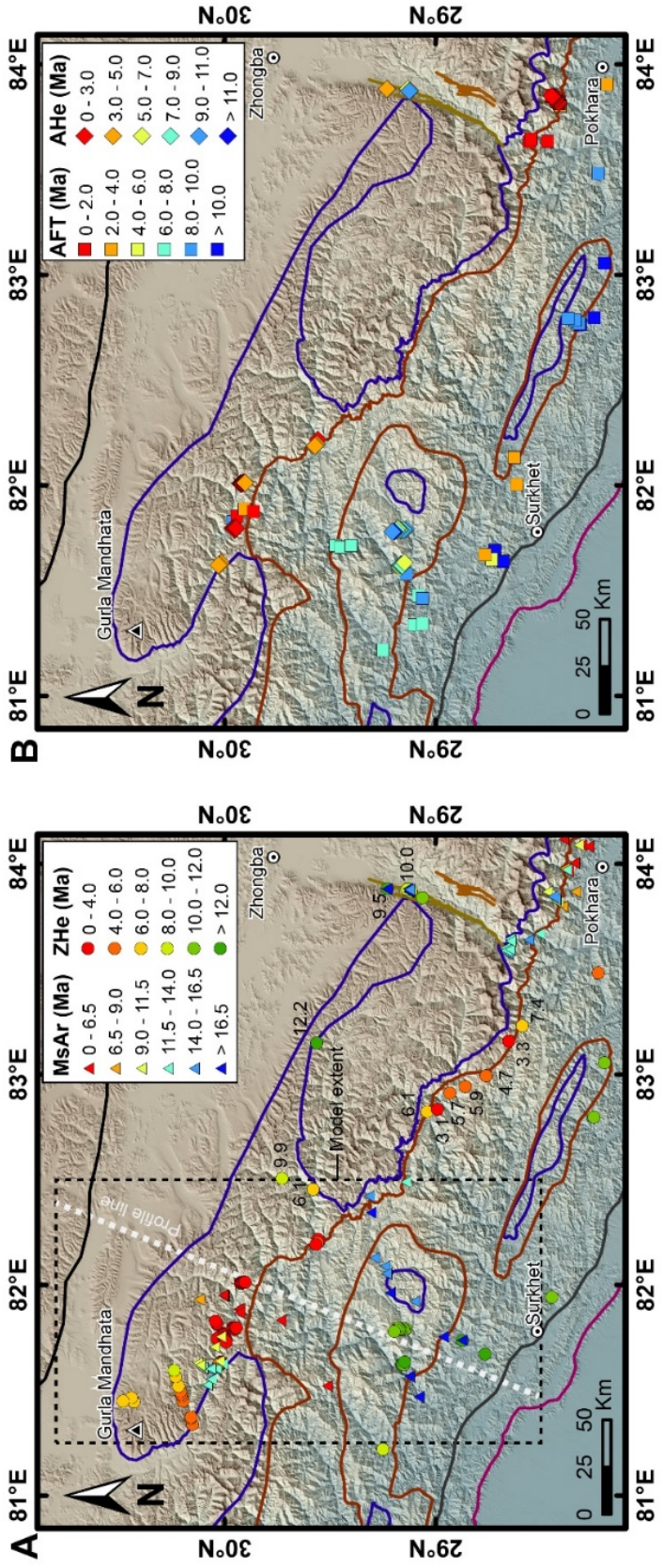

Figure 4 Previously reported and new thermochronologic ages in the western Nepal Himalayan area. The dash box in (A) shows the extent of the themrokienmatic models in this study. The ZHe ages labeled with age values are newly reported ages in this study. Previously published data are from Vannay and Hodges (1996), Godin et al. (2001), Robert et al. (2011), Nadin and Martin (2012), Sakai et al. (2013), Mercier (2014), McCallister et al. (2014), Harvey (2015), Martin et al. (2015), Nagy et al. (2015), Gibson et al. (2016), van der Beek et al. (2016), Soucy La Roche et al. (2018), Braden et al. (2020), Brubacher et al. (2020), and DeCelles et al. (2020). MsAr – Muscovite $^{40}Ar/^{39}Ar$ age; ZHe – Zircon (U-Th)/He age; AFT – Apatite fission track age; AHe – Apatite (U-Th)/He age.

Table 1 Zircon (U-Th)/He Dating Results[a]

Sample	Age (Ma)	U (ppm)	Th (ppm)	^{147}Sm (ppm)	He (nmol/g)	mass (ug)	Ft	ESR	Mean Age (Ma)	Error (1σ)
DG-10-2	3.3	505.5	28.1	0.0	6.3	1.99	0.70	36.31		
DG-10-3	3.3	309.0	9.2	-3.0	4.1	3.18	0.74	42.97		
DG-10-4	3.4	703.7	39.8	0.8	10.7	11.07	0.82	65.07		
DG-10-5	3.1	551.7	10.1	-1.7	7.2	5.67	0.78	52.54	3.27	0.06
DG-38-2	2.9	124.9	83.6	0.0	1.6	3.16	0.72	41.28		
DG-38-3	3.2	240.7	105.4	0.0	3.1	2.04	0.68	35.25		
DG-38-4	3.1	673.9	182.9	0.0	8.3	1.90	0.69	36.24	3.08	0.07
DH-10-1	5.7	481.3	203.7	2.6	13.4	14.34	0.83	69.80		
DH-10-2	5.5	300.0	75.5	0.0	6.9	3.83	0.74	43.37		
DH-10-3	7.3	518.3	85.7	1.4	17.5	13.10	0.83	68.71	6.14	0.46
Dolpo-04-1	*16.3*	*253.9*	*87.0*	*0.8*	*19.7*	*11.78*	*0.82*	*66.09*		
Dolpo-04-2	12.1	278.5	98.3	0.0	15.2	6.24	0.77	50.57		
Dolpo-04-3	12.2	171.6	61.7	0.8	10.0	12.01	0.82	64.83	12.20	0.03
DF-3-2	10.0	1141.8	194.6	0.0	46.4	2.91	0.72	40.72		
DF-3-3	*4.7*	*190.4*	*59.5*	*1.8*	*3.9*	*5.13*	*0.76*	*49.33*	10.0	0.80
DF-4-3	10.5	1649.4	30.2	1.3	74.1	7.23	0.79	54.31		
DF-4-1	9.7	1720.5	55.4	1.3	71.2	7.23	0.78	52.79		
DF-4-2	8.4	1551.4	27.8	0.0	41.8	0.86	0.60	26.03	9.53	0.51
DG-12-1	8.0	689.6	81.1	0.0	21.4	2.64	0.70	37.73		
DG-12-2	*14.1*	*1937.3*	*46.7*	*0.0*	*93.0*	*1.37*	*0.63*	*28.95*		
DG-12-3	6.8	342.1	54.0	0.0	7.8	0.94	0.60	26.66	7.40	0.41
DG-22-1	6.2	321.2	88.3	2.2	9.5	16.75	0.84	72.47		
DG-22-2	4.6	439.6	34.1	0.0	8.3	4.78	0.76	46.31		
DG-22-3	3.3	262.8	37.6	0.0	3.4	2.30	0.70	37.83	4.68	0.67
DG-29-1	6.7	1143.0	35.4	0.0	29.8	2.65	0.71	38.82		
DG-29-2	5.2	136.1	74.8	1.9	3.6	15.10	0.83	72.20		
DG-29-3	5.8	514.7	83.8	0.0	13.1	6.78	0.79	55.59	5.91	0.36
DG-30-1	5.5	281.9	30.1	1.5	7.5	30.41	0.87	91.30		
DG-30-2	6.4	301.1	44.1	1.2	9.8	136.73	0.92	151.44		
DG-30-3	5.2	166.8	41.4	1.5	4.2	18.85	0.84	75.56	5.69	0.29
TB10-12-1	5.4	294.9	97.9	1.9	7.5	14.49	0.82	66.64		
TB10-12-2	6.8	322.2	75.5	0.0	10.4	17.24	0.84	73.28		
TB10-12-3	*16.5*	*248.9*	*97.5*	*1.0*	*19.3*	*8.97*	*0.80*	*57.83*	6.06	0.50
TB10-9-1	11.7	1054.0	90.3	21.2	57.8	24.09	0.85	80.46		
TB10-9-2	10.2	794.7	106.4	10.7	39.7	45.06	0.88	99.95		
TB10-9-3	7.7	542.8	86.0	5.1	20.2	31.07	0.86	86.76	9.87	0.95

[a]Ft is the alpha ejection correction factor. ESR is equivalent sphere radius. Data in italic indicate outliers that were discarded in mean age calculation. The age error is the standard deviation between aliquots divided by the square root of the number of aliquots.

4 Thermokinematic Modeling

To test the geometric and kinematic models of the MHT, we conducted thermokinematic modeling by using a modified version of the software Pecube (Braun, 2003; Braun et al., 2012). Models are evaluated by comparing the observed ages obtained from sample analyses with ages predicted by the software. To quantitatively do this, the software calculates the misfit using a goodness-of-fit statistic Φ,

$$\Phi = \frac{1}{n}\sqrt{\sum_{i=1}^{n} \frac{(PredAge_i - ObsAge_i)^2}{{\sigma_i}^2}}$$

where n is the number of thermochronometer ages, *PredAge* and *ObsAge* are the ages predicted by Pecube and obtained from sample analyses, respectively, and σ is the 1-sigma uncertainty in the observed age.

4.1 Modeling Extent and Inversion Input Data

Conceptual models describe a network of oblique ramps to explain along strike changes in the geometry of the MHT (Hubbard et al., 2016; Fan and Murphy, 2021). In this study, we focus on explaining the most representative sector of the embayment along the Karnali river transect, where it reaches its largest recession (Fig. 4). Because faults in Pecube can only be defined by a constant strike (i.e., no lateral ramp can be incorporated) we use the MHT of the Karnali transect to define the megathrust of the entire model and only use the ages that are representative of the Karnali transect in the model.

Thermochronologic ages used in the modeling are reported from multiple dating systems including muscovite $^{40}Ar/^{39}Ar$ (MsAr) ages, zircon and apatite (U-Th)/He (ZHe and AHe respectively) ages, and apatite fission track (AFT) ages (McCallister et al., 2014; Mercier, 2014; Harvey, 2015; Nagy et al., 2015; van der Beek et al., 2016; Soucy La Roche et al., 2018; Braden et al., 2020). We selected the data for modeling from published datasets following criteria as follows: (1) we do not use the data out of the swath of our interested section because those samples might have significantly different thermal histories from the rocks within the swath due to the existence of lateral and oblique ramps of the MHT; (2) we do not use data that may be affected by the upper-crustal ramp of the MHT in the outer wedge close to the PT2-S because this is outside the area of interest; (3) we do not use ages older than 16 Ma because several studies suggest that the dynamics of the Himalayan orogen and thus the exhumation pattern changed significantly during the Middle Miocene and resolving the complex evolution history in this transition is not a goal of this study (e.g. Mugnier and Huyghe, 2006; DeCelles et al., 2011; Husson et al., 2014; Webb et al., 2017). For some data close to the interpreted lateral ramps, we do not use them in the inversion modeling or calculating the misfit values, but we still use the algorithm to estimate their ages in the forward model and incorporate them in the age-comparison plot for discussion. Close to the PT2-N, both ca. 6 Ma and 9-10 Ma MsAr ages are reported along Karnali transect, but MsAr ages reported along the active-uplift front in other sectors in Himalaya are mostly ca. 6 Ma or younger. The reason for the large difference in the MsAr cooling ages over a short distance along the modeled transect is unknown, therefore we used all the ages. The distribution of the ages used in the modeling is shown in the Figure S1. Some of the reported MsAr ages have much smaller uncertainties than other dating systems. Because we are focused on the current geometry and kinematics of the MHT and the small uncertainties of the potential outliers of the 9-10 Ma MsAr ages close to the PT2-N may mislead the inversion process, we change the uncertainties of the MsAr ages younger than 9 Ma to 0.5 Ma and the uncertainties of the MsAr ages older than 9 Ma to 1.0 Ma when conducting inversion modeling, such that the inversion does not over-value the MsAr ages, which are usually much older than the ages of other dating systems. However, in the forward model, we used true uncertainties for all ages. The calculated misfit values of the inversion model and forward model are notated as misfit (Φ) and corrected misfit (Φ_{corr}) later.

4.2 Forward Model in Pecube and Model Parameters

Pecube calculates the location and temperature of points in the model using inputs of fault geometry, fault slip rate, flexural isostacy, radiogenic heat production, frictional heat production, and the boundary temperatures at the surface and the bottom of the model. These calculations are repeated at every timestep. The time-temperature history for each point is then used to calculate the expected cooling ages for each thermochronologic system, using known kinetic parameters for the system in question.

In Pecube, for a model without a localized zone of enhanced rock uplift, mass transport is parallel to each fault dip panel, and the fault geometries are defined by coordinate pairs (X, Y) defining the locations of fault dip change in a transect parallel with the mass-transport direction. In this study, the X and Y are the horizontal distance from the MFT fault trace, and vertical distances below sea level, respectively (Fig. 5). The slip rate along the MHT is defined by the convergence rate (V_{conv}) between the hanging wall and footwall and a partitioning factor (λ) partitioning the convergence into hanging-wall overthrusting, $V_o = (1 - \lambda)V_{conv}$, and footwall underthrusting, $V_u = \lambda V_{conv}$, with respect to the MHT (Fig. 5). This modified version of Pecube used in this study is the same as that used in Landry et al. (2016), and it deals with the change in the velocity in the hanging wall between different dip panels using a kink-band style fault kinematics described by Suppe (1983) — the velocity vectors change across the calculated planes bisecting the angle between any two neighboring fault dip panels, rather than using the velocity averaging approach in the original version. The other modification of the software is adding a function of applying a localized zone of enhanced rock uplift, similar to the version used in Herman et al. (2010). It simplifies the effect of localized crustal accretion by adding an extra vertical velocity component (V_{CA}) within the region defined by two specified distances (CA_{dist} and CA_{prox} for the southern and northern points respectively in this study) from the fault trace, MFT (Fig. 5). Rather than using the strategy that applies an enhanced uplift zone at a constant location with respect to the topography in the simulations conducted by Herman et al. (2010) and Landry et al. (2016), we apply a narrower enhanced uplift zone and make it translate hinterland-ward at an advection rate (CA_{adv}) to its present location which is defined by CA_{dist} and CA_{prox} in a certain amount of time (CA_T) to simulate one cycle of accretion (Fig. 5). Our strategy is more consistent with the kinematics for the generation of a new horse in a duplex, i.e. a newly generated ramp underthrusts beneath the slice of rock in hanging wall of the new ramp. The total uplift caused by the enhanced uplift zone in one cycle of crustal accretion on a cross-section is an isosceles trapezoid (Fig. 5), which is more consistent with geometry of a horse than the rectangle-shaped uplift generated by an enhanced uplift zone at a constant location. We only simulate the last cycle of accretion and set $CA_T = 6$ Ma to test the thermal effects since the specific kinematics of the entire multi-cycle accretion process in the mid-lower crust is unknown. The time span of one cycle of accretion is also unknown but we consider 6 Ma to be reasonable compared with the balanced cross-section coupled with thermokinematic modeling study in central Nepal Himalaya, the inversion result of the time span of the last accretion below the LHS duplex in northwestern Himalaya, and the geodynamic simulation of the crustal accretion in Himalaya (Mercier et al., 2017; Stübner et al., 2018; Ghoshal et al., 2020). We enable fault translation in all the models to simulate lateral advection of the model topography, such that all samples can translate laterally with respect to the fault but only move vertically relative to the topography.

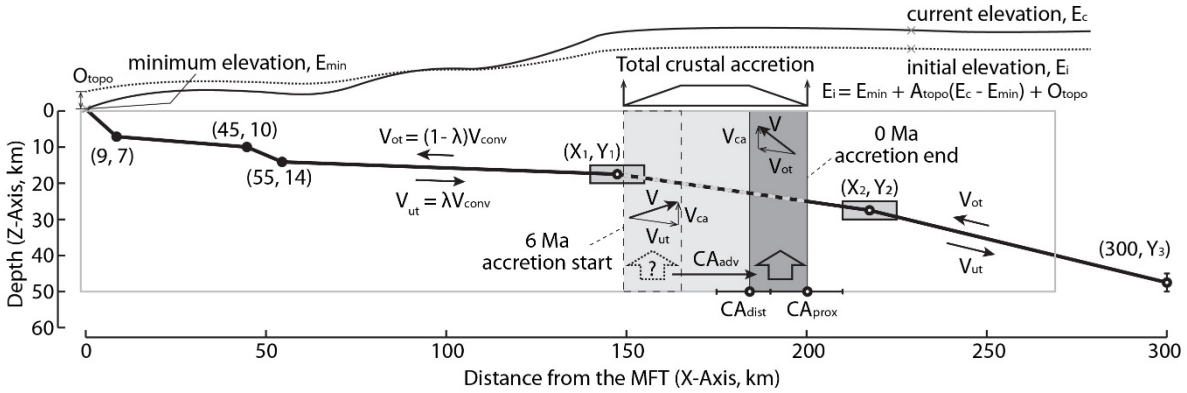

Figure 5 Illustration shows the thermokienmatic model boundary conditions and parameters. The kinematic model has the convergence rate (Vconv) partitioned on either side of the megathrust into upper plate overthrusting component (Vot) and lower plate underthrusting component (Vut) using a partitioning factor (λ). The geometry of the megathrust is defined using a series of points along its length and the inverted free points, such as (X1, Y1), (X2, Y2), and (300, Y3), may occupy any position within each search box or on the error bar. Crustal accretion is carried out by adding a vertical uplift component (Vca) to the velocity field within the range defined by two distance coordinates (CAdist, and CAprox). The range can advect from a position represented by dash box hinterland-ward to the present position defined by CAdist and CAprox in the past 6 Ma at an advection velocity of CAadv. The effect of topographic evolution is simulated by assuming a liner evolution from initial topography (Ei) to the current topography (Ec)and assuming an initial topography by compress the relief of current topography (Ec-Emin) by an amplification factor (Atopo) and make it offset vertically by Otopo. For details of the model and other parameters refer to the text and Table 3.2 and 3.3.

The dynamic thermal field of the model is calculated using an iterative solution to the finite-element formulation of the 3-D thermal advection-diffusion equation (Braun et al., 2012),

$$\rho c\left(\frac{\partial T}{\partial t}+V\nabla \mathrm{T}\right)=\mathrm{k}\nabla^{2}\mathrm{T}+\mathrm{H}$$

where ρ is density, c is heat capacity, T is temperature, t is time, V is the velocity, k is thermal conductivity, and H is volumetric radiogenic heat production (for units and symbols, see Table 2). In our models, the temperature at the base of the model is set at 750 °C and does not change over time. Surface temperature decreases with elevation at an atmospheric lapse rate of 6 °C/km from 25 °C at 0 km. Thermal diffusivity is 35.0 km^2/Myr. The bottom of each model is 50 km below the lowest point of the modeled area. Although we only use ages younger than 16 Ma, we run the models from 20 Ma to allow the samples in the model to accumulate enough displacement to be thermally reset at the beginning and to help the model obtain a natural, kinematic-affected, thermal field at 16 Ma. The default age of rocks in the model is 20 Ma.

Table 2 Parameters of Pecube Models[a]

Parameter Name	Parameter Range	Units	Parameter Symbol	Reference
Material Properties				
Thermal conductivity	2.5	W/m/K	k	Whipp et al. [2007]
Specific heat capacity	800	J/kg/K	c	Whipp et al. [2007]
Crusal density	2700	kg/m^3	ρc	
Upper mantle density	3200	kg/m^3	ρm	
Thermal difusivity	35.0	km^2/My	α	
Volumetric radiogenic heat production		$\mu W/m^3$	H	
Radiogenic heat production	**15-25**	°C/Myr	A	
Effective elastic thickness of the India plate	25.0	km		Jordan and Watts [2005] Berthet et al. [2013]
Young's modulus	100.0	GPa	E	
Poisson's ratio	0.3	n/a	ν	
Pecube Model Parameters				
Mean annual surface temperature in the foreland	25.0	°C	Ts	
Atmospheric lapse rate	6	°C/km	L	Landry et al. [2016]
Basal temperature	750	°C	Tb	
India-Eurasia convergence rate	**Variable**	mm/yr	V_{conv}	Bilham et al. [1997] Jouanne et al. [1999] Larson et al. [1999]
Convergence partitioning	**0.5-0.7**	n/a	λ	
Model time step	Optimal	years		
Horizontal node spacing	0.9	km		
Vertical node spacing (0-5 km)	0.9	km		
Vertical node spacing (5-15 km)	2.7	km		
Vertical node spacing (15-50 km)	8.1	km		
Model domain	255×122×50	km		
Fault geometry	**Variable**	km	(Xn, Yn)	
Crustal accretion (south boundary)	**Variable**	km	CA_{dist}	
Crustal accretion (north boundary)	**Variable**	km	CA_{prox}	
Crustal accretion vertical rate	**Variable**	mm/yr	V_{ca}	
Crustal accretion window advection rate	**Variable**	mm/yr	CA_{adv}	
Amplification factor for evolving topography	**Variable**	n/a	A_{topo}	
Offset factor for evolving topography	**Variable**	km	O_{topo}	

[a]The bold entries indicate the free parameters that were inverted for in the simulations.

Previous studies dispute whether the Himalayan orogen had a similar topography in the Miocene to the present topography in High Himalaya (e.g. Masek et al., 1994; Wang et al., 2010; Gébelin et al., 2013; McDermott et al., 2013; Carrapa et al., 2016). Moreover, recent geomorphologic analysis in the Dolpo area suggests that glacial and fluvial erosion along with tectonics have significantly reshaped the extent of the orogenic plateau (Buceta et al., 2020). Therefore, we incorporate the effect of evolving topography in one inversion. Instead of coupling Pecube with a landscape evolution modeling software, as Herman et al. (2010) did, we simply assume an initial topography of the same shape but different relief and minimum elevation than the present topography, and assume a linear evolution from the initial topography over time (Fig. 5). To make a synthetic initial topography, the software first keeps the elevation of the lowest point (E_{min}) in the current topography unchanged and linearly compresses the current topography by an amplification factor (A_{topo}). After the compression, the elevation of any point on the surface changes from current elevation decreases to $E_{min} + A_{topo}(E_c - E_{min})$. The software then vertically moves the compressed topography by an offset distance (O_{topo}). This results in a synthetic initial topography, in which every point has an initial elevation, $E_i = E_{min} + A_{topo}(Ec - E_{min}) + O_{topo}$.

In models with evolving topography, flexural isostasy is enabled to compute the effect of isostatic adjustment due to evolving topography. The algorithm deals with the subducting plate as a thin elastic plate. We use 25.0 km for the effective elastic thickness of the Indian plate based on the reported Bouguer gravity anomaly data (Jordan and Watts, 2005; Berthet et al., 2013). We use 2700 kg/m^3 and 3200 kg/m^3 for crustal and upper mantle density respectively. Young's modulus (E) is 100 GPa and Poisson's ratio (ν) is 0.25 in the models.

We designed three inversions to simulate exhumation: (1) exhumation caused by the flat-ramp geometry of the MHT with a steady state topography ("ramp model", WNP01); (2) exhumation caused by both the flat-ramp geometry of the MHT and localized enhanced crustal accretion with a steady state topography ("ramp + duplex model", WNP02); (3) exhumation caused by both the flat-ramp geometry of the MHT and localized enhanced crustal accretion, and affected by the evolving topography ("ramp + duplex + evolving topography model", WNP03). We did not design a model for the out-of-sequence thrusting hypothesis, but discuss it based on our modeling results. All models have a dimension of 255 km × 122 km × 50 km. The topography data is down sampled to a resolution of approximately 900 m. To save computing time, we used a varying node spacing at different depths in the models; 0.9 km spacing for the upper 0-5 km, 2.7 km spacing for the 5-15 km part, and 8.1 km spacing for the 15-50 km part. For a list of the model parameters, including their values, units, symbols and important references, refer to the Table 2. We use the inversion algorithm of Pecube to invert for parameters specifically characterizing the three tectonic scenarios. For the geometry of the MHT in scenarios WNP01 and WNP02, because we focus on the exhumation caused by the deep structures in the hinterland of the wedge, we only invert for the coordinates of the northernmost three nodes among the nodes defining the geometry of the MHT, notated as (X1, Y1), (X2, Y2), and (X3, Y3) (Fig. 5). For the northernmost dip panel of the MHT, we only invert for Y3 in the models and set X3 = 300 km to find a proper dip angle. For all other nodes to the south of these three nodes, primally defining the upper-crustal flat, the southern small ramp, and the MFT, we set their coordinates based on seismic images, balanced cross-sections, and microseismicity, and do not invert for them. Previous studies suggest that the basal temperature and radiogenic heat production are correlated and can compensate each other to some extent. Because we define the

450 basal temperature at 750 °C, we invert for the radiogenic heat production, A (in °C/Myr). We
451 also inverted for the convergence rate and partitioning factor for several reasons; (1) Current
452 GPS data suggests convergence rate is in a wide range of 14-21 mm/yr; (2) the convergence rate
453 and the partitioning between overthrusting and underthrusting over the past 20 Ma are not well
454 known; (3) Internal shortening within the upper plate is not simulated in the simplified models,
455 which may cause inconsistency between the models and the real-world geology even if using the
456 correct values. For scenario WNP02, we also invert for the four parameters defining the crustal
457 accretion (CA_{dist}, CA_{prox}, CA_{adv}, and V_{CA}). The inverted parameters for scenario WNP03 are
458 slightly different from scenario 2; (1) We invert for the two parameters defining the evolving
459 topography, A_{topo} and O_{topo}; (2) To reduce the dimension of the parameter space, we set the Y1
460 and Y3 as constants respectively based on the inversion result of scenario WNP02. Table 3
461 shows the parameter values and the ranges of the values used in each inversion set.

Table 3 Inversion Results[a]

462

	Inversion Name		
	WNP01	WNP02	WNP03
Number of models	22220	28820	28820
Φ/Φ_{corr}	0.26/0.78	0.22/0.55	0.22/0.55
A_{topo}	n/a	n/a	**0.96** (0.5:1.0)
O_{topo} (km)	n/a	n/a	**0.14** (0.0:2.0)
Tb (°C)	750	750	750
A (°C/Myr)	**24.89** (15:25)	**24.94** (15:25)	**24.63** (15:25)
Y3 (km)	**49.9** (45:50)	**48.5** (45:50)	50
Y2 (Km)	**25.0** (25:30)	**25.4** (25:30)	**25.9** (25:30)
X2 (Km)	**220.3** (215:230)	**224.6** (210:225)	**224.5** (210:225)
Y1 (Km)	**15.2** (15:20)	**15.2** (15:20)	15
X1 (Km)	**167.3** (160:175)	**149.2** (140:155)	**147.2** (140:155)
V_{conv} (mm/yr)	**17.1** (15:20)	**15.5** (14:20)	**14.5** (14:20)
λ	**0.52** (0.5:0.7)	**0.52** (0.5:0.7)	**0.50** (0.5:0.7)
V_{ca} (mm/yr)	n/a	**4.0** (3.0:6.0)	**5.0** (3.0:6.0)
CA_{dist} (km)	n/a	**189.0** (175:190)	**189.3** (175:190)
CA_{prox} (km)	n/a	**203.2** (190:210)	**203.3** (190:210)
CA_{adv} (mm/yr)	n/a	**5.2** (4.0:6.0)	**5.2** (4.0:6.0)

[a]Values in brackets indicate the investigated range of the free parameters and values in bold indicate lowest misfit values for each parameter.

463

464 4.3 Inversion Algorithm: Neighborhood Algorithm

465 When combined with the Neighborhood Algorithm (NA) (Sambridge, 1999a, b;
466 Rickwood and Sambridge, 2006), Pecube can perform inversion modeling that searches for a
467 combination of parameters depicting a forward model that produce predicted cooling ages

consistent with the observed ages. The algorithm searches within the multidimensional parameter space defined by given ranges of free parameters.

The NA deals with the inversion in two stages. In the first stage, the software selects the first set of forward models by randomly selecting parameters from their defined ranges and uses the selected parameters to divide the model parameter space into Voronoi cells (Sambridge, 1999a). The parameters for subsequent forward models are selected from within the subset of Voronoi cells with a low misfit (Φ) to the observed ages. During the inversion, each subsequent forward model is selected from 80-85% (resampling ratio, varies with different scenarios) of the current Voronoi cells with the lowest misfits.

The second stage of the NA is an appraisal of the search results to define statistical limits on the ranges of input parameters that provide a good fit to the observed age data (Sambridge, 1999b). Bayesian inference is used to produce posterior probability density functions (PPDFs) for each model parameter using a likelihood function L,

$$L = \exp\left(-\frac{n}{2}\sqrt{\sum_{i=1}^{n}\frac{(PredAge_i - ObsAge_i)^2}{{\sigma_i}^2}}\right)$$

the appraisal yields 1-D and 2-D PPDFs for the model parameters that are presented for each set of model parameters.

5 Modeling Results

For the three inversion sets presented below (Fig. 6-8), the parameter ranges are determined based on multiple trials. To evaluate the defined ranges of the inverted parameters in each trial, we use reasonably small ranges of parameters and compute more than 20,000 forward models in each inversion. If the inversion converges at the end of the defined ranges for many inverted parameters, we change the ranges of the corresponding parameters in the next inversion trial. A summary of the parameter ranges of the presented inversions, parameter values of the best-fit model in each inversion, and the misfit value of the best-fit model for the presented inversion for each scenario is shown in Table 3. As introduced above, we use synthetic errors for some ages in the inversion and calculate the corresponding misfit, Φ. We then select the best model found in each inversion and calculate the corrected misfit, Φ_{corr}, using true errors of all ages.

5.1 Inversion Set WNP01: Slip on the MHT with Steady State Topography

The models in the inversion set WNP01 simulate a scenario where exhumation is caused only by slip along the MHT with steady topography (ramp model). The inversion set comprises 22,220 forward models. Using a resampling ratio of 85%, the inversion converges to a misfit $\Phi < 0.3$ after approximately 8,000 models. For the best-fit model, the misfit is $\Phi = 0.26$ and the corrected misfit $\Phi_{corr} = 0.78$.

The inversion result indicates that the misfit of model in this scenario is sensitive to the fault geometry (Fig. 6). The distance between the mid-lower crustal ramp and the MFT (X1 and X2) is well constrained. The depths of the inverted nodes of the fault in low-misfit models suggest a shallow mid-crustal ramp indicated by the low Y1 and Y2 and a steep hinterland sector indicated by the large Y3 (Fig. 9). The best-fit model has a mid-crustal ramp starting from 167.3

km to 220.3 km from the MFT and has a dip of 10.5°. The hinterland sector of the MHT in the best-fit model has a dip of 17.4°. These three depth parameters converge to the end of the given ranges in the inversion but we didn't test new ranges because the ranges of these parameters are consistent with other geophysical and geologic data. The convergence rate and partitioning factor for low-misfit models are correlated in a narrow zone on the 2D PPDF plot (Fig. 6), suggesting that the misfit is very sensitive to the slip rate along the MHT at the first order but the effect of convergence and the partitioning between the underthrusting and overthrusting can compensate each other to some extent. The best-fit model has a convergence rate of 17.1 mm/yr with 52% of it accommodated by footwall underthrusting. Both of these values are reasonable compared with previous studies (Bilham et al., 1997; Jouanne et al., 1999; Larson et al., 1999; Coutand et al., 2014; Landry et al., 2016). Because we used a constant temperature at the bottom of the model, we inverted for the heat production over a wide range, 15-25 °C/Myr, and the inversion converges to the high end of the range, suggesting a hot orogen.

The comparison between the predicted ages of the best-fit model in this inversion set and the observed ages is shown in Figure 9. Some ages not used in the inversion or misfit calculation are also included in the plot. Generally, for the low-temperature-system ages used in the inversion, including AHe, ZHe, and AFT ages, most predicted ages match the observed ages within 1 standard uncertainty. Age cluster of AHe and ZHe between 29.5°-29.6° N (132-135 km from the MFT) are not used in the inversion, they have a worse match than the ages used in the inversion. Among the four ZHe and four AHe ages in the cluster, only two predicted AHe ages overlap with the observed ages within 1 standard uncertainty, but the discrepancy is usually within 2 standard uncertainties. For the MsAr ages, there is a large discrepancy between the predicted and observed ages for rocks in the hinterland close to the PT2-N. Among the two previously introduced groups of MsAr ages close to the high-slope zone, the predicted ages are closer to the group of 9-10 Ma data than the ca. 6 Ma ages. However, ages of ca. 6 Ma or younger are common along the high-slope zone in other segments of the Himalaya. For example, one MsAr age of 5.85 ± 0.67 Ma is reported at 29.73°N (139 km from the MFT) in this region(Mercier, 2014), close to the high-slope zone to the west of the modeled profile across a proposed lateral ramp in the MHT (Fig. 4). Thus, we interpret that this model fails to produce MsAr ages consistent with observation close to the high-slope zone. The predicted MsAr ages of the samples from the southernmost part of the model are consistent with observed ages (age difference < 1 Ma).

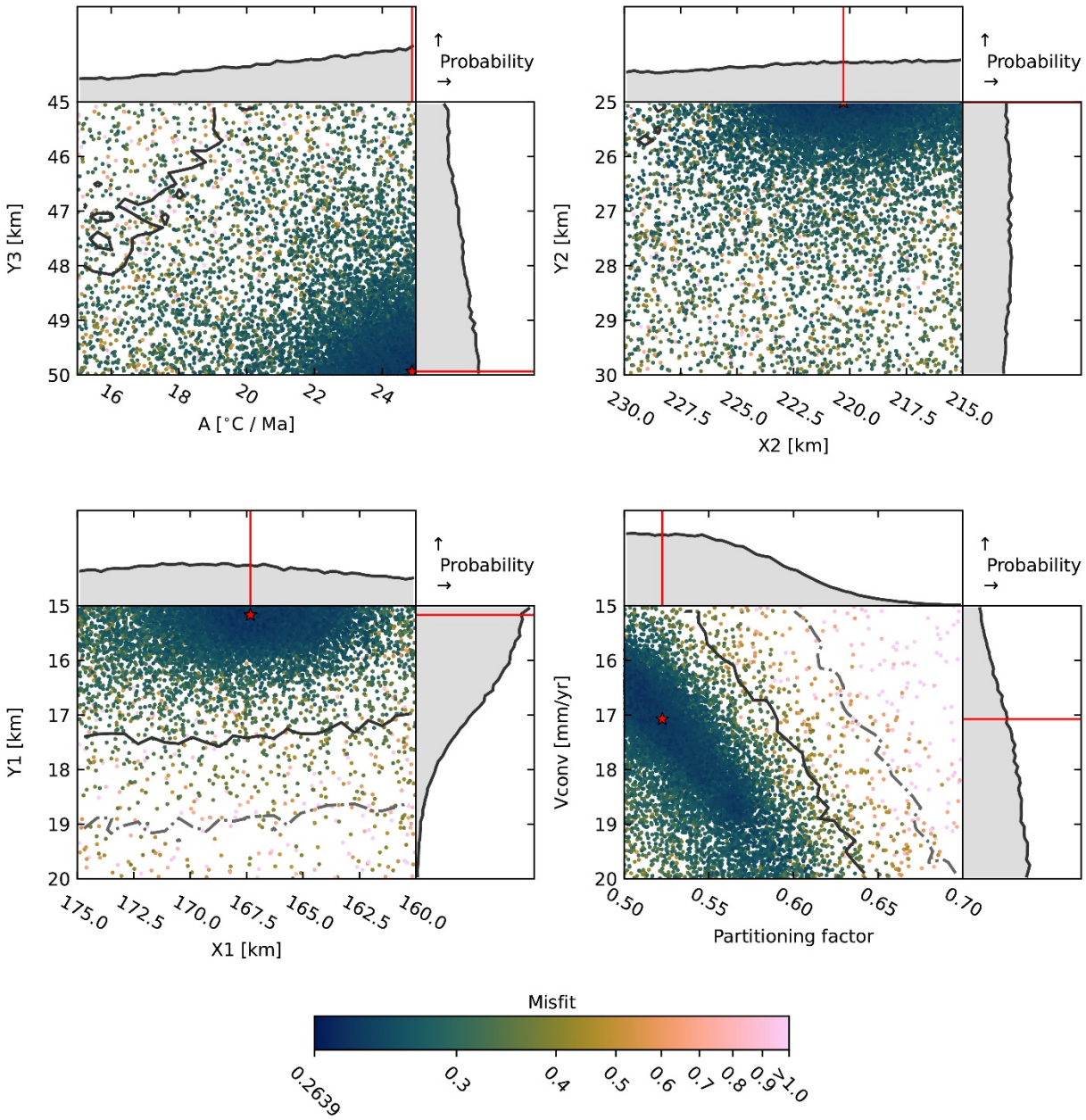

539

Figure 6 Inversion results of model WNP01 solving for 8 free parameters (see Table 3.3) with Y_3 versus A, Y_2 versus X_2, Y_1 versus X_1, and V_{conv} versus λ. Each dot represents a single forward model, and its color corresponds the goodness of fit to the data. The red star represents the parameter values obtained from the forward model with the lowest misfit. One-dimensional posterior probability density functions (1-D PPDFs) derived from the NA appraisal are shown adjacent to the axes for each parameter. The red lines indicate parameter values for the lowest misfit forward model. Two-dimensional PPDFs (2-D PPDFs) are represented by lines overlying the scatter diagram where the solid black line is the 1σ confidence interval and the dashed line the 2σ confidence interval.

540

5.2 Inversion Set WNP02: Slip on the MHT and Localized Enhanced Rock Uplift at Steady Topography

The models in the inversion set WNP02 simulate a scenario where exhumation is caused by a combination of slip along the MHT and localized enhanced uplift by crustal accretion with steady topography (ramp + duplex model). The inversion set comprises 28,820 forward models (Fig. 7). Using a resampling ratio of 80%, the inversion converges to a misfit $\Phi < 0.35$ after approximately 2,000 models. For the best-fit model, the misfit is $\Phi = 0.22$ and the corrected misfit $\Phi_{corr} = 0.55$.

Similar to the inversion set WNP01, the misfit values are sensitive to the convergence rate and underthrusting-overthrusting partitioning factor as suggested by the strongly correlated pattern for the low-misfit forward models on the 2D PPDF plot (Fig. 7). The best-fit model in this set has a convergence rate of 15.48 mm/yr with 0.52% of it accommodated by underthrusting. Both values are broadly consistent with previous studies (Bilham et al., 1997; Jouanne et al., 1999; Larson et al., 1999; Coutand et al., 2014; Landry et al., 2016). The locations of distal and proximal ends of the crustal accretion zone are well-constrained. The rates of localized enhanced uplift and accretion-zone advection are less well-constrained probably due to lack of age constraints in the inversion for the northernmost area. The best-fit mode has a localized enhanced uplifting zone translated at a rate of 5.24 mm/yr to its present location at 189.0 – 203.2 km from the MFT with a vertical crustal accretion rate of 4.01 mm/yr. Due to the existence of an enhanced uplift zone close to the high-slope zone in the model, the dip of the northernmost sector of the MHT, different from the inversion set WNP01, has more freedom in this inversion as suggested by the diffuse distribution of the Y3 values of low-misfit models (Fig. 7). This suggests that the existence and kinematics of a crustal accretion zone plays a more determining role than the dip of the hinterland sector of the MHT. In this inversion, the mid-crustal ramp in the MHT is well-constrained. The best-fit mode has a mid-crustal ramp starting from 149.2 km to 224.6 km from the MFT and has a dip of 7.6° (Fig. 9). The hinterland sector of the MHT in the best-fit model has a dip of 17.0°. The inversion of the heat production parameter also converges to the high end of the given range, with a best-fit value of 24.94 °C/Myr, suggesting a hot orogen.

The comparison between the estimated ages in the best-fit model and the observed ages is shown in Figure 9. Similar to the best-fit model in WNP01 inversion, for the low-temperature systems, the estimated ages also can generally match the observed ages, including the ages not used in the inversion. The large decrease in corrected misfit of the best-fit model compared with the one in WNP01 is mainly contributed by a significantly improved fit for the data cluster close to the high-slope zone (160-185 km). The difference between the observed MsAr ages and predicted ages there are mostly less than 2 Ma. The estimated MsAr ages are younger than the estimation in the best-fit model of the WNP01 inversion, and therefore are more consistent with the young MsAr ages (as young as < 5 Ma) close to the high-slope zone along-strike in other segments (e.g. Copeland et al., 1991; Huntington and Hodges, 2006; Martin et al., 2015; Gibson et al., 2016). The estimated MsAr ages of the samples from the southernmost part of the model also have a good fit with the observed ages (age difference < 1.5 Ma). We interpret that this model is overall successful in producing ages consistent with the observed ages for all age systems discussed.

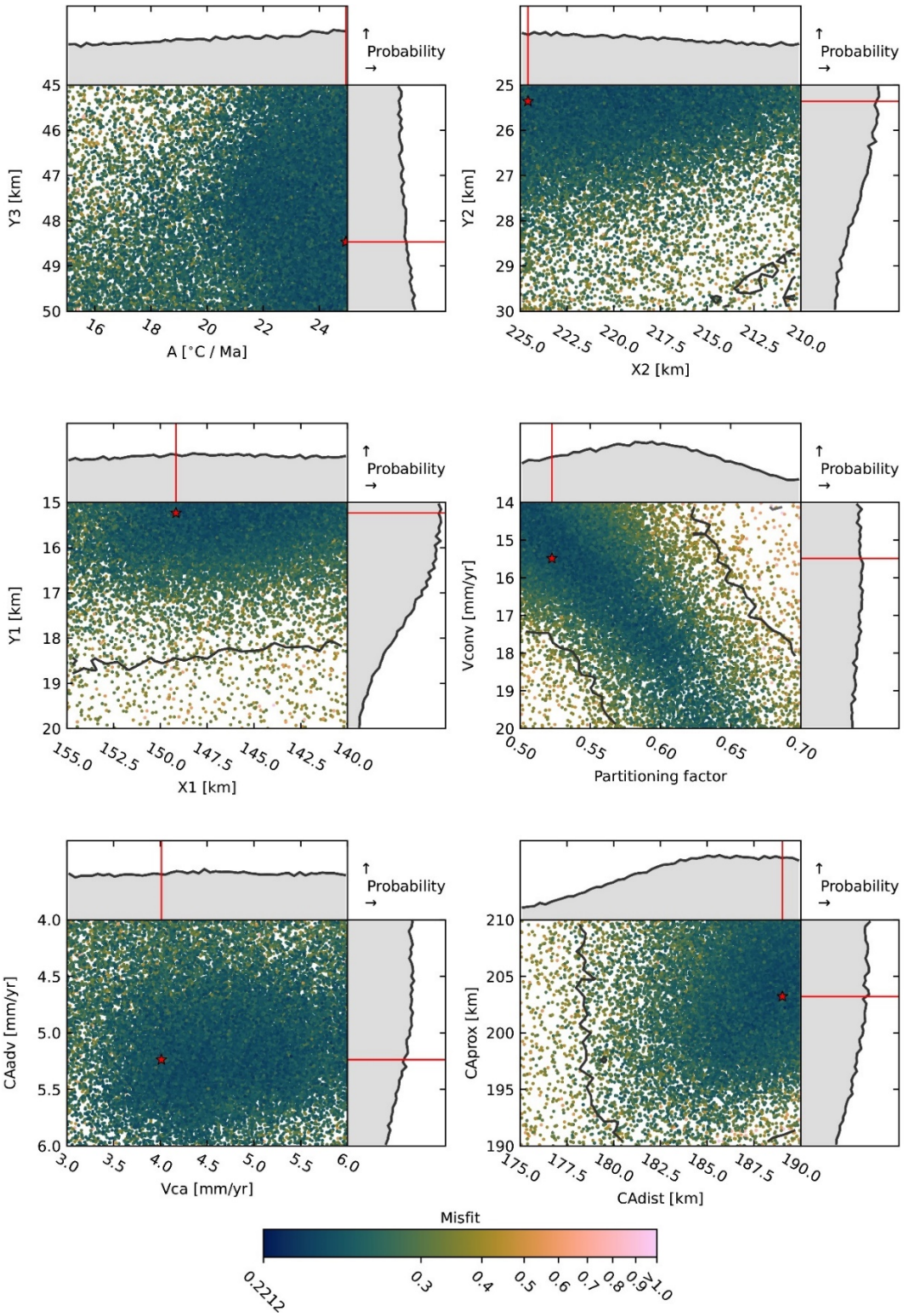

585

Figure 7 Inversion results for model WNP02 solving for 12 parameters (see Table 3.3) with Y_3 versus A, Y_2 versus X_2, Y_1 versus X_1, V_{conv} versus λ, CA_{adv} versus V_{ca}, and CA_{prox} versus CA_{dist}. Symbols are the same as for Figure 6.

586

5.3 Inversion Set WNP03: Slip on the MHT, Localized Enhanced Rock Uplift, and Evolving Topography

The models for inversion set WNP03 simulate a scenario similar to WNP02 except that it has a dynamically evolving topography (ramp + duplex + evolving topography model). Because of the introduction of two parameters defining the evolving topography, to keep the number of parameter-space dimensions unchanged, we use constant values for the vertical coordinates of the hinterland most node of the MHT (Y3 = 50.0 km) and the upper end of the ramp (Y1 = 15.0 km). The value of Y1 is selected based on the consistent Y1 values of the best models in the inversion sets WNP01 and WNP02. We also change Y3 to a constant parameter because the inversion result of WNP02 shows, when crustal accretion is incorporated, Y3 cannot be well-constrained. This inversion set comprises 28,820 forward models. Using a resampling ratio of 80%, the inversion has a worse convergence than the WNP02 inversion set, but it still converges to a misfit $\Phi < 0.35$ after approximately 28,000 models (with only one model exception). The lowest misfit is $\Phi = 0.22$, and the corrected misfit $\Phi_{corr} = 0.55$.

The inversion result is similar to WNP02 in relatively less well-constrained fault-bend locations than WNP01 (related parameters X1, X2, Y2), highly correlated convergence rate (V_{conv}) and underthrusting-overthrusting partitioning factor (λ), well-constrained distal and proximal ends of the crustal accretion zone and uplift rate (CA_{dist} and CA_{prox}), not well-constrained uplift rate and advection velocity of the crustal accretion zone (V_{CA} and CA_{adv}) (Fig. 8). The introduction of inversion for evolving topography makes the distribution of good-fit X1, X2, and Y2 more diffuse than the result of WNP02 in their 2D PPDF plots. The best-fit model has a convergence rate of 14.48 mm/yr. with 50% of it accommodated by underthrusting Both of these values are broadly consistent with previous studies (Bilham et al., 1997; Jouanne et al., 1999; Larson et al., 1999; Coutand et al., 2014; Landry et al., 2016). The best-fit geometry and kinematics of the MHT, including crustal accretion is approximately similar to the best model of WNP02. The best-fit MHT has a shallow-dipping middle crustal ramp of an 8.0° dip, starting from 147.2 km to 224.5 km from the MFT, and a hinterland sector of 17.7°. The best-fit mode has a localized enhanced uplift zone translated at a rate of 5.18 mm/yr to its present location at 189.3 – 203.3 km from the MFT with a vertical crustal accretion rate of 5.00 mm/yr during the last 6 Ma in the model. The inversion of the heat production parameter converges to 24.63 °C/Myr, also indicating a hot orogen. Like the correlation between the convergence rate and partitioning factor of the low-misfit models, the parameters defining the initial topography, A_{topo} and O_{topo}, are also well correlated in a narrow zone on the 2D PPDF plot. The best-fit A_{topo} and O_{topo} are 0.955 and 0.14 km, indicating no significant topographic evolution in the best-fit model.

Between the inversion sets WNP02 and WNP03, the parameters of the best-fit models are not significantly different, and they have the same level of observation-prediction fit (Fig. 9). The pattern in the estimated ages is similar to that of the best-fit model in WNP02. We conclude that this model is overall successful in producing ages consistent with the observed ages for all age systems discussed and that whether the topography significantly evolved over time cannot be determined with the methods used in this study.

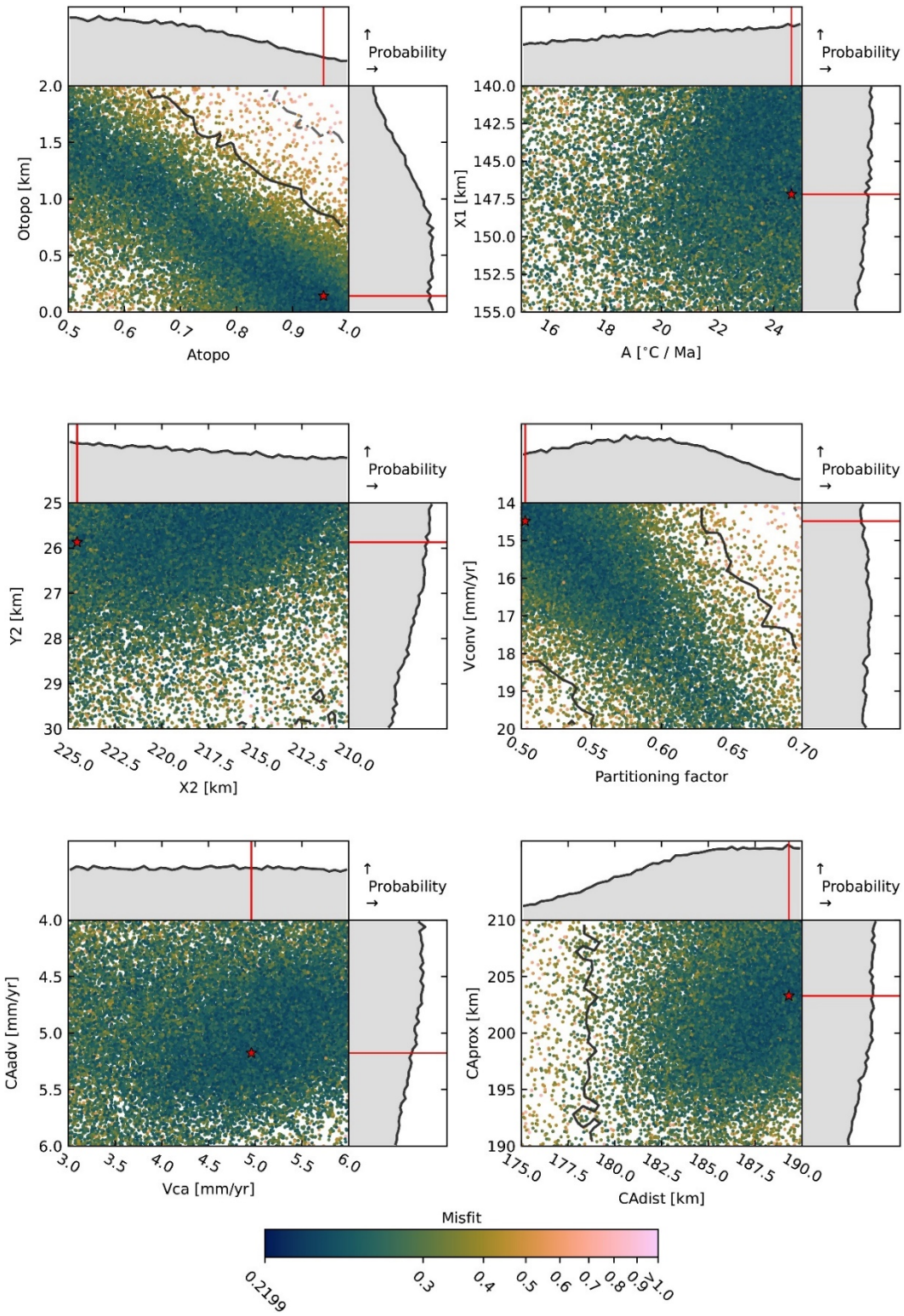

627

Figure 8 Inversion results for model WNP03 solving for 12 parameters (see Table 3.3) with O_{topo} versus A_{topo}, X_1 versus A, Y_2 versus X_2, V_{conv} versus λ, CA_{adv} versus V_{ca}, and CA_{prox} versus CA_{dist}. Symbols are the same as for Figure 6.

628

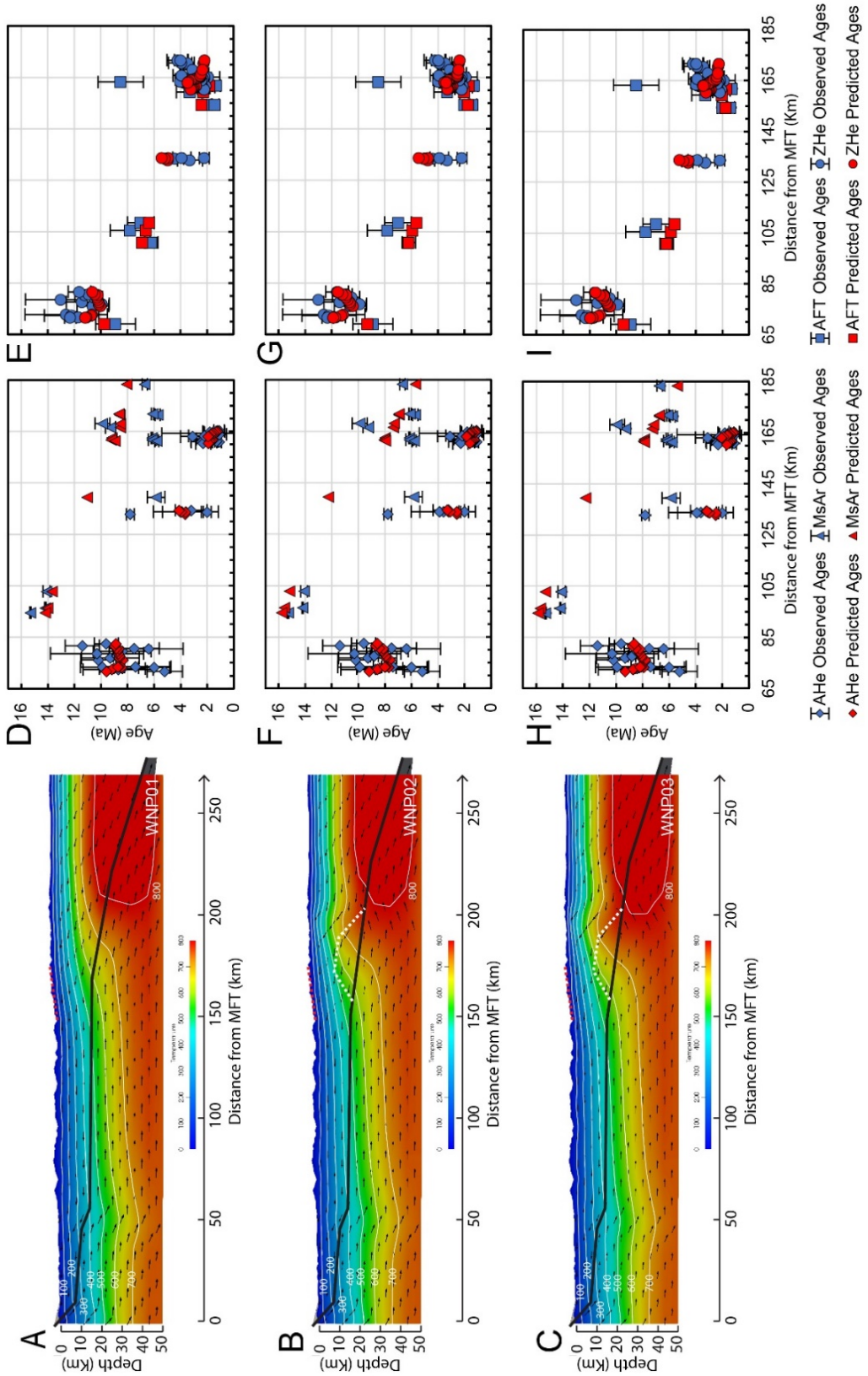

Figure 9 Thermal structures of the best-fit models of the 3 modeled scenarios (A-C) and comparison between the predicted and observed cooling ages for each model (D-I). White dash lines show the amount and location of the crustal accretion along the megathrust. The red dash lines show the high-slope zone on the topography. Black arrows show present snapshot of the velocity field for each model.

629

6 Discussion

6.1 Mid-lower Crustal Duplex Causing Hinterland Exhumation

Comparing the results of the models with and without the involvement of crustal creation shows that mid-lower crustal accretion is required in a model that can produce observation-fitting cooling ages. While each of the three best-fit models can produce good-fit cooling ages of low-temperature systems, only the two best-fit models involving crustal accretion can also produce observation-fitting MsAr ages.

Thermo-kinematic modeling has been used in many studies to test the crustal-accretion model of the exhumation, tectonics, and metamorphism in the Himalayan wedge. Similar work in the central Nepal Himalaya also suggests that a model with crustal accretion along a mid-crustal ramp in the MHT can produce good-fit cooling ages of MsAr, ZHe, and AFT (Herman et al., 2010). The other study in the central Nepal Himalaya used a different version of Pecube which can be coupled with detailed kinematics based on balanced cross-sections to assess different structural reconstructions (Ghoshal et al., 2020). They also found that only models involving hinterland-dipping duplexing and the thrusting of the duplex over a mid-crustal ramp can produce sufficiently rapid exhumation to produce the observed young MsAr ages as well as low-temperature cooling ages. An equivalent study in Sikkim Himalaya by Landry et al. (2016) did not investigate MsAr ages, but, by comparing the model-produced and observed ZHe and AHe ages they also favor a model with crustal accretion. Equivalent studies in Eastern Bhutan, Kumaun, and Garwhal Himalaya did not test competing kinematic models, but confirmed that models involving crustal accretion can produce observation-fitting cooling ages of various geochronometers including MsAr, ZHe, and AFT (Célérier et al., 2009; Grujic et al., 2020). Similar thermokinematic models also invoked duplexing or complex kinematics requiring matter accretion from the subducting plate to the hanging wall of the MCT to produce both the inverted metamorphic gradient recorded in the rocks across the MCT and the exhumation of the LHS (Harrison et al., 1997; Bollinger et al., 2004; Grujic et al., 2020).

Some studies using other approaches also suggest that crustal accretion is a main mechanism accommodating mid-lower crustal strain. Within the MCT thrust sheet, many thrust-sense tectonic or metamorphic discontinuities have been documented (e.g. Montomoli et al., 2013; Larson et al., 2015; Montomoli et al., 2015; Carosi et al., 2016; Carosi et al., 2018). These discontinuities approximately mimic the PT2 on the map and usually correspond to the areas on the foreland limb of the antiformal crustal accretion in the thermokinematic models discussed above, indicating mid-lower crustal strain accumulation. Underplating of the material from the Indian plate to the upper plate is supported by isotopic signatures of the high-grade crystalline rocks in the Gurla Mandhata area along the Northern Himalayan antiform (Murphy, 2007; Godin et al., 2021). Direct observation of a crustal-scale duplex structure on seismic-reflection profiles across the Yarlung-Zangbo suture were documented (Gao et al., 2016; Guo et al., 2018) or reinterpreted (Laskowski et al., 2018). The similar inclinations recorded in the GHS and LHS indicated by the secondary remnant magnetization formed during metamorphism contradict to MCT ramping and rather favors the interpretation of duplex structures (Schill et al., 2004). Landscape evolution simulations in the Bhutan and central Nepal Himalaya suggest that crustal accretion at depth can facilitate in-situ formation of low-relief landscape and a physiographic transition at the front of it (Herman et al., 2010; Adams et al., 2016). Similarly, Fan and Murphy (2021) proposed that strain accumulation in mid-lower crust through duplexing is a mechanism

of plateau outward growth based on the observation that the thick high-grade metamorphic core of the orogen correlates well with the high-elevation, low-relief landscape to the north of the present active-uplift front. Grandin et al. (2012) addressed that the interseismic transient-uplift peak indicated by interferometric synthetic aperture radar data spatially matches the long-term uplift peak indicated by the study on trans-Himalayan river incision in central Nepal. This pattern requires formation of a new crustal ramp via footwall-to-hanging-wall accretion as the old ramp translated towards the hinterland. Similarly, a steady position of the active uplift with respect to the PT2 since ca. 1.5 Ma in northwestern Himalaya is suggested by the spatial similarity of the long- (Ma) and short-term (ka) erosion rates, which lead Morell et al. (2017) to draw the same conclusion.

There are two main groups of studies invoking the ramp model without the involvement of crustal accretion to explain observations from a variety of disciplines, but their data usually cannot represent long-term orogen-building process. The first group used mechanical modeling methods to simulate the deformation depicted by geodetic data within the time span of seismic cycles, but these data record deformation no older than decades (e.g. Jackson and Bilham, 1994; Bilham et al., 1997; Jouanne et al., 1999; Larson et al., 1999; Cattin and Avouac, 2000; Berger et al., 2004; Godard et al., 2004; Elliott et al., 2016). Some of these studies also considered the effects of rheology change and erosion in their models, and compared the model predictions with results of erosion and denudation studies which usually do not account for processes older than Quaternary (Cattin and Avouac, 2000; Lavé and Avouac, 2001; Godard et al., 2004, 2009). The other group of studies that support the ramp model conducted thermokinematic modeling similar to this study, but they usually did not test effect of crustal accretion (Robert et al., 2009; Robert et al., 2011; Coutand et al., 2014). They also used only ages of low-temperature chronometers to test the models which may not be able to determine the feasibility of continuous crustal accretion (this study, Whipp et al., 2007; Ghoshal et al., 2020). Some other studies invoked the ramp model to conceptually explain some geological observations without quantitative test, and therefore do not conflict with the models invoking crustal accretion (e.g. Seeber et al., 1981; Molnar, 1984; Ni and Barazangi, 1984; Beaumont, 2004; van der Beek et al., 2016).

The other competing kinematic model to explain the PT2 and the rapid exhumation along it is the out-of-sequence model (Harrison et al., 1997; Wobus et al., 2003; Hodges et al., 2004; Thiede et al., 2004; Thiede et al., 2005; Wobus et al., 2005; Wobus et al., 2006; Whipple et al., 2016). We did not directly test this model in this study because this model contradicts several independent lines of observations. If there is an active thrust fault accommodating the hinterland active uplift and maintaining the PT2 and rapid exhumation, there should be an abrupt change in the cooling ages across the active fault. However, age profiles along most of the investigated transects do not show an abrupt change, especially for the ages of low-temperature dating systems (e.g. Thiede and Ehlers, 2013; Coutand et al., 2014; Landry et al., 2016; Stübner et al., 2018; McQuarrie et al., 2019; Ghoshal et al., 2020). Although several lines of evidence for active out-of-sequence thrusting or reactivation of the MCT have been reported at several places (e.g. Harrison et al., 1997; Catlos et al., 2001; Wobus et al., 2003; Hodges et al., 2004; Wobus et al., 2005; Wobus et al., 2006; Whipple et al., 2016; Thiede et al., 2017; Braden et al., 2018), no continuous active thrust fault along the generally orogen-wide continuous (> 1,500 km long) PT2 has yet been mapped. Finally, thermokinematic modeling in central Nepal shows that an out-of-sequence model producing observation-fitting exhumation pattern requires either unrealistic fast

718 movement along the thrust fault and the STD or mechanically unfeasible high-dip angle of the
719 thrust fault (Herman et al., 2010).

720 6.2 3D Megathrust Ramps

721 Many studies suggest that the MHT has complex along-strike heterogeneity regarding the
722 dip, location and number of the fault ramps (Hauck et al., 1998; Larson et al., 1999; Robert et al.,
723 2011; Mugnier et al., 2017; Fan and Murphy, 2021). For the western Nepal Himalaya, different
724 MHT geometries from the central Nepal Himalaya have been proposed based on observations
725 from a variety of disciplines, including structural geology (Robinson et al., 2001; Hubbard et al.,
726 2016; DeCelles et al., 2020), thermochronology (Gibson et al., 2016; van der Beek et al., 2016),
727 metamorphism (Soucy La Roche and Godin, 2019), seismicity (Hoste-Colomer et al., 2018), and
728 landscape analysis (Harvey et al., 2015). However, most of these models are conceptual and are
729 not quantitatively constrained. Some models based on balanced cross-sections focus on the
730 structures primarily to the south of the PT2 and do not deal with the mid-lower crustal structures
731 or MHT crustal ramps (e.g. DeCelles et al., 2001; Robinson et al., 2006; Robinson, 2008; Olsen
732 et al., 2019) (Fig. 3). Geophysical data used in interpreting the MHT geometry are usually of
733 poor quality for deep structures in the hinterland (e.g. Caldwell et al., 2013; Subedi et al., 2018).
734 The numerical models in this study provide the first assessment of the MHT hinterland geometry
735 in western Nepal Himalaya from the perspective of thermokinematics.

736 The best models of inversion sets WNP02 and WNP03 are very similar and we consider
737 both to be the preferred models based on their successful prediction of the calculated cooling
738 ages (Fig. 9). The upper-crustal portion of the MHT (shallower than 14 km) are not investigated
739 in this study, and in our model the geometry of this part is adopted from the two-ramp model
740 based on geomorphology, thermochronology, microseismicity, and balanced cross-sections
741 (DeCelles et al., 2001; Harvey et al., 2015; van der Beek et al., 2016; Hoste-Colomer et al.,
742 2018; Olsen et al., 2019). The upper-crustal ramp connects to a long flat at approximately 14-15
743 km deep in our preferred models. This flat is imaged as a midcrustal low-velocity zone from
744 receiver function analysis on teleseismic waveforms (Subedi et al., 2018), and its southern extent
745 is consistent with the distribution of microseismicity (Ader et al., 2012; Hoste-Colomer et al.,
746 2018). At about 149 km to the north of the MFT, this midcrustal flat connects to a not-well-
747 expressed mid-lower crustal ramp, which is consistent with the northward lack of intense
748 microseismicity as the ramp extends beneath seismogenic depths (Fig. 3, 9). A sector of low-
749 velocity zone to the north but discontinuous from the midcrustal flat on the receiver function
750 image also in agreement with the gently dipping mid-lower crustal ramp geometry in our
751 preferred models (Fig. 3). The crustal accretion in our preferred models is on this mid-lower
752 crustal ramp, indicating that PT2-N in western Nepal Himalaya represents the active-uplift front
753 of the high Himalaya plateau, which is consistent with previous interpretations (e.g. Cannon and
754 Murphy, 2014; Fan and Murphy, 2021) (will be discussed in the next section) (Fig. 9). The mid-
755 lower crustal ramp connects to a steeper hinterland ramp at ca. 25 km depth in our preferred
756 models. But this hinterland ramp should be interpreted with caution because no data, including
757 cooling ages, are available to test it. It is possible that it is a trade-off product of the inversion
758 caused by the limitation of the model design: The northern Himalaya anticline is thought to start
759 its thickening process as early as Early-Middle Miocene (e.g. Murphy et al., 2002; Murphy and
760 Copeland, 2005; Godin et al., 2006; Fan and Murphy, 2021) and thus should have thickened via
761 multiple cycles of crustal accretion. However, in the numerical models, we only simulate one

762 accretion cycle. Therefore, the thermal effect of a hot hinterland due to multiple cycles of
763 accretion prior to the simulated last accretion cycle can be compensated by fast exhumation
764 along a steep hinterland ramp in the simulation.

765 Our preferred models are different from the MHT geometry in the central Nepal
766 Himalaya which is characterized by one large mid-lower crustal ramp at approximately 100 km
767 from the MFT. The differences in the number and location of MHT ramps between the western
768 and central Nepal Himalaya require lateral or oblique ramps in the MHT. A 3D conceptual
769 model with a lateral ramp has been invoked to explain the different P-T-t paths of metamorphic
770 rocks from approximately the same structural position but different along-strike segments in
771 western Nepal Himalaya (Soucy La Roche and Godin, 2019). Based on a balanced cross-section
772 in western Nepal and the assumption of an along-strike constant amount of shortening, DeCelles
773 et al. (2020) discussed the 3D evolution of the upper-crustal structures in midwestern Nepal area,
774 but the model does not address the deeper structures in the hinterland. Based on the finding that a
775 balanced cross-section with LHS duplex on a mid-crustal ramp can fit well with the MHT
776 geometry revealed by seismic observations from the 2015 M_w 7.8 Gorkha earthquake, Hubbard
777 et al. (2016) assumed the constant kinematics along-strike and proposed a 3D MHT model for
778 the Nepal Himalaya using the axis of the LHS anticlinorium as a proxy of the top of the mid-
779 lower crustal ramp. Fan and Murphy (2021) synthesized different datasets to propose a 3D
780 evolution model of the MHT in the midwestern Nepal Himalaya and discussed the mechanism of
781 orogenic wedge growth. Their results support the idea that the inner wedge or the orogenic
782 plateau grow outward through crustal accretion at the bottom of the brittle-ductile transition
783 zone, the location of which is mainly controlled by the geometry, especially the mid-lower
784 crustal ramp, of the MHT. This hypothesis predicts that the along-strike variation in the location
785 of active-uplift front of the plateau or the high slope zone is the surface expression of the along-
786 strike variation in MHT geometry.

787 To assess the conceptual 3D MHT model for the mid-western Nepal Himalaya proposed
788 by Fan and Murphy (2021), three questions need to be addressed before assessing the details of
789 the geometry: First, is it true that the mid-lower crustal ramp always controls where the active-
790 uplift front location along the Himalaya? Second, can the high-slope zone represent the active-
791 uplift front of the orogen? Third, which high-slope zone among the two branches in western
792 Nepal Himalaya represent the active-uplift front of that segment?

793 The northern branch of the high-slope zone where the young cooling ages cluster along
794 the modeled transect, is above the upper part of the mid-lower crustal ramp and the southern
795 limb of the antiformal crustal accretion in our preferred models (Fig. 9). Along a transect across
796 the Kathmandu and Anapurna areas, the cooling ages have a similar spatial pattern showing the
797 youngest age cluster located in the high-slope zone is associated with the rapid exhumation
798 caused by crustal accretion on a mid-lower crustal ramp in good-fit thermokinematic models
799 (Herman et al., 2010; Ghoshal et al., 2020). This pattern is not affected by the ca. 60-70 km
800 difference in the distance between the MFT and the ramp or the active-uplift front between the
801 western and central Nepal Himalaya (e.g. Herman et al., 2010; Elliott et al., 2016; Hubbard et al.,
802 2016; Whipple et al., 2016; Ghoshal et al., 2020, and this study). This pattern is also found valid
803 in Kumaun, Annapurna, and Bhutan Himalaya (Whipp et al., 2007; Célérier et al., 2009; Landry
804 et al., 2016). These observations support that the same mechanism may be controlling the
805 tectonomorphology of the whole orogen; the along-strike variation in the location of the active-
806 uplift front can therefore be interpreted as an indicator of the along-strike heterogeneity in the

location of the MHT mid-lower crustal ramp (Fan and Murphy, 2021). The newly reported ages along the northern Himalaya antiform and close to the hinge of the Dolpo synform in western Nepal are older (9.5-12.2 Ma) than those reported along-strike correspondent ages along the modeled transect. In contrast, the ages to the south of the Dolpo synform, generally along the eastern limb of the topographic embayment in mid-western Nepal, are of younger ages (3.1-7.4 Ma), and the youngest age of 3.1 Ma is consistent with the ZHe ages reported along the high slope zone in other sectors of the orogen (Fig. 4). In the Thakkhola graben, published ages also show that the youngest cooling ages are at the high-slope zone and the ages to the north in the inner wedge are relatively old (Fig. 4). Although the southward younging trend of the cooling ages along the footwall of the graben-bounding fault is originally thought to indicate the southward development of the graben (Brubacher et al., 2020), we interpret it as a result of the southward propagation of the crustal thickening for two reasons. First, the graben-bounding fault is very steep and has only accommodated 2.2 km of wedge-parallel extension (Baltz, 2012). Therefore, it is unlikely to significantly affect the thermal structure in the footwall. Second, the cooling ages reported from the footwall of the graben-bounding fault by Brubacher et al. (2020) are very consistent with our new data from the northern Himalaya antiform and from the hinge of the Dolpo syncline, far away from the graben-bounding normal fault. These data support that the active-uplift front of the transitional area along the embayment from far western Nepal to central Nepal is represented by the northern branch of the high-slope zone (Fan and Murphy, 2021).

The details of the conceptual 3D kinematic evolution of the MHT geometry including the ramps and how the MHT coevolved with the morphology of the orogen is described in Fan and Murphy (2021). The 3D kinematics of the fold-thrust-belt in the upper-crustal part in this region is also discussed in DeCelles et al. (2020). Below we integrate these discussions with the surface geology and our modeling results to briefly introduce the main along-strike variations in the MHT ramp geometry of our model for the western Nepal Himalaya (Fig. 10). Along the transect across the apex of the embayment the MHT is characterized by two ramps of which the mid-lower crustal ramp is located further to the hinterland compared with the adjacent segments. The two ramps correlate with PT2-S and PT2-N. In the adjacent areas to the west and to the east of this segment, the MHT is characterized by one mid-crustal ramp located closer to the MFT and it connects up-dip to a deeper flat than the flat in our modeled transect. Oblique or lateral ramps in the mid-lower crust accommodate the along-strike changes in the location of the mid-lower crustal ramps. These oblique or lateral ramps correlate with the abrupt forelandward shift of the MCT and the active-uplift front from the embayment sector to adjacent sectors, and with the along-strike transition between antiformal structures (duplex) and synformal structures (klippe or half klippe). If these lateral ramps started to develop as an older mid-lower crustal ramp below the northern Himalaya anticline propagated towards the foreland differently along-strike as suggested by (Fan and Murphy, 2021), it may have happened at ca. 10 Ma as suggested by the cooling ages along the northern Himalayan anticline (this study and Brubacher et al., 2020). To the east of the town of Juphal, a small lateral ramp may accommodate the further southward shift of the mid-lower crustal ramp. This lateral ramp, though is not expressed in the klippe structure to the south, can be correlated with the shift of the crest of the LHS duplex, the MCT, the STD, and the active-uplift front. The general trend and major step-overs of the WNFS can be correlated well with the general shape of the mid-lower crustal ramps and the lateral and oblique ramps in this model. This supports that the WNFS might have developed partly by exploiting the structures at depth as suggested by Fan and Murphy (2021). The present mid-lower crustal ramp in this model also has a similar pattern to the reconstructed initial upper-crustal frontal ramp

producing the LHS duplex reported in DeCelles et al. (2020), supporting that this upper-crustal ramp may initially bifurcate from a once longer mid-lower crustal ramp as suggested by Fan and Murphy (2021).

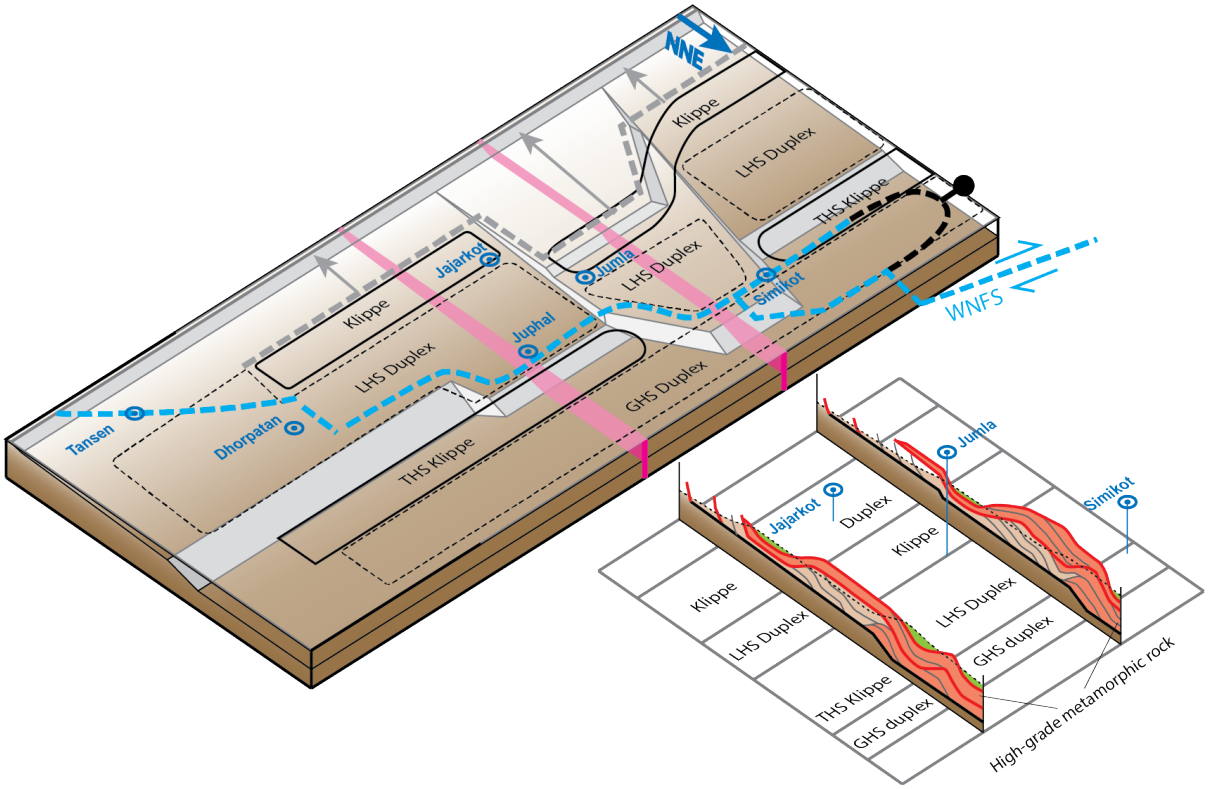

Figure 10 Three-dimensional conceptual model of the MHT in western Nepal Himalaya with two simplified cross-sections show the along-strike variation in first-order structures. Refer to the text for the description and the correlation with main geological features.

6.3 Implications for Orogenic Wedge Growth

Our thermokinematic models employed a different strategy from previous similar studies in adjacent areas to simulate crustal accretion (e.g. Herman et al., 2010; Landry et al., 2016; Grujic et al., 2020). These previous studies used a wide window of crustal accretion at a constant location in the coordinate of the upper plate. However, the location of crustal accretion may change as the orogenic wedge grows. Crustal accretion or duplexing kinematically requires the formation of new crustal slices and their advection to the base of the orogen in the hinterland over successive cycles. Thermo-mechanical models show that each accretion cycle generates transient topographic growth above the crustal ramp which translates with the crustal ramp to the hinterland after their generation, resulting in a permanent increase in the orogen width (Mercier et al., 2017). Considering this kinematics, we used a narrower window of accretion than previous studies but let it advect to the hinterland in a cycle. In this design, the total one-cycle accretion, if plotted in an uplift profile along the transect, has an isosceles trapezoid shape, consistent with the common antiformal shape of a duplex (Fig. 5).

In the inversions, the parameters defining crustal accretion, including the location, accretion rate, and the advection velocity, are independent from the parameters defining the MHT geometry. However, in the best-fit models in the two accretion-involved inversions, the crustal accretion process fit well with many observations. First, the total crustal accretion is in the hinterland above the present mid-lower crustal ramp and it corresponds well with the northern Himalayan anticline, which are consistent with the conceptual model proposed by Fan and Murphy (2021). Second, the hinterland-ward advection of the instantaneous accretion window relative to the matter in upper plate is consistent with the finding of the modeling work in central Nepal Himalaya that to produce the observation-fitting ages a model requires the recent up-dip advection of a duplex structure over a ramp (Ghoshal et al., 2020). Third, the high-slope zone is on the southern flank of antiformal crustal accretion, which is consistent with the geomorphological modeling results that the enhanced uplift caused by duplexing or advection over a ramp can cause the highest river steepness in the forelimb of the uplift zone (Adams et al., 2016; Eizenhöfer et al., 2019). Lastly, the uplift rates caused by the crustal accretion and rock advection over the mid-lower crustal ramp in the preferred models are broadly consistent with previous exhumation-rate studies at different locations in the Himalaya: The preferred models have accretion velocity of ~ 5.2 mm/yr, adding the uplift caused by advection over mid-lower crustal ramp resulting in a total uplift rate of ~ 6.1 mm/yr. The instantaneous velocity is consistent with the observed short-term deformation or erosion, such as geodetic observations at various locations (Jackson et al., 1992; Jackson and Bilham, 1994; Bilham et al., 1997; Grandin et al., 2012); fluvial incision rates estimated from the modern channel geometries (Lavé and Avouac, 2001); and erosion rates estimated from petrographic and mineralogical data of modern river sediments (Garzanti et al., 2007). If considering the time span of one accretion cycle (6 Ma), average uplift rate can be determined by the accretion rate, width of the accretion window, and advection rate of the accretion window in the model. In our preferred models, the temporally average uplift rates of the crest part of the antiformal accretion are about 1.81 mm/yr (WNP02) and 2.24 mm/yr (WNP03), which adding the uplift component caused by advection over the mid-lower crustal ramp results in 2.73 mm/yr and 3.17 mm/yr respectively. They are also broadly consistent with studies on long-term erosion rates, including the results from bedrock thermochronology (Burbank et al., 1996; Burbank et al., 2003; Huntington et al., 2006; Blythe et al., 2007; Adams et al., 2009; Thiede et al., 2009; Thiede and Ehlers, 2013), bedrock thermochronology with thermokinematic modeling (Herman et al., 2010; McCallister et al., 2014; Adams et al., 2015; Landry et al., 2016; Stübner et al., 2018), detrital thermochronology (Brewer et al., 2006; Huntington and Hodges, 2006; Szulc et al., 2006; Copeland et al., 2015). They are also broadly consistent with studies on current average erosion rate in catchment scale determined by cosmogenic nuclides in quartz from river sediments (Vance et al., 2003; Scherler et al., 2014; Ojha et al., 2019) and on geochemical mass-balance of erosion fluxes of modern rivers (Galy and France-Lanord, 2001).

A modified critical taper model predicts that a wedge with brittle-ductile transition in both the wedge and decollement parts can maintain a high slope zone connecting a taper-like outer wedge and a plateau inner wedge at a critical state (Williams et al., 1994). But like the original critical taper model that only considers frictional material (Davis et al., 1983; Dahlen et al., 1984), this model does not address the internal deformation that maintains the wedge shape and self-similar growing process. Many of the previous thermokinematic models highlighting the role of crustal accretion in other Himalayan regions correlate the accretion in their models with the LHS duplex in the footwall of the MCT. Different from these models, our models of the

western Nepal Himalaya suggest the mid-lower crustal accretion causes the thickening the northern Himalayan anticline (Fig. 9), where high-grade metamorphic rocks with protolith from both the GHS and LHS are exposed (Murphy, 2007). However, to the south of the high-slope zone or the active crustal accretion zone above the mid-lower crustal MHT ramp, the LHS duplex is also well-developed and is interpreted to develop by the southward propagation of crustal accretion on an upper-crustal flat (e.g. DeCelles et al., 2001; DeCelles et al., 2020) (Fig. 10). Recently, the LHS duplex is interpreted to be active in central Nepal based on the seismicity data (Mendoza et al., 2019). Further to the foreland, between the MBT and MFT, the older foreland basin strata group (SG) also exhibits duplexes (e.g. Mugnier et al., 1999). A recent study at the rear side of the wedge suggests that thrust duplexing at depth is also active in South Tibet (Taylor et al., 2021). These observations demonstrate that material accretion from the lower plate to the upper plate occurs at different depths with a complex megathrust geometry; the crustal accretion in the mid-lower crust, controlled by the brittle-ductile transition zone along the MHT, may be determining the most active-uplift front and thus the edge of the plateau.

Crustal thickening via multi-layer duplexing is observed or proposed not only in Tibet-Himalayan orogenic system, such as Kunlun range (Wang et al., 2011), Qilian Shan (Zuza et al., 2018), northern Indo-Burma range (Haproff et al., 2020), Yarlung suture (Laskowski et al., 2018), Lhasa terrane (Shi et al., 2020), but also in many other convergent wedges, such as the Franciscan Complex (Platt, 1975), the Appalachian (Ando et al., 1984), and Alaska (Sample and Fisher, 1986; Fuis et al., 1997; Moore et al., 1997; Wissinger et al., 1997; Fuis et al., 2008). These studies provide detailed information about deformation styles and kinematics of wedge or plateau growth. However, how rheologic change and material accretion affect the formation and evolution of a mid-lower crustal ramp and the duplexes above it remains unclear. Due to the limitation of the resolution and computing ability, numerical simulations at the lithospheric scale usually ignore the complex ramp geometries and thus simulate accretion along a single orogen-scale ramp which is seldomly truth in real life (e.g. Mercier et al., 2017; Menant et al., 2020). Numerical and analogue simulations designed for investigating the kinematics of deformation and the evolution of megathrust ramps usually ignore the rheology change along the megathrust and the lower plate deformation as it subducts (e.g. Mugnier et al., 1997; Malavieille, 2010; Dal Zilio et al., 2020b; Ghosh et al., 2020; Shen et al., 2020). These models usually require the preexistence of weak layers in the lower plate to generate duplexes, and the weak layers usually behave as décollements after being involved in the wedge deformation. In these models, once a ramp forms it can only underthrust to the hinterland without deformation in the footwall till a new ramp forms in the foreland. This kinematics may be consistent with the upper-crustal structures but are not true for the evolution of the mid-lower crustal ramps. The formation and sustaining of a mid-lower crustal ramp have been conceptually explained by flexural depression of the lower plate driven by gravity load of the orogen or plateau (Coward, 1983), and mechanical models suggest the strength of the underthrusting lithosphere affects the geometry of the fault (Lyon-Caen and Molnar, 1985; Molnar and Lyon-Caen, 1988).

6.4 Effects of Crustal Accretion on the Landscape of the Himalayan Orogen

The growth of the inner wedge caused by mid-lower crustal accretion may have significantly affected the drainage systems and landscape of the southern edge of the Tibetan plateau. The present landscape of the Himalaya, from north to south, is characterized by the longitudinal Indus and Yarlung river systems, a plateau of high-elevation and low-relief, and an

outer wedge of high-relief landscape, and the extent of these features varies along strike (Fig. 11). The Indus and Yarlung drainage systems are separated from drainage systems within the Tibetan plateau to the north and the outer Himalayan wedge to the south by drainage divides (Fig. 11). Moreover, in the Late Oligocene-Early Miocene, the landscape between the Gangdese range in south Tibet and the Himalaya to the south was characterized by extensive lakes rather than by longitudinal river systems (e.g. DeCelles et al., 2018), and trans-Himalaya rivers existed bringing sediment from the Gangdese range to the Himalayan foreland in the Miocene (e.g. Cina et al., 2009; Lang and Huntington, 2014).

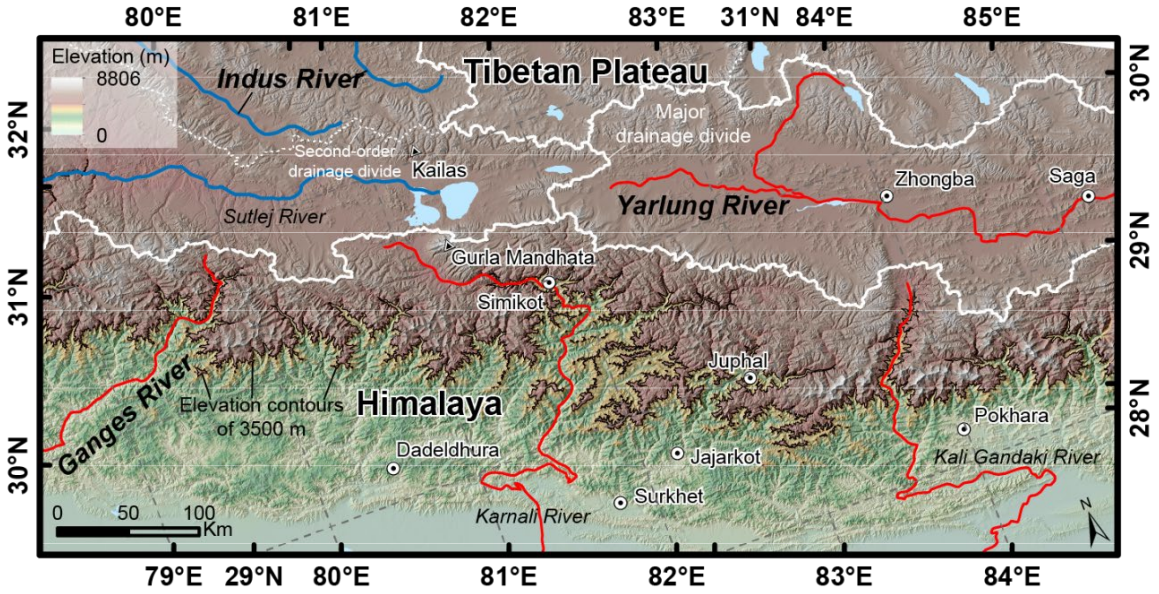

Figure 11 Map shows the topography, landform, and the drainage systems of the central-western Nepal Himalayan and adjacent areas. The blue and red lines represent rivers that flow to Indus fan and Bangel fan respectively. Notice the along-strike change in the width of the orogenic plateau landscape, approximately the area between the 3500 m elevation contours and the southern divides of Indus and Yarlung river systems, and the major drainage divide between the Indus river system and Yarlung river system to the north of the topographic embayment in Simikot segment.

On the northern side of the Himalaya range, the formation of the longitudinal Indus and Yarlung drainage systems may be caused by uplift of the northern Himalaya and shortening on both sides of the present drainage system. On the northern side of the Himalaya along the Indus-Yarlung suture zone, low-altitude warm-water great lakes existed during Oligocene-Miocene time (26-21 Ma) (DeCelles et al., 2018). Early deposition of the Kailas Formation during this period is interpreted to be caused by reginal extension as the subducting slab rolls back (DeCelles et al., 2011; Carrapa et al., 2014), and the detrital sources are mostly the Gangdese range to its north. Late stages of the deposition recorded the addition of the THS source from its south. The change in source is interpreted to be caused by the activation of the north-directed Great Counter thrust at the rear of the Himalaya range. Cooling ages of the Kailas basin suggest post-depositional exhumation at around 17 ± 1 Ma (Carrapa et al., 2014), and is interpreted to reflect the initial rapid incision of the longitudinal river systems. The northern Himalaya anticline may have developed coevally due to mid-lower crustal accretion and ceased in some segment at ca. 10 Ma as our data suggest. Along the suture, studies also suggest crustal duplex at

depth developed from ca. 21-23 Ma (Laskowski et al., 2018). Therefore, we posit that the crustal accretion may have facilitated the development of the river systems (Fig. 12). North-south shortening along the Great Counter thrust and the Gangdese thrust made the area between the Gangdese range and Himalaya range narrow and therefore facilitated localization of the drainage systems. Subsequent crustal accretion along the suture and later the Northern Himalaya anticline, and probably also slab detachment of the subducting plate, caused elevation gain in the area and rapid incision of the Indus and Yarlung river systems. Development of the northern Himalayan anticline may have also terminated some the trans-Himalaya rivers presently represented by wind gaps along the drainage divide between the Himalaya plateau (inner wedge) and the two longitudinal river systems (e.g. Murphy and Burgess, 2006; Buceta et al., 2020).

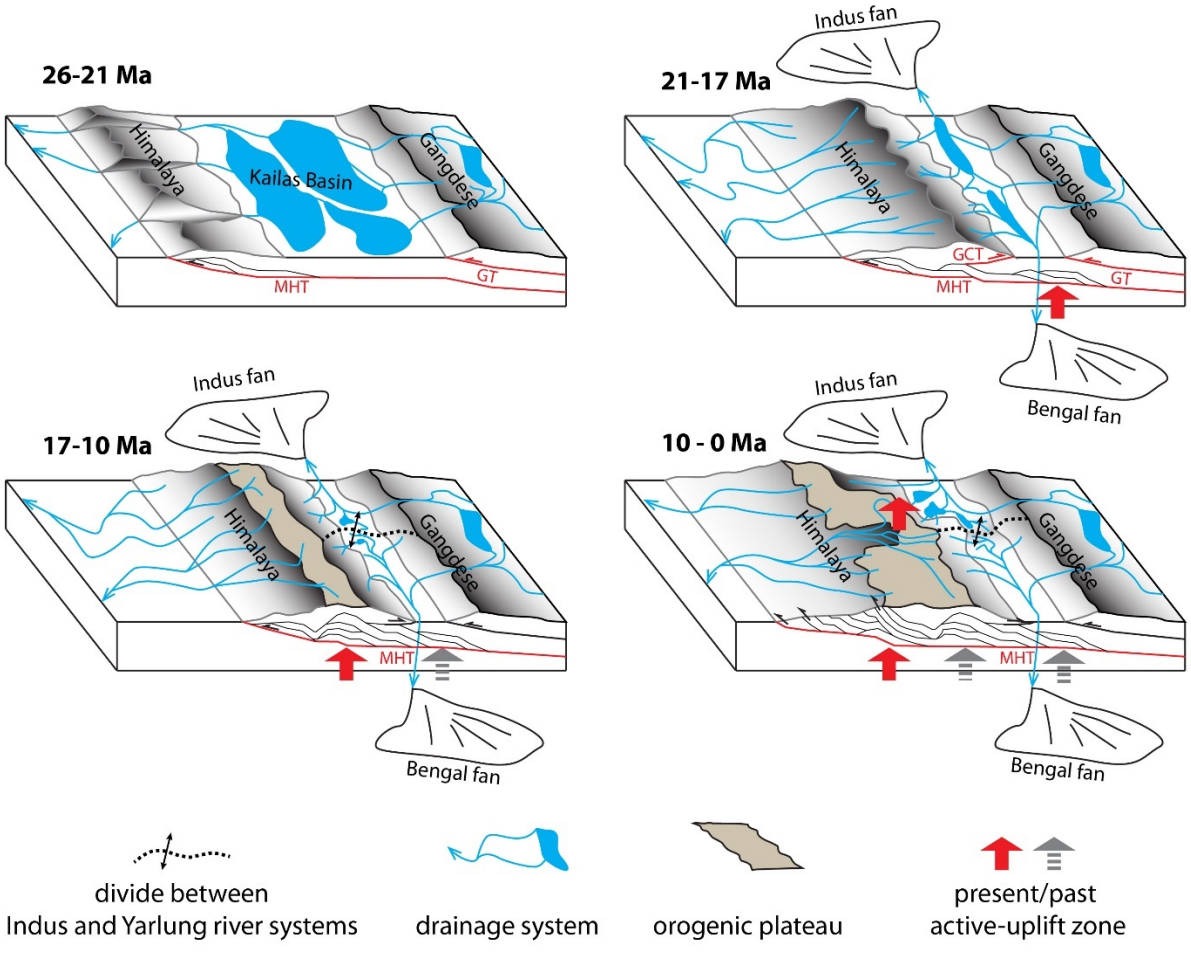

Figure 12 Conceptual evolution model of the drainage system and landscape of the area across the western Nepal Himalaya and adjacent areas.

The Indus and Yarlung river systems extends approximately parallel with the Himalaya at the rear with the Indus river system draining the western part to the west to the Indus fan and the Yarlung river system draining the central-eastern segment to the east to the Bengal fan. The divide between the two river-system catchments is to the north of the topographic embayment in western Nepal (Fig. 11). This raises two questions; how did this divide form and when did it

evolve to its present location? Yin (2006) originally proposed that this drainage divide may have been controlled by subduction of basement ridges in the Indian plate and it might have shifted from ridge to ridge to its current position by headwater erosion. Given that the topographic embayment developed on a structurally high MHT segment which might have pushed the hinterland mid-lower crustal accretion further to the north compared along-strike (this study and Fan and Murphy, 2021), we propose a modified basement-ridge-control model in which the divide may be controlled by this structurally high segment of the MHT, not necessarily the large basement ridges. If this is correct, the divide should have established its present location by ca. 10 Ma, when the mid-lower crustal lateral ramps of the MHT in the embayment area developed. If the drainage systems were affected by the wedge-parallel extension that initiated at ca. 15 Ma in the Gurla Mandhata and Xiao Gurla areas (McCallister et al., 2014), the divide could start to develop at its present location as early as then. This suggests that the divide between the Indus river system and the Yarlung river system may have established its present location approximately right after the river systems formed or localized (Fig. 12).

To the south of the Indus and Yarlung drainage systems, across a drainage divide, the growth of the Himalayan plateau landscape might be controlled by the evolution of mid-lower crustal accretion. In western Nepal, the drainage divide between Yarlung-Brahmputra drainage system and the Himalayan plateau approximately follows the northern Himalaya anticline and the southern edge of the plateau landscape is approximately along the northern limit of the high-slope zone which varies in its location along strike (Fig. 11). Therefore, the width of the inner wedge also varies along the strike. In far-western Nepal along the apex of the topographic embayment, the plateau part is narrow, while in the segment from Dolpo area to the Thakkhola graben, approximately corresponding to the Dolpo THS syncline, the plateau landscape is relatively wide (Fig. 11). If, as discussed in this study and Fan and Murphy (2021), the active-uplift front caused by mid-lower crustal accretion migrated from the northern Himalaya anticline to its present location as lateral or oblique ramps in MHT at mid-lower crustal depth developed, the inner wedge or the plateau landscape might have expanded at the same time with along-strike variation. Two factors could contribute to this process; (1) the southward migration of the mid-lower crustal accretion contributed to build the topography; (2) due to the orographic precipitation effect (Bookhagen and Burbank, 2006), the aridification to the north of the active-uplift front could facilitate the preservation of the plateau landscape built by earlier mid-lower crustal accretion. The coevolution of the mid-lower crustal accretion and plateau expansion is similar to the well-studied forming process of intermontane basins or piggyback basins resulted from the foreland-ward propagation of deformation in fold-and-thrust belts (e.g. Sobel et al., 2003; Hilley and Strecker, 2005; Coutand et al., 2006; Ruetenik et al., 2018; Pingel et al., 2020). This proposed process is also supported by the landscape evolution modeling of the forming process of high-elevation, low-relief landscape patches in the lower Himalaya area via duplex deformation at depth (Adams et al., 2016). The history of the trans-Himalaya rivers that once transported detritus from Gangdese to the Himalayan foreland is not well known, but these rivers could have been blocked as the northern Himalayan anticline and the plateau landscape developed.

7 Conclusion

Our thermokinematic models suggest that the MHT along the Karnali river transect is characterized by two ramps connected by a long upper-crustal flat and a mid-lower crustal ramp

in the hinterland farther to the north with a gentler slope compared with the mid-lower crustal ramps in adjacent segments. The modeling results also suggest that the best-fit models require crustal accretion on the mid-lower crustal ramp to successfully produce observation-fitting cooling ages of MsAr, AFT, ZHe, and AHe dating systems. The youngest cluster of the cooling ages and the high-slope zone of the orogenic wedge are above the forelimb of the antiformal crustal accretion, which is coincidence with the northern Himalaya anticline in far-western Nepal in our model. These findings suggest that the crustal accretion along the mid-lower crustal ramp is controlling the location of the active-uplift front of the orogenic wedge and the migration of the location controls the outward growth of an orogenic plateau. The coexistence of the duplex structures in the upper-crustal depth with the mid-lower crustal accretion we modeled suggests that crustal accretion at different depths or multi-layer duplexing is an important mechanism of maintaining the wedge shape predicted by the critical taper theory.

The ZHe ages reported here from western Nepal Himalaya support that the northern branch of the high-slope zone or the PT2-N is the active-uplift front of the plateau in the area and that its along-strike change in its location is an expression of the along-strike change in MHT geometry. The lateral and oblique ramps in mid-lower crust of a 3-D MHT geometric model for the western Nepal Himalaya on the base of this can be correlated well with the surficial geological features. Cooling ages in this region also suggest that the mid-lower crustal lateral and oblique ramps in MHT started to develop at least by ca. 10 Ma, when the crustal accretion building the northern Himalaya anticline ceased in the segment between the modeled transect and the Thakkhola graben and started to migrate southward to its present location. Integrating other geologic data across the Himalaya, we propose that the deep tectonic process may have controlled the first-order evolution of the landscape and drainage systems, including the transition from the landscape featured by low-elevation big lakes to the localized river systems, the cessation of the trans-Himalaya rivers, the development of the drainage divide between the Indus river system and the Yarlung river system, the southward growth of the inner-wedge plateau landscape with along-strike variations, and the formation of the topographic embayment in western Nepal.

Acknowledgements

This study was funded by National Science Foundation grant (no. 1827863) to Michael Murphy. The authors acknowledge the use of the Sabine Cluster and the advanced support from the Research Computing Data Core at the University of Houston to carry out the research presented here.

References cited in the figure captions are included in the references.

References

Adams, B., Dietsch, C., Owen, L. A., Caffee, M. W., Spotila, J., and Haneberg, W. C., 2009, Exhumation and incision history of the Lahul Himalaya, northern India, based on (U–Th)/He thermochronometry and terrestrial cosmogenic nuclide methods: Geomorphology, v. 107, no. 3, p. 285-299, https://doi.org/https://doi.org/10.1016/j.geomorph.2008.12.017.

Adams, B. A., Hodges, K. V., Whipple, K. X., Ehlers, T. A., van Soest, M. C., and Wartho, J., 2015, Constraints on the tectonic and landscape evolution of the Bhutan Himalaya from thermochronometry: Tectonics, v. 34, no. 6, p. 1329-1347, https://doi.org/10.1002/2015TC003853.

Adams, B. A., Whipple, K. X., Hodges, K. V., and Heimsath, A. M., 2016, In situ development of high-elevation, low-relief landscapes via duplex deformation in the Eastern Himalayan hinterland, Bhutan: Journal of Geophysical Research: Earth Surface, v. 121, no. 2, p. 294-319, https://doi.org/10.1002/2015jf003508.

Ader, T., Avouac, J.-P., Liu-Zeng, J., Lyon-Caen, H., Bollinger, L., Galetzka, J., Genrich, J., Thomas, M., Chanard, K., Sapkota, S. N., Rajaure, S., Shrestha, P., Ding, L., and Flouzat, M., 2012, Convergence rate across the Nepal Himalaya and interseismic coupling on the Main Himalayan Thrust: Implications for seismic hazard: Journal of Geophysical Research, v. 117, no. B4, https://doi.org/10.1029/2011jb009071.

Ando, C. J., Czuchra, B. L., Klemperer, S. L., Brown, L. D., Cheadle, M. J., Cook, F. A., Oliver, J. E., Kaufman, S., Walsh, T., Thompson, J. B., Jr., Lyons, J. B., and Rosenfeld, J. L., 1984, Crustal Profile of Mountain Belt: COCORP Deep Seismic Reflection Profiling in New England Appalachians and Implications for Architecture of Convergent Mountain Chains1: AAPG Bulletin, v. 68, no. 7, p. 819-837, https://doi.org/10.1306/ad461430-16f7-11d7-8645000102c1865d.

Avouac, J.-P., 2003, Mountain building, erosion, and the seismic cycle in the Nepal Himalaya: Advances in geophysics, v. 46, p. 1-80.

Bai, L., Klemperer, S. L., Mori, J., Karplus, M. S., Ding, L., Liu, H., Li, G., Song, B., and Dhakal, S., 2019, Lateral variation of the Main Himalayan Thrust controls the rupture length of the 2015 Gorkha earthquake in Nepal: Science Advances, v. 5, no. 6, p. eaav0723, https://doi.org/10.1126/sciadv.aav0723.

Baltz, T., 2012, Structural evolution of Thakkhola Graben: implications for the architecture of the Central Himalaya, Nepal [Master]: University of Houston.

Baral, U., Lin, D., and Chamlagain, D., 2015, Detrital zircon U–Pb geochronology of the Siwalik Group of the Nepal Himalaya: implications for provenance analysis: International Journal of Earth Sciences, v. 105, no. 3, p. 921-939, https://doi.org/10.1007/s00531-015-1198-7.

Beaumont, C., 2004, Crustal channel flows: 1. Numerical models with applications to the tectonics of the Himalayan-Tibetan orogen: Journal of Geophysical Research, v. 109, no. B6, https://doi.org/10.1029/2003jb002809.

1125 Beaumont, C., Jamieson, R. A., Nguyen, M. H., and Lee, B., 2001, Himalayan tectonics
1126 explained by extrusion of a low-viscosity crustal channel coupled to focused surface
1127 denudation: Nature, v. 414, no. 6865, p. 738-742, https://doi.org/10.1038/414738a.

1128 Bendick, R., and Bilham, R., 2001, How perfect is the Himalayan arc?: Geology, v. 29, no. 9, p.
1129 791-794, https://doi.org/10.1130/0091-7613(2001)029<0791:Hpitha>2.0.Co;2.

1130 Berger, A., Jouanne, F., Hassani, R., and Mugnier, J. L., 2004, Modelling the spatial distribution
1131 of present-day deformation in Nepal: how cylindrical is the Main Himalayan Thrust in
1132 Nepal?: Geophysical Journal International, v. 156, no. 1, p. 94-114,
1133 https://doi.org/10.1111/j.1365-246X.2004.02038.x.

1134 Bernet, M., van der Beek, P., Pik, R., Huyghe, P., Mugnier, J.-L., Labrin, E., and Szulc, A.,
1135 2006, Miocene to Recent exhumation of the central Himalaya determined from combined
1136 detrital zircon fission-track and U/Pb analysis of Siwalik sediments, western Nepal: Basin
1137 Research, v. 18, no. 4, p. 393-412, https://doi.org/10.1111/j.1365-2117.2006.00303.x.

1138 Berthet, T., Hetényi, G., Cattin, R., Sapkota, S. N., Champollion, C., Kandel, T., Doerflinger, E.,
1139 Drukpa, D., Lechmann, S., and Bonnin, M., 2013, Lateral uniformity of India Plate
1140 strength over central and eastern Nepal: Geophysical Journal International, v. 195, no. 3,
1141 p. 1481-1493, https://doi.org/10.1093/gji/ggt357.

1142 Bilham, R., Larson, K., Freymueller, J., Jouanne, F., LeFort, P., Leturmy, P., Mugnier, J. L.,
1143 Gamond, J. F., Glot, J. P., Martinod, J., Chaudury, N. L., Chitrakar, G. R., Gautam, U. P.,
1144 Koirala, B. P., Pandey, M. R., Ranabhat, R., Sapkota, S. N., Shrestha, P. L., Thakuri, M.
1145 C., Timilsina, U. R., Tiwari, D. R., Vidal, G., Vigny, C., Galy, A., and deVoogd, B.,
1146 1997, GPS measurements of present-day convergence across the Nepal Himalaya:
1147 Nature, v. 386, no. 6620, p. 61-64, https://doi.org/10.1038/386061a0.

1148 Blythe, A. E., Burbank, D. W., Carter, A., Schmidt, K., and Putkonen, J., 2007, Plio-Quaternary
1149 exhumation history of the central Nepalese Himalaya: 1. Apatite and zircon fission track
1150 and apatite [U-Th]/He analyses: Tectonics, v. 26, no. 3,
1151 https://doi.org/10.1029/2006tc001990.

1152 Bollinger, L., Avouac, J. P., Beyssac, O., Catlos, E. J., Harrison, T. M., Grove, M., Goffe, B.,
1153 and Sapkota, S., 2004, Thermal structure and exhumation history of the Lesser Himalaya
1154 in central Nepal: Tectonics, v. 23, no. 5, https://doi.org/10.1029/2003tc001564.

1155 Bollinger, L., Henry, P., and Avouac, J., 2006, Mountain building in the Nepal Himalaya:
1156 Thermal and kinematic model: Earth and Planetary Science Letters, v. 244, no. 1-2, p. 58-
1157 71, https://doi.org/10.1016/j.epsl.2006.01.045.

1158 Bollinger, L., Tapponnier, P., Sapkota, S. N., and Klinger, Y., 2016, Slip deficit in central Nepal:
1159 omen for a repeat of the 1344 AD earthquake?: Earth, Planets and Space, v. 68, no. 1, p.
1160 1-12, https://doi.org/10.1186/s40623-016-0389-1.

1161 Bookhagen, B., and Burbank, D. W., 2006, Topography, relief, and TRMM-derived rainfall
1162 variations along the Himalaya: Geophysical Research Letters, v. 33, no. 8,
1163 https://doi.org/10.1029/2006gl026037.

1164 Braden, Z., Godin, L., Cottle, J., and Yakymchuk, C., 2018, Renewed late Miocene (< 8 Ma)
1165 hinterland ductile thrusting, western Nepal Himalaya: Geology, v. 46, no. 6, p. 503-506,
1166 https://doi.org/10.1130/g40097.1.

1167 Braden, Z., Godin, L., Kellett, D. A., and Yakymchuk, C., 2020, Spatio-temporal challenges in
1168 dating orogen-scale shear zones: The case of the Himalayan Main Central thrust:
1169 Tectonophysics, v. 774, p. 228246, https://doi.org/10.1016/j.tecto.2019.228246.

1170 Braun, J., 2003, Pecube: a new finite-element code to solve the 3D heat transport equation
1171 including the effects of a time-varying, finite amplitude surface topography: Computers
1172 & Geosciences, v. 29, no. 6, p. 787-794, https://doi.org/10.1016/S0098-3004(03)00052-9.

1173 Braun, J., van der Beek, P., Valla, P., Robert, X., Herman, F., Glotzbach, C., Pedersen, V., Perry,
1174 C., Simon-Labric, T., and Prigent, C., 2012, Quantifying rates of landscape evolution and
1175 tectonic processes by thermochronology and numerical modeling of crustal heat transport
1176 using PECUBE: Tectonophysics, v. 524–525, p. 1-28,
1177 https://doi.org/10.1016/j.tecto.2011.12.035.

1178 Brewer, I. D., Burbank, D. W., and Hodges, K. V., 2006, Downstream development of a detrital
1179 cooling-age signal: Insights from 40Ar/39Ar muscovite thermochronology in the
1180 Nepalese Himalaya: Geological Society of America Special Papers, v. 398, p. 321-338,
1181 https://doi.org/10.1130/2006.2398(20).

1182 Brubacher, A. D., Larson, K. P., Cottle, J. M., Matthews, W., and Camacho, A., 2020,
1183 Progressive development of E-W extension across the Tibetan plateau: A case study of
1184 the Thakkhola graben, west-central Nepal: International Geology Review, p. 1-20,
1185 https://doi.org/10.1080/00206814.2020.1808860.

1186 Brunel, M., 1986, Ductile thrusting in the Himalayas: Shear sense criteria and stretching
1187 lineations: Tectonics, v. 5, no. 2, p. 247-265, https://doi.org/10.1029/TC005i002p00247.

1188 Buceta, R. E., Schoenbohm, L. M., and DeCelles, P. G., 2020, Glacial and fluvial erosion in the
1189 Dolpo Basin, Western Nepal: Geomorphology, v. 354, p. 107033,
1190 https://doi.org/10.1016/j.geomorph.2020.107033.

1191 Burbank, D. W., Blythe, A. E., Putkonen, J., Pratt-Sitaula, B., Gabet, E., Oskin, M., Barros, A.,
1192 and Ojha, T. P., 2003, Decoupling of erosion and precipitation in the Himalayas: Nature,
1193 v. 426, no. 6967, p. 652-655, https://doi.org/10.1038/nature02187.

1194 Burbank, D. W., Leland, J., Fielding, E., Anderson, R. S., Brozovic, N., Reid, M. R., and
1195 Duncan, C., 1996, Bedrock incision, rock uplift and threshold hillslopes in the
1196 northwestern Himalayas: Nature, v. 379, no. 6565, p. 505-510,
1197 https://doi.org/10.1038/379505a0.

1198 Burchfiel, B. C., Zhiliang, C., Hodges, K. V., Yuping, L., Royden, L. H., Changrong, D., and
1199 Jiene, X., 1992, The South Tibetan Detachment System, Himalayan Orogen: Extension
1200 Contemporaneous With and Parallel to Shortening in a Collisional Mountain Belt:
1201 Geological Society of America Special Papers, v. 269, p. 1-41,
1202 https://doi.org/10.1130/SPE269-p1.

1203 Burg, J. P., Brunel, M., Gapais, D., Chen, G. M., and Liu, G. H., 1984, Deformation of
1204 leucogranites of the crystalline Main Central Sheet in southern Tibet (China): Journal of

1205 Structural Geology, v. 6, no. 5, p. 535-542, https://doi.org/10.1016/0191-8141(84)90063-
1206 4.

1207 Burg, J. P., and Chen, G. M., 1984, Tectonics and Structural Zonation of Southern Tibet, China:
1208 Nature, v. 311, no. 5983, p. 219-223, https://doi.org/10.1038/311219a0.

1209 Caldwell, W. B., Klemperer, S. L., Lawrence, J. F., Rai, S. S., and Ashish, 2013, Characterizing
1210 the Main Himalayan Thrust in the Garhwal Himalaya, India with receiver function CCP
1211 stacking: Earth and Planetary Science Letters, v. 367, p. 15-27,
1212 https://doi.org/10.1016/j.epsl.2013.02.009.

1213 Cannon, J. M., and Murphy, M. A., 2014, Active lower crustal deformation and Himalayan
1214 seismic hazard revealed by stream channels and regional geology: Tectonophysics, v.
1215 633, p. 34-42, https://doi.org/10.1016/j.tecto.2014.06.031.

1216 Cannon, J. M., Murphy, M. A., and Taylor, M., 2018, Segmented strain accumulation in the
1217 High Himalaya expressed in river channel steepness: Geosphere, v. 14, no. 3, p. 1131-
1218 1149, https://doi.org/10.1130/Ges01508.1.

1219 Carosi, R., Lombardo, B., Molli, G., Musumeci, G., and Pertusati, P. C., 1998, The south Tibetan
1220 detachment system in the Rongbuk valley, Everest region. Deformation features and
1221 geological implications: Journal of Asian Earth Sciences, v. 16, no. 2, p. 299-311,
1222 https://doi.org/10.1016/S0743-9547(98)00014-2.

1223 Carosi, R., Montomoli, C., and Iaccarino, S., 2018, 20 years of geological mapping of the
1224 metamorphic core across Central and Eastern Himalayas: Earth-Science Reviews, v. 177,
1225 no. Supplement C, p. 124-138, https://doi.org/10.1016/j.earscirev.2017.11.006.

1226 Carosi, R., Montomoli, C., Iaccarino, S., Massonne, H. J., Rubatto, D., Langone, A., Gemignani,
1227 L., and Visona, D., 2016, Middle to late Eocene exhumation of the Greater Himalayan
1228 Sequence in the Central Himalayas: Progressive accretion from the Indian plate:
1229 Geological Society of America Bulletin, v. 128, no. 11-12, p. 1571-1592,
1230 https://doi.org/10.1130/B31471.1.

1231 Carrapa, B., Orme, D. A., DeCelles, P. G., Kapp, P., Cosca, M. A., and Waldrip, R., 2014,
1232 Miocene burial and exhumation of the India-Asia collision zone in southern Tibet:
1233 Response to slab dynamics and erosion: Geology, v. 42, no. 5, p. 443-446,
1234 https://doi.org/10.1130/g35350.1.

1235 Carrapa, B., Robert, X., DeCelles, P. G., Orme, D. A., Thomson, S. N., and Schoenbohm, L. M.,
1236 2016, Asymmetric exhumation of the Mount Everest region: Implications for the tectono-
1237 topographic evolution of the Himalaya: Geology, https://doi.org/10.1130/g37756.1.

1238 Catlos, E. J., Harrison, T. M., Kohn, M. J., Grove, M., Ryerson, F. J., Manning, C. E., and
1239 Upreti, B. N., 2001, Geochronologic and thermobarometric constraints on the evolution
1240 of the Main Central Thrust, central Nepal Himalaya: Journal of Geophysical Research-
1241 Solid Earth, v. 106, no. B8, p. 16177-16204, https://doi.org/10.1029/2000jb900375.

1242 Catlos, E. J., Lovera, O. M., Kelly, E. D., Ashley, K. T., Harrison, T. M., and Etzel, T., 2018,
1243 Modeling High-Resolution Pressure-Temperature Paths Across the Himalayan Main
1244 Central Thrust (Central Nepal): Implications for the Dynamics of Collision: Tectonics,
1245 https://doi.org/10.1029/2018tc005144.

1246 Cattin, R., and Avouac, J. P., 2000, Modeling mountain building and the seismic cycle in the
1247 Himalaya of Nepal: Journal of Geophysical Research-Solid Earth, v. 105, no. B6, p.
1248 13389-13407, https://doi.org/10.1029/2000jb900032.

1249 Célérier, J., Harrison, T. M., Beyssac, O., Herman, F., Dunlap, W. J., and Webb, A. A. G., 2009,
1250 The Kumaun and Garwhal Lesser Himalaya, India: Part 2. Thermal and deformation
1251 histories: Geological Society of America Bulletin, v. 121, no. 9-10, p. 1281-1297,
1252 https://doi.org/10.1130/b26343.1.

1253 Cina, S. E., Yin, A., Grove, M., Dubey, C. S., Shukla, D. P., Lovera, O. M., Kelty, T. K.,
1254 Gehrels, G. E., and Foster, D. A., 2009, Gangdese arc detritus within the eastern
1255 Himalayan Neogene foreland basin: Implications for the Neogene evolution of the Yalu–
1256 Brahmaputra River system: Earth and Planetary Science Letters, v. 285, no. 1, p. 150-
1257 162, https://doi.org/10.1016/j.epsl.2009.06.005.

1258 Coleman, M., and Hodges, K., 1995, Evidence for Tibetan Plateau Uplift before 14-Myr Ago
1259 from a New Minimum Age for East-West Extension: Nature, v. 374, no. 6517, p. 49-52,
1260 https://doi.org/10.1038/374049a0.

1261 Coleman, M. E., 1996, Orogen-parallel and orogen-perpendicular extension in the central
1262 Nepalese Himalayas: GSA Bulletin, v. 108, no. 12, p. 1594-1607,
1263 https://doi.org/10.1130/0016-7606(1996)108<1594:OPAOPE>2.3.CO;2.

1264 Copeland, P., Bertrand, G., France-Lanord, C., and Sundell, K., 2015, 40Ar/39Ar ages of
1265 muscovites from modern Himalayan rivers: Himalayan evolution and the relative
1266 contribution of tectonics and climate: Geosphere, p. 1837-1858,
1267 https://doi.org/10.1130/ges01154.1.

1268 Copeland, P., Harrison, T. M., Hodges, K. V., Maruéjol, P., Le Fort, P., and Pecher, A., 1991, An
1269 Early Pliocene thermal disturbance of the main central thrust, central Nepal: Implications
1270 for Himalayan tectonics: Journal of Geophysical Research: Solid Earth, v. 96, no. B5, p.
1271 8475-8500, https://doi.org/10.1029/91JB00178.

1272 Cottle, J. M., Larson, K. P., and Kellett, D. A., 2015a, How does the mid-crust accommodate
1273 deformation in large, hot collisional orogens? A review of recent research in the
1274 Himalayan orogen: Journal of Structural Geology, v. 78, p. 119-133,
1275 https://doi.org/10.1016/j.jsg.2015.06.008.

1276 Cottle, J. M., Searle, M. P., Jessup, M. J., Crowley, J. L., and Law, R. D., 2015b, Rongbuk re-
1277 visited: Geochronology of leucogranites in the footwall of the South Tibetan Detachment
1278 System, Everest Region, Southern Tibet: Lithos, v. 227, p. 94-106,
1279 https://doi.org/10.1016/j.lithos.2015.03.019.

1280 Coutand, I., Carrapa, B., Deeken, A., Schmitt, A. K., Sobel, E. R., and Strecker, M. R., 2006,
1281 Propagation of orographic barriers along an active range front: insights from sandstone
1282 petrography and detrital apatite fission-track thermochronology in the intramontane
1283 Angastaco basin, NW Argentina: Basin Research, v. 18, no. 1, p. 1-26,
1284 https://doi.org/10.1111/j.1365-2117.2006.00283.x.

1285 Coutand, I., Whipp, D. M., Grujic, D., Bernet, M., Fellin, M. G., Bookhagen, B., Landry, K. R.,
1286 Ghalley, S. K., and Duncan, C., 2014, Geometry and kinematics of the Main Himalayan
1287 Thrust and Neogene crustal exhumation in the Bhutanese Himalaya derived from

1288 inversion of multithermochronologic data: Journal of Geophysical Research: Solid Earth,
1289 v. 119, no. 2, p. 1446-1481, https://doi.org/10.1002/2013jb010891.

1290 Coward, M. P., 1983, Thrust tectonics, thin skinned or thick skinned, and the continuation of
1291 thrusts to deep in the crust: Journal of Structural Geology, v. 5, no. 2, p. 113-123,
1292 https://doi.org/https://doi.org/10.1016/0191-8141(83)90037-8.

1293 Dahlen, F. A., Suppe, J., and Davis, D., 1984, Mechanics of fold-and-thrust belts and
1294 accretionary wedges: Cohesive Coulomb Theory: Journal of Geophysical Research: Solid
1295 Earth, v. 89, no. B12, p. 10087-10101, https://doi.org/10.1029/JB089iB12p10087.

1296 Dal Zilio, L., Jolivet, R., and van Dinther, Y., 2020a, Segmentation of the Main Himalayan
1297 Thrust illuminated by Bayesian inference of interseismic coupling: Geophysical Research
1298 Letters, v. 47, no. 4, https://doi.org/10.1029/2019gl086424.

1299 Dal Zilio, L., Ruh, J., and Avouac, J.-P., 2020b, Structural Evolution of Orogenic Wedges:
1300 Interplay Between Erosion and Weak Décollements: Tectonics, v. 39, no. 10, p.
1301 e2020TC006210, https://doi.org/10.1029/2020tc006210.

1302 Davis, D., Suppe, J., and Dahlen, F. A., 1983, Mechanics of fold-and-thrust belts and
1303 accretionary wedges: Journal of Geophysical Research, v. 88, no. B2, p. 1153-1172,
1304 https://doi.org/10.1029/JB088iB02p01153.

1305 DeCelles, P. G., Carrapa, B., Ojha, T. P., Gehrels, G. E., and Collins, D., 2020, Structural and
1306 Thermal Evolution of the Himalayan Thrust Belt in Midwestern Nepal, Structural and
1307 Thermal Evolution of the Himalayan Thrust Belt in Midwestern Nepal,
1308 https://doi.org/10.1130/2020.2547(01).

1309 DeCelles, P. G., Castañeda, I. S., Carrapa, B., Liu, J., Quade, J., Leary, R., and Zhang, L., 2018,
1310 Oligocene-Miocene Great Lakes in the India-Asia Collision Zone: Basin Research, v. 30,
1311 p. 228-247, https://doi.org/10.1111/bre.12217.

1312 DeCelles, P. G., and DeCelles, P. C., 2001, Rates of shortening, propagation, underthrusting, and
1313 flexural wave migration in continental orogenic systems: Geology, v. 29, no. 2, p. 135-
1314 138, https://doi.org/10.1130/0091-7613(2001)029<0135:Rospua>2.0.Co;2.

1315 DeCelles, P. G., Kapp, P., Quade, J., and Gehrels, G. E., 2011, Oligocene–Miocene Kailas basin,
1316 southwestern Tibet: Record of postcollisional upper-plate extension in the Indus-Yarlung
1317 suture zone: GSA Bulletin, v. 123, no. 7-8, p. 1337-1362,
1318 https://doi.org/10.1130/B30258.1.

1319 DeCelles, P. G., Robinson, D. M., Quade, J., Ojha, T. P., Garzione, C. N., Copeland, P., and
1320 Upreti, B. N., 2001, Stratigraphy, structure, and tectonic evolution of the Himalayan fold-
1321 thrust belt in western Nepal: Tectonics, v. 20, no. 4, p. 487-509,
1322 https://doi.org/10.1029/2000tc001226.

1323 Duncan, C., Masek, J., and Fielding, E., 2003, How steep are the Himalaya? Characteristics and
1324 implications of along-strike topographic variations: Geology, v. 31, no. 1, p. 75-78,
1325 https://doi.org/10.1130/0091-7613(2003)031<0075:HSATHC>2.0.CO;2.

1326 Duputel, Z., Vergne, J., Rivera, L., Wittlinger, G., Farra, V., and Hetényi, G., 2016, The 2015
1327 Gorkha earthquake: A large event illuminating the Main Himalayan Thrust fault:

Geophysical Research Letters, v. 43, no. 6, p. 2517-2525, https://doi.org/10.1002/2016GL068083.

Edwards, M. A., Kidd, W. S. F., Li, J., Yue, Y., and Clark, M., 1996, Multi-stage development of the southern Tibet detachment system near Khula Kangri. New data from Gonto La: Tectonophysics, v. 260, no. 1, p. 1-19, https://doi.org/10.1016/0040-1951(96)00073-X.

Eizenhöfer, P. R., McQuarrie, N., Shelef, E., and Ehlers, T. A., 2019, Landscape Response to Lateral Advection in Convergent Orogens Over Geologic Time Scales: Journal of Geophysical Research: Earth Surface, v. 124, no. 8, p. 2056-2078, https://doi.org/10.1029/2019jf005100.

Elliott, J. R., Jolivet, R., González, P. J., Avouac, J. P., Hollingsworth, J., Searle, M. P., and Stevens, V. L., 2016, Himalayan megathrust geometry and relation to topography revealed by the Gorkha earthquake: Nature Geoscience, v. 9, no. 2, p. 174-180, https://doi.org/10.1038/ngeo2623.

Eugster, P., Thiede, R. C., Scherler, D., Stübner, K., Sobel, E. R., and Strecker, M. R., 2018, Segmentation of the Main Himalayan Thrust Revealed by Low-Temperature Thermochronometry in the Western Indian Himalaya: Tectonics, v. 37, no. 8, p. 2710-2726, https://doi.org/doi:10.1029/2017TC004752.

Fan, S., and Murphy, M. A., 2021, Three-dimensional strain accumulation and partitioning in an arcuate orogenic wedge: An example from the Himalaya: GSA Bulletin, v. 133, no. 1-2, p. 3-18, https://doi.org/10.1130/b35528.1.

Fuis, G. S., Moore, T. E., Plafker, G., Brocher, T. M., Fisher, M. A., Mooney, W. D., Nokleberg, W. J., Page, R. A., Beaudoin, B. C., Christensen, N. I., Levander, A. R., Lutter, W. J., Saltus, R. W., and Ruppert, N. A., 2008, Trans-Alaska Crustal Transect and continental evolution involving subduction underplating and synchronous foreland thrusting: Geology, v. 36, no. 3, p. 267-270, https://doi.org/10.1130/g24257a.1.

Fuis, G. S., Murphy, J. M., Lutter, W. J., Moore, T. E., Bird, K. J., and Christensen, N. I., 1997, Deep seismic structure and tectonics of northern Alaska: Crustal-scale duplexing with deformation extending into the upper mantle: Journal of Geophysical Research: Solid Earth, v. 102, no. B9, p. 20873-20896, https://doi.org/10.1029/96jb03959.

Gaetani, M., and Garzanti, E., 1991, Multicyclic History of the Northern India Continental Margin (Northwestern Himalaya)(1): AAPG Bulletin, v. 75, no. 9, p. 1427-1446.

Galy, A., and France-Lanord, C., 2001, Higher erosion rates in the Himalaya: Geochemical constraints on riverine fluxes: Geology, v. 29, no. 1, p. 23-26, https://doi.org/10.1130/0091-7613(2001)029<0023:HERITH>2.0.CO;2.

Gansser, A., 1964, Geology of the Himalayas, New York, Wiley Interscience, 289 p.

Gao, R., Lu, Z., Klemperer, S. L., Wang, H., Dong, S., Li, W., and Li, H., 2016, Crustal-scale duplexing beneath the Yarlung Zangbo suture in the western Himalaya: Nature Geoscience, v. 9, no. 7, p. 555-560, https://doi.org/10.1038/ngeo2730.

Garzanti, E., Vezzoli, G., Andò, S., Lavé, J., Attal, M., France-Lanord, C., and DeCelles, P., 2007, Quantifying sand provenance and erosion (Marsyandi River, Nepal Himalaya):

Earth and Planetary Science Letters, v. 258, no. 3–4, p. 500-515, https://doi.org/10.1016/j.epsl.2007.04.010.

Gébelin, A., Mulch, A., Teyssier, C., Jessup, M. J., Law, R. D., and Brunel, M., 2013, The Miocene elevation of Mount Everest: Geology, v. 41, no. 7, p. 799-802, https://doi.org/10.1130/g34331.1.

Ghazoui, Z., Bertrand, S., Vanneste, K., Yokoyama, Y., Nomade, J., Gajurel, A. P., and van der Beek, P. A., 2019, Potentially large post-1505 AD earthquakes in western Nepal revealed by a lake sediment record: Nature Communications, v. 10, no. 1, p. 2258, https://doi.org/10.1038/s41467-019-10093-4.

Ghosh, S., Bose, S., Mandal, N., and Laik, A., 2020, Mid-crustal ramping of the Main Himalayan Thrust in Nepal to Bhutan Himalaya: New insights from analogue and numerical experiments: Tectonophysics, v. 782-783, p. 228425, https://doi.org/10.1016/j.tecto.2020.228425.

Ghoshal, S., McQuarrie, N., Robinson, D. M., Adhikari, D. P., Morgan, L. E., and Ehlers, T. A., 2020, Constraining Central Himalayan (Nepal) Fault Geometry Through Integrated Thermochronology and Thermokinematic Modeling: Tectonics, v. 39, no. 9, p. e2020TC006399, https://doi.org/10.1029/2020tc006399.

Gibson, R., Godin, L., Kellett, D. A., Cottle, J. M., and Archibald, D., 2016, Diachronous deformation along the base of the Himalayan metamorphic core, west-central Nepal: Geological Society of America Bulletin, v. 128, no. 5-6, p. 860-878, https://doi.org/10.1130/B31328.1.

Godard, V., Cattin, R., and Lavé, J., 2004, Numerical modeling of mountain building: Interplay between erosion law and crustal rheology: Geophysical Research Letters, v. 31, no. 23, https://doi.org/10.1029/2004gl021006.

Godard, V., Cattin, R., and Lavé, J., 2009, Erosional control on the dynamics of low-convergence rate continental plateau margins: Geophysical Journal International, v. 179, no. 2, p. 763-777, https://doi.org/10.1111/j.1365-246X.2009.04324.x.

Godin, L., Ahenda, M., Grujic, D., Stevenson, R., and Cottle, J., 2021, Protolith affiliation and tectonometamorphic evolution of the Gurla Mandhata core complex, NW Nepal Himalaya: Geosphere, v. 17, no. 2, p. 626-646, https://doi.org/10.1130/ges02326.1.

Godin, L., Gleeson, T. P., Searle, M. P., Ullrich, T. D., and Parrish, R. R., 2006, Locking of southward extrusion in favour of rapid crustal-scale buckling of the Greater Himalayan sequence, Nar valley, central Nepal: Geological Society, London, Special Publications, v. 268, no. 1, p. 269-292, https://doi.org/10.1144/Gsl.Sp.2006.268.01.13.

Godin, L., Parrish, R. R., Brown, R. L., and Hodges, K. V., 2001, Crustal thickening leading to exhumation of the Himalayan Metamorphic core of central Nepal: Insight from U-Pb Geochronology and 40Ar/39Ar Thermochronology: Tectonics, v. 20, no. 5, p. 729-747, https://doi.org/10.1029/2000tc001204.

Grandin, R., Doin, M. P., Bollinger, L., Pinel-Puyssegur, B., Ducret, G., Jolivet, R., and Sapkota, S. N., 2012, Long-term growth of the Himalaya inferred from interseismic InSAR measurement: Geology, v. 40, no. 12, p. 1059-1062, https://doi.org/10.1130/g33154.1.

1409 Grujic, D., Ashley, K. T., Coble, M. A., Coutand, I., Kellett, D. A., Larson, K. P., Whipp, D. M.,
1410 Gao, M., and Whynot, N., 2020, Deformational Temperatures Across the Lesser
1411 Himalayan Sequence in Eastern Bhutan and Their Implications for the Deformation
1412 History of the Main Central Thrust: Tectonics, v. 39, no. 4, p. e2019TC005914,
1413 https://doi.org/10.1029/2019tc005914.

1414 Guo, X., Gao, R., Zhao, J., Xu, X., Lu, Z., Klemperer, S. L., and Liu, H., 2018, Deep-seated
1415 lithospheric geometry in revealing collapse of the Tibetan Plateau: Earth-Science
1416 Reviews, v. 185, p. 751-762, https://doi.org/10.1016/j.earscirev.2018.07.013.

1417 Haproff, P. J., Odlum, M. L., Zuza, A. V., Yin, A., and Stockli, D. F., 2020, Structural and
1418 Thermochronologic Constraints on the Cenozoic Tectonic Development of the Northern
1419 Indo-Burma Ranges: Tectonics, v. 39, no. 9, p. e2020TC006231,
1420 https://doi.org/10.1029/2020tc006231.

1421 Harrison, T. M., Ryerson, F., Le Fort, P., Yin, A., Lovera, O. M., and Catlos, E., 1997, A late
1422 Miocene-Pliocene origin for the central Himalayan inverted metamorphism: Earth and
1423 Planetary Science Letters, v. 146, no. 1, p. E1-E7.

1424 Harvey, J. E., 2015, Along-strike tectonic variability in the central Himalaya [Ph.D.]: University
1425 of California, Santa Barbara.

1426 Harvey, J. E., Burbank, D. W., and Bookhagen, B., 2015, Along-strike changes in Himalayan
1427 thrust geometry: Topographic and tectonic discontinuities in western Nepal: Lithosphere,
1428 v. 7, no. 5, p. 511-518, https://doi.org/10.1130/l444.1.

1429 Hauck, M. L., Nelson, K. D., Brown, L. D., Zhao, W., and Ross, A. R., 1998, Crustal structure of
1430 the Himalayan orogen at ~90° east longitude from Project INDEPTH deep reflection
1431 profiles: Tectonics, v. 17, no. 4, p. 481-500, https://doi.org/10.1029/98TC01314.

1432 Heim, A., and Gansser, A., 1939, Geological Observations of the Swiss Expedition, Volume 73,
1433 p. 245.

1434 Herman, F., Copeland, P., Avouac, J. P., Bollinger, L., Maheo, G., Le Fort, P., Rai, S., Foster,
1435 D., Pecher, A., Stuwe, K., and Henry, P., 2010, Exhumation, crustal deformation, and
1436 thermal structure of the Nepal Himalaya derived from the inversion of
1437 thermochronological and thermobarometric data and modeling of the topography: Journal
1438 of Geophysical Research-Solid Earth, v. 115, no. B6,
1439 https://doi.org/10.1029/2008jb006126.

1440 Hetenyi, G., Cattin, R., Berthet, T., Le Moigne, N., Chophel, J., Lechmann, S., Hammer, P.,
1441 Drukpa, D., Sapkota, S. N., Gautier, S., and Thinley, K., 2016, Segmentation of the
1442 Himalayas as revealed by arc-parallel gravity anomalies: Sci Rep, v. 6, p. 33866,
1443 https://doi.org/10.1038/srep33866.

1444 Hilley, G. E., and Strecker, M. R., 2005, Processes of oscillatory basin filling and excavation in a
1445 tectonically active orogen: Quebrada del Toro Basin, NW Argentina: GSA Bulletin, v.
1446 117, no. 7-8, p. 887-901, https://doi.org/10.1130/b25602.1.

1447 Hodges, K., Bowring, S., Davidek, K., Hawkins, D., and Krol, M., 1998, Evidence for rapid
1448 displacement on Himalayan normal faults and the importance of tectonic denudation in

1449 the evolution of mountain ranges: Geology, v. 26, no. 6, p. 483-486,
1450 https://doi.org/10.1130/0091-7613(1998)026<0483:efrdoh>2.3.co;2.

1451 Hodges, K. V., Hurtado, J. M., and Whipple, K. X., 2001, Southward extrusion of Tibetan crust
1452 and its effect on Himalayan tectonics: Tectonics, v. 20, no. 6, p. 799-809,
1453 https://doi.org/10.1029/2001TC001281.

1454 Hodges, K. V., Parrish, R. R., Housh, T. B., Lux, D. R., Burchfiel, B. C., Royden, L. H., and
1455 Chen, Z., 1992, Simultaneous Miocene Extension and Shortening in the Himalayan
1456 Orogen: Science, v. 258, no. 5087, p. 1466-1470,
1457 https://doi.org/10.1126/science.258.5087.1466.

1458 Hodges, K. V., Wobus, C., Ruhl, K., Schildgen, T., and Whipple, K., 2004, Quaternary
1459 deformation, river steepening, and heavy precipitation at the front of the Higher
1460 Himalayan ranges: Earth and Planetary Science Letters, v. 220, no. 3-4, p. 379-389,
1461 https://doi.org/10.1016/s0012-821x(04)00063-9.

1462 Hossler, T., Bollinger, L., Sapkota, S. N., Lavé, J., Gupta, R. M., and Kandel, T. P., 2016,
1463 Surface ruptures of large Himalayan earthquakes in Western Nepal: Evidence along a
1464 reactivated strand of the Main Boundary Thrust: Earth and Planetary Science Letters, v.
1465 434, p. 187-196, https://doi.org/10.1016/j.epsl.2015.11.042.

1466 Hoste-Colomer, R., Bollinger, L., Lyon-Caen, H., Adhikari, L. B., Baillard, C., Benoit, A.,
1467 Bhattarai, M., Gupta, R. M., Jacques, E., Kandel, T., Koirala, B. P., Letort, J., Maharjan,
1468 K., Matrau, R., Pandey, R., and Timsina, C., 2018, Lateral variations of the midcrustal
1469 seismicity in western Nepal: Seismotectonic implications: Earth and Planetary Science
1470 Letters, v. 504, p. 115-125, https://doi.org/10.1016/j.epsl.2018.09.041.

1471 Hubbard, J., Almeida, R., Foster, A., Sapkota, S. N., Bürgi, P., and Tapponnier, P., 2016,
1472 Structural segmentation controlled the 2015 Mw7.8 Gorkha earthquake rupture in Nepal:
1473 Geology, v. 44, no. 8, p. 639-642, https://doi.org/10.1130/g38077.1.

1474 Hubbard, M. S., and Harrison, T. M., 1989, 40Ar/39Ar age constraints on deformation and
1475 metamorphism in the main central thrust zone and Tibetan slab, eastern Nepal Himalaya:
1476 Tectonics, v. 8, no. 4, p. 865-880, https://doi.org/10.1029/TC008i004p00865.

1477 Huntington, K. W., Blythe, A. E., and Hodges, K. V., 2006, Climate change and Late Pliocene
1478 acceleration of erosion in the Himalaya: Earth and Planetary Science Letters, v. 252, no.
1479 1–2, p. 107-118, https://doi.org/10.1016/j.epsl.2006.09.031.

1480 Huntington, K. W., and Hodges, K. V., 2006, A comparative study of detrital mineral and
1481 bedrock age-elevation methods for estimating erosion rates: Journal of Geophysical
1482 Research: Earth Surface, v. 111, no. F3, p. n/a-n/a,
1483 https://doi.org/10.1029/2005JF000454.

1484 Hurtado, J. M., Hodges, K. V., and Whipple, K. X., 2001, Neotectonics of the Thakkhola graben
1485 and implications for recent activity on the South Tibetan fault system in the central Nepal
1486 Himalaya: GSA Bulletin, v. 113, no. 2, p. 222-240, https://doi.org/10.1130/0016-
1487 7606(2001)113<0222:NOTTGA>2.0.CO;2.

1488 Husson, L., Bernet, M., Guillot, S., Huyghe, P., Mugnier, J.-L., Replumaz, A., Robert, X., and
1489 Van der Beek, P., 2014, Dynamic ups and downs of the Himalaya: Geology, v. 42, no.
1490 10, p. 839-842, https://doi.org/10.1130/g36049.1.

1491 Hyndman, R. D., Yamano, M., and Oleskevich, D. A., 1997, The seismogenic zone of
1492 subduction thrust faults: Island Arc, v. 6, no. 3, p. 244-260,
1493 https://doi.org/10.1111/j.1440-1738.1997.tb00175.x.

1494 Iaccarino, S., Montomoli, C., Carosi, R., Massonne, H. J., and Visona, D., 2017, Geology and
1495 tectono-metamorphic evolution of the Himalayan metamorphic core: insights from the
1496 Mugu Karnali transect, Western Nepal (Central Himalaya): Journal of Metamorphic
1497 Geology, v. 35, no. 3, p. 301-325, https://doi.org/10.1111/jmg.12233.

1498 Jackson, M., Barrientos, S., Bilham, R., Kyestha, D., and Shrestha, B., 1992, Uplift in the Nepal
1499 Himalaya revealed by Spirit leveling: Geophysical Research Letters, v. 19, no. 15, p.
1500 1539-1542, https://doi.org/10.1029/92gl01638.

1501 Jackson, M., and Bilham, R., 1994, Constraints on Himalayan deformation inferred from vertical
1502 velocity fields in Nepal and Tibet: Journal of Geophysical Research: Solid Earth, v. 99,
1503 no. B7, p. 13897-13912, https://doi.org/10.1029/94jb00714.

1504 Johnston, S. N., Cannon, J. M., and Copeland, P., 2020, Post-Miocene Erosion in Central Nepal
1505 Controlled by Midcrustal Ramp Position, Duplex Growth, and Dynamically Maintained
1506 Elastic Strain: Tectonics, v. 39, no. 12, p. e2020TC006291,
1507 https://doi.org/10.1029/2020TC006291.

1508 Jordan, T. A., and Watts, A. B., 2005, Gravity anomalies, flexure and the elastic thickness
1509 structure of the India–Eurasia collisional system: Earth and Planetary Science Letters, v.
1510 236, no. 3, p. 732-750, https://doi.org/https://doi.org/10.1016/j.epsl.2005.05.036.

1511 Jouanne, F., Mugnier, J. L., Pandey, M. R., Gamond, J. F., Le Fort, P., Serrurier, L., Vigny, C.,
1512 and Avouac, J. P., 1999, Oblique convergence in the Himalayas of western Nepal
1513 deduced from preliminary results of GPS measurements: Geophysical Research Letters,
1514 v. 26, no. 13, p. 1933-1936, https://doi.org/10.1029/1999gl900416.

1515 Jouanne, F., Mugnier, J. L., Sapkota, S. N., Bascou, P., and Pecher, A., 2017, Estimation of
1516 coupling along the Main Himalayan Thrust in the central Himalaya: Journal of Asian
1517 Earth Sciences, v. 133, p. 62-71, https://doi.org/10.1016/j.jseaes.2016.05.028.

1518 Kohn, M. J., 2014, Himalayan Metamorphism and Its Tectonic Implications: Annual Review of
1519 Earth and Planetary Sciences, v. 42, no. 1, p. 381-419, https://doi.org/10.1146/annurev-
1520 earth-060313-055005.

1521 Kohn, M. J., Wieland, M. S., Parkinson, C. D., and Upreti, B. N., 2005, Five generations of
1522 monazite in Langtang gneisses: implications for chronology of the Himalayan
1523 metamorphic core: Journal of Metamorphic Geology, v. 23, no. 5, p. 399-406,
1524 https://doi.org/10.1111/j.1525-1314.2005.00584.x.

1525 Kumar, A., Singh, S. K., Mitra, S., Priestley, K. F., and Dayal, S., 2017, The 2015 April 25
1526 Gorkha (Nepal) earthquake and its aftershocks: implications for lateral heterogeneity on
1527 the Main Himalayan Thrust: Geophysical Journal International, v. 208, no. 2, p. 992-
1528 1008, https://doi.org/10.1093/gji/ggw438.

1529 Landry, K. R., Coutand, I., Whipp, D. M., Grujic, D., and Hourigan, J. K., 2016, Late Neogene
1530 tectonically driven crustal exhumation of the Sikkim Himalaya: Insights from inversion
1531 of multithermochronologic data: Tectonics, v. 35, no. 3, p. 833-859,
1532 https://doi.org/10.1002/2015TC004102.

1533 Lang, K. A., and Huntington, K. W., 2014, Antecedence of the Yarlung–Siang–Brahmaputra
1534 River, eastern Himalaya: Earth and Planetary Science Letters, v. 397, p. 145-158,
1535 https://doi.org/10.1016/j.epsl.2014.04.026.

1536 Larson, K. M., Bürgmann, R., Bilham, R., and Freymueller, J. T., 1999, Kinematics of the India-
1537 Eurasia collision zone from GPS measurements: Journal of Geophysical Research: Solid
1538 Earth, v. 104, no. B1, p. 1077-1093, https://doi.org/10.1029/1998JB900043.

1539 Larson, K. P., Ambrose, T. K., Webb, A. A. G., Cottle, J. M., and Shrestha, S., 2015,
1540 Reconciling Himalayan midcrustal discontinuities: The Main Central thrust system: Earth
1541 and Planetary Science Letters, v. 429, p. 139-146,
1542 https://doi.org/10.1016/j.epsl.2015.07.070.

1543 Larson, K. P., Godin, L., and Price, R. A., 2010, Relationships between displacement and
1544 distortion in orogens: Linking the Himalayan foreland and hinterland in central Nepal:
1545 Geological Society of America Bulletin, v. 122, no. 7-8, p. 1116-1134,
1546 https://doi.org/10.1130/B30073.1.

1547 Laskowski, A. K., Kapp, P., and Cai, F., 2018, Gangdese culmination model: Oligocene–
1548 Miocene duplexing along the India-Asia suture zone, Lazi region, southern Tibet: GSA
1549 Bulletin, v. 130, no. 7-8, p. 1355-1376, https://doi.org/10.1130/B31834.1.

1550 Lavé, J., and Avouac, J. P., 2001, Fluvial incision and tectonic uplift across the Himalayas of
1551 central Nepal: Journal of Geophysical Research, v. 106, no. B11, p. 26561,
1552 https://doi.org/10.1029/2001jb000359.

1553 Le Fort, P., 1975, Himalayas: the collided range. Present knowledge of the continental arc:
1554 American Journal of Science, v. 275, no. 1, p. 1-44.

1555 Lee, J., Hacker, B. R., Dinklage, W. S., Wang, Y., Gans, P., Calvert, A., Wan, J., Chen, W.,
1556 Blythe, A. E., and McClelland, W., 2000, Evolution of the Kangmar Dome, southern
1557 Tibet: Structural, petrologic, and thermochronologic constraints: Tectonics, v. 19, no. 5,
1558 p. 872-895, https://doi.org/10.1029/1999TC001147.

1559 Lee, J., and Whitehouse, M. J., 2007, Onset of mid-crustal extensional flow in southern Tibet:
1560 Evidence from U/Pb zircon ages: Geology, v. 35, no. 1, p. 45-48,
1561 https://doi.org/10.1130/G22842a.1.

1562 Li, S., Wang, Q., Yang, S., Qiao, X., Nie, Z., Zou, R., Ding, K., He, P., and Chen, G., 2018,
1563 Geodetic imaging mega-thrust coupling beneath the Himalaya: Tectonophysics, v. 747-
1564 748, p. 225-238, https://doi.org/https://doi.org/10.1016/j.tecto.2018.08.014.

1565 Liu, G., and Einsele, G., 1994, Sedimentary history of the Tethyan basin in the Tibetan
1566 Himalayas: Geologische Rundschau, v. 83, no. 1, p. 32-61,
1567 https://doi.org/10.1007/Bf00211893.

1568 Lyon-Caen, H., and Molnar, P., 1985, Gravity anomalies, flexure of the Indian Plate, and the
1569 structure, support and evolution of the Himalaya and Ganga Basin: Tectonics, v. 4, no. 6,
1570 p. 513-538, https://doi.org/10.1029/TC004i006p00513.

1571 Malavieille, J., 2010, Impact of erosion, sedimentation, and structural heritage on the structure
1572 and kinematics of orogenic wedges: Analog models and case studies: GSA Today, p. 4-
1573 10, https://doi.org/10.1130/gsatg48a.1.

1574 Marechal, A., Mazzotti, S., Cattin, R., Cazes, G., Vernant, P., Drukpa, D., Thinley, K., Tarayoun,
1575 A., Le Roux-Mallouf, R., Thapa, B. B., Pelgay, P., Gyeltshen, J., Doerflinger, E., and
1576 Gautier, S., 2016, Evidence of interseismic coupling variations along the Bhutan
1577 Himalayan arc from new GPS data: Geophysical Research Letters, p. n/a-n/a,
1578 https://doi.org/10.1002/2016GL071163.

1579 Martin, A. J., Copeland, P., and Benowitz, J. A., 2015, Muscovite40Ar/39Ar ages help reveal the
1580 Neogene tectonic evolution of the southern Annapurna Range, central Nepal: Geological
1581 Society, London, Special Publications, v. 412, no. 1, p. 199-220,
1582 https://doi.org/10.1144/sp412.5.

1583 Martin, A. J., Ganguly, J., and DeCelles, P. G., 2009, Metamorphism of Greater and Lesser
1584 Himalayan rocks exposed in the Modi Khola valley, central Nepal: Contributions to
1585 Mineralogy and Petrology, v. 159, no. 2, p. 203-223, https://doi.org/10.1007/s00410-009-
1586 0424-3.

1587 Masek, J. G., Isacks, B. L., Gubbels, T. L., and Fielding, E. J., 1994, Erosion and tectonics at the
1588 margins of continental plateaus: Journal of Geophysical Research: Solid Earth, v. 99, no.
1589 B7, p. 13941-13956, https://doi.org/10.1029/94jb00461.

1590 McCallister, A. T., Taylor, M. H., Murphy, M. A., Styron, R. H., and Stockli, D. F., 2014,
1591 Thermochronologic constraints on the late Cenozoic exhumation history of the Gurla
1592 Mandhata metamorphic core complex, Southwestern Tibet: Tectonics, v. 33, no. 2, p. 27-
1593 52, https://doi.org/10.1002/2013tc003302.

1594 McDermott, J. A., Whipple, K. X., Hodges, K. V., and van Soest, M. C., 2013, Evidence for
1595 Plio-Pleistocene north-south extension at the southern margin of the Tibetan Plateau,
1596 Nyalam region: Tectonics, v. 32, no. 3, p. 317-333, https://doi.org/10.1002/tect.20018.

1597 McQuarrie, N., Eizenhöfer, P. R., Long, S. P., Tobgay, T., Ehlers, T. A., Blythe, A. E., Morgan,
1598 L. E., Gilmore, M. E., and Dering, G. M., 2019, The Influence of Foreland Structures on
1599 Hinterland Cooling: Evaluating the Drivers of Exhumation in the Eastern Bhutan
1600 Himalaya: Tectonics, v. 0, no. 0, https://doi.org/10.1029/2018tc005340.

1601 Menant, A., Angiboust, S., Gerya, T., Lacassin, R., Simoes, M., and Grandin, R., 2020, Transient
1602 stripping of subducting slabs controls periodic forearc uplift: Nature Communications, v.
1603 11, no. 1, p. 1823, https://doi.org/10.1038/s41467-020-15580-7.

1604 Mendoza, M. M., Ghosh, A., Karplus, M. S., Klemperer, S. L., Sapkota, S. N., Adhikari, L. B.,
1605 and Velasco, A., 2019, Duplex in the Main Himalayan Thrust illuminated by aftershocks
1606 of the 2015 Mw 7.8 Gorkha earthquake: Nature Geoscience,
1607 https://doi.org/10.1038/s41561-019-0474-8.

1608 Mercier, J., 2014, Structure and evolution of orogenic wedges : a multidisciplinary study on the
1609 Himalayan case [Ph.D]: Université de Grenoble.

1610 Mercier, J., Braun, J., and van der Beek, P., 2017, Do along-strike tectonic variations in the
1611 Nepal Himalaya reflect different stages in the accretion cycle? Insights from numerical
1612 modeling: Earth and Planetary Science Letters, v. 472, p. 299-308,
1613 https://doi.org/10.1016/j.epsl.2017.04.041.

1614 Molnar, P., 1984, Structure and tectonics of the Himalaya: Constraints and implications of
1615 geophysical data: Annual Review of Earth and Planetary Sciences, v. 12, no. 1, p. 489-
1616 516.

1617 Molnar, P., and Lyon-Caen, H., 1988, Some simple physical aspects of the support, structure,
1618 and evolution of mountain belts, *in* Clark, J. S. P., Burchfiel, B. C., and Suppe, J., eds.,
1619 Processes in Continental Lithospheric Deformation, Geological Society of America.

1620 Montemagni, C., Montomoli, C., Iaccarino, S., Carosi, R., Jain, A. K., Massonne, H.-J., and
1621 Villa, I. M., 2019, Dating protracted fault activities: microstructures, microchemistry and
1622 geochronology of the Vaikrita Thrust, Main Central Thrust zone, Garhwal Himalaya, NW
1623 India: Geological Society, London, Special Publications, v. 481, no. 1, p. 127-146,
1624 https://doi.org/10.1144/sp481.3.

1625 Montomoli, C., Carosi, R., and Iaccarino, S., 2015, Tectonometamorphic discontinuities in the
1626 Greater Himalayan Sequence: a local or a regional feature?: Geological Society, London,
1627 Special Publications, v. 412, https://doi.org/10.1144/sp412.3.

1628 Montomoli, C., Iaccarino, S., Carosi, R., Langone, A., and Visona, D., 2013,
1629 Tectonometamorphic discontinuities within the Greater Himalayan Sequence in Western
1630 Nepal (Central Himalaya): Insights on the exhumation of crystalline rocks:
1631 Tectonophysics, v. 608, p. 1349-1370, https://doi.org/10.1016/j.tecto.2013.06.006.

1632 Moore, T. E., Wallace, W. K., Mull, C. G., Adams, K. E., Plafker, G., and Nokleberg, W. J.,
1633 1997, Crustal implications of bedrock geology along the Trans-Alaska Crustal Transect
1634 (TACT) in the Brooks Range, northern Alaska: Journal of Geophysical Research: Solid
1635 Earth, v. 102, no. B9, p. 20645-20684, https://doi.org/10.1029/96jb03733.

1636 Morell, K. D., Sandiford, M., Kohn, B., Codilean, A., Fulop, R. H., and Ahmad, T., 2017,
1637 Current strain accumulation in the hinterland of the northwest Himalaya constrained by
1638 landscape analyses, basin-wide denudation rates, and low temperature thermochronology:
1639 Tectonophysics, v. 721, p. 70-89, https://doi.org/10.1016/j.tecto.2017.09.007.

1640 Morell, K. D., Sandiford, M., Rajendran, C. P., Rajendran, K., Alimanovic, A., Fink, D., and
1641 Sanwal, J., 2015, Geomorphology reveals active décollement geometry in the central
1642 Himalayan seismic gap: Lithosphere, v. 7, no. 3, p. 247-256,
1643 https://doi.org/10.1130/l407.1.

1644 Mugnier, J.-L., and Huyghe, P., 2006, Ganges basin geometry records a pre-15 Ma isostatic
1645 rebound of Himalaya: Geology, v. 34, no. 6, p. 445-448,
1646 https://doi.org/10.1130/g22089.1.

1647 Mugnier, J. L., Baby, P., Colletta, B., Vinour, P., Bale, P., and Leturmy, P., 1997, Thrust
1648 geometry controlled by erosion and sedimentation: A view from analogue models:

Geology, v. 25, no. 5, p. 427-430, https://doi.org/10.1130/0091-7613(1997)025<0427:tgcbea>2.3.co;2.

Mugnier, J. L., Jouanne, F., Bhattarai, R., Cortes-Aranda, J., Gajurel, A., Leturmy, P., Robert, X., Upreti, B., and Vassallo, R., 2017, Segmentation of the Himalayan megathrust around the Gorkha earthquake (25 April 2015) in Nepal: Journal of Asian Earth Sciences, v. 141, p. 236-252, https://doi.org/10.1016/j.jseaes.2017.01.015.

Mugnier, J. L., Leturmy, P., Mascle, G., Huyghe, P., Chalaron, E., Vidal, G., Husson, L., and Delcaillau, B., 1999, The Siwaliks of western Nepal: I. Geometry and kinematics: Journal of Asian Earth Sciences, v. 17, no. 5–6, p. 629-642, https://doi.org/10.1016/S1367-9120(99)00038-3.

Murphy, M. A., 2007, Isotopic characteristics of the Gurla Mandhata metamorphic core complex: Implications for the architecture of the Himalayan orogen: Geology, v. 35, no. 11, p. 983-986, https://doi.org/10.1130/g23774a.1.

Murphy, M. A., and Burgess, W. P., 2006, Geometry, kinematics, and landscape characteristics of an active transtension zone, Karakoram fault system, Southwest Tibet: Journal of Structural Geology, v. 28, no. 2, p. 268-283, https://doi.org/10.1016/j.jsg.2005.10.009.

Murphy, M. A., and Copeland, P., 2005, Transtensional deformation in the central Himalaya and its role in accommodating growth of the Himalayan orogen: Tectonics, v. 24, no. 4, p. TC4012, https://doi.org/10.1029/2004tc001659.

Murphy, M. A., and Harrison, M. T., 1999, Relationship between leucogranites and the Qomolangma detachment in the Rongbuk Valley, south Tibet: Geology, v. 27, no. 9, p. 831-834, https://doi.org/10.1130/0091-7613(1999)027<0831:rblatq>2.3.co;2.

Murphy, M. A., Taylor, M. H., Gosse, J., Silver, C. R. P., Whipp, D. M., and Beaumont, C., 2014, Limit of strain partitioning in the Himalaya marked by large earthquakes in western Nepal: Nature Geoscience, v. 7, no. 1, p. 38-42, https://doi.org/10.1038/Ngeo2017.

Murphy, M. A., and Yin, A., 2003, Structural evolution and sequence of thrusting in the Tethyan fold-thrust belt and Indus-Yalu suture zone, southwest Tibet: Geological Society of America Bulletin, v. 115, no. 1, p. 21-34, https://doi.org/10.1130/0016-7606(2003)115<0021:Seasot>2.0.Co;2.

Murphy, M. A., Yin, A., Kapp, P., Harrison, T. M., Manning, C. E., Ryerson, F. J., Ding, L., and Guo, J. H., 2002, Structural evolution of the Gurla Mandhata detachment system, southwest Tibet: Implications for the eastward extent of the Karakoram fault system: Geological Society of America Bulletin, v. 114, no. 4, p. 428-447, https://doi.org/10.1130/0016-7606(2002)114<0428:Seotgm>2.0.Co;2.

Myrow, P. M., Hughes, N. C., Searle, M. P., Fanning, C. M., Peng, S. C., and Parcha, S. K., 2009, Stratigraphic correlation of Cambrian–Ordovician deposits along the Himalaya: Implications for the age and nature of rocks in the Mount Everest region: Geological Society of America Bulletin, v. 121, no. 3-4, p. 323-332, https://doi.org/10.1130/b26384.1.

Nábělek, J., Hetényi, G., Vergne, J., Sapkota, S., Kafle, B., Jiang, M., Su, H., Chen, J., Huang, B.-S., and Team, t. H.-C., 2009, Underplating in the Himalaya-Tibet Collision Zone

1690 Revealed by the Hi-CLIMB Experiment: Science, v. 325, no. 5946, p. 1371-1374,
1691 https://doi.org/10.1126/science.1167719.

1692 Nadin, E. S., and Martin, A. J., 2012, Apatite thermochronometry within a knickzone near the
1693 Higher Himalaya front, central Nepal: No resolvable fault motion in the past one million
1694 years: Tectonics, v. 31, no. 2, https://doi.org/10.1029/2011tc003000.

1695 Nagy, C., Godin, L., Antolín, B., Cottle, J., and Archibald, D., 2015, Mid-Miocene initiation of
1696 orogen-parallel extension, NW Nepal Himalaya: Lithosphere, v. 7, no. 5, p. 483-502,
1697 https://doi.org/10.1130/l425.1.

1698 Ni, J., and Barazangi, M., 1984, Seismotectonics of the Himalayan Collision Zone: Geometry of
1699 the underthrusting Indian Plate beneath the Himalaya: Journal of Geophysical Research:
1700 Solid Earth, v. 89, no. B2, p. 1147-1163, https://doi.org/10.1029/JB089iB02p01147.

1701 Ojha, L., Ferrier, K. L., and Ojha, T., 2019, Millennial-scale denudation rates in the Himalaya of
1702 Far Western Nepal: Earth Surface Dynamics, v. 7, no. 4, p. 969-987,
1703 https://doi.org/10.5194/esurf-7-969-2019.

1704 Olsen, J. E. S., McQuarrie, N., and Robinson, D. M., 2019, Determining kinematic order and
1705 relative age of faulting via flexural-kinematic restoration: A case study in far western
1706 Nepal: Basin Research, https://doi.org/10.1111/bre.12362.

1707 Pearson, O. N., and DeCelles, P. G., 2005, Structural geology and regional tectonic significance
1708 of the Ramgarh thrust, Himalayan fold-thrust belt of Nepal: Tectonics, v. 24, no. 4,
1709 https://doi.org/10.1029/2003tc001617.

1710 Pêcher, A., 1989, The Metamorphism in the Central Himalaya: Journal of Metamorphic
1711 Geology, v. 7, no. 1, p. 31-41, https://doi.org/10.1111/j.1525-1314.1989.tb00573.x.

1712 Pingel, H., Strecker, M. R., Mulch, A., Alonso, R. N., Cottle, J., and Rohrmann, A., 2020, Late
1713 Cenozoic topographic evolution of the Eastern Cordillera and Puna Plateau margin in the
1714 southern Central Andes (NW Argentina): Earth and Planetary Science Letters, v. 535, p.
1715 116112, https://doi.org/https://doi.org/10.1016/j.epsl.2020.116112.

1716 Platt, J. P., 1975, Metamorphic and deformational processes in the Franciscan Complex,
1717 California: Some insights from the Catalina Schist terrane: Geological Society of
1718 America Bulletin, v. 86, no. 10, p. 1337-1347, https://doi.org/10.1130/0016-
1719 7606(1975)86<1337:Madpit>2.0.Co;2.

1720 Reiners, P. W., 2005, Zircon (U-Th)/He Thermochronometry: Reviews in Mineralogy and
1721 Geochemistry, v. 58, no. 1, p. 151-179, https://doi.org/10.2138/rmg.2005.58.6.

1722 Reiners, P. W., Spell, T. L., Nicolescu, S., and Zanetti, K. A., 2004, Zircon (U-Th)/He
1723 thermochronometry: He diffusion and comparisons with 40Ar/39Ar dating: Geochimica
1724 et Cosmochimica Acta, v. 68, no. 8, p. 1857-1887,
1725 https://doi.org/https://doi.org/10.1016/j.gca.2003.10.021.

1726 Rickwood, P., and Sambridge, M., 2006, Efficient parallel inversion using the Neighbourhood
1727 Algorithm: Geochemistry, Geophysics, Geosystems, v. 7, no. 11, p. n/a-n/a,
1728 https://doi.org/10.1029/2006gc001246.

1729 Robert, X., van der Beek, P., Braun, J., Perry, C., Dubille, M., and Mugnier, J. L., 2009,
1730 Assessing Quaternary reactivation of the Main Central thrust zone (central Nepal

1731 Himalaya): New thermochronologic data and numerical modeling: Geology, v. 37, no. 8,
1732 p. 731-734, https://doi.org/10.1130/G25736a.1.

1733 Robert, X., van der Beek, P., Braun, J., Perry, C., and Mugnier, J. L., 2011, Control of
1734 detachment geometry on lateral variations in exhumation rates in the Himalaya: Insights
1735 from low-temperature thermochronology and numerical modeling: Journal of
1736 Geophysical Research-Solid Earth, v. 116, no. B5, https://doi.org/10.1029/2010jb007893.

1737 Robinson, D. M., 2008, Forward modeling the kinematic sequence of the central Himalayan
1738 thrust belt, western Nepal: Geosphere, v. 4, no. 5, p. 785,
1739 https://doi.org/10.1130/ges00163.1.

1740 Robinson, D. M., DeCelles, P. G., and Copeland, P., 2006, Tectonic evolution of the Himalayan
1741 thrust belt in western Nepal: Implications for channel flow models: Geological Society of
1742 America Bulletin, v. 118, no. 7-8, p. 865-885, https://doi.org/10.1130/B25911.1.

1743 Robinson, D. M., DeCelles, P. G., Garzione, C. N., Pearson, O. N., Harrison, T. M., and Catlos,
1744 E. J., 2003, Kinematic model for the Main Central thrust in Nepal: Geology, v. 31, no. 4,
1745 p. 359-362, https://doi.org/10.1130/0091-7613(2003)031<0359:kmftmc>2.0.co;2.

1746 Robinson, D. M., DeCelles, P. G., Patchett, P. J., and Garzione, C. N., 2001, The kinematic
1747 evolution of the Nepalese Himalaya interpreted from Nd isotopes: Earth and Planetary
1748 Science Letters, v. 192, no. 4, p. 507-521, https://doi.org/10.1016/S0012-
1749 821X(01)00451-4.

1750 Robinson, D. M., and McQuarrie, N., 2012, Pulsed deformation and variable slip rates within the
1751 central Himalayan thrust belt: Lithosphere, v. 4, no. 5, p. 449-464,
1752 https://doi.org/10.1130/l204.1.

1753 Ruetenik, G. A., Hoke, G. D., Moucha, R., and Val, P., 2018, Regional landscape response to
1754 thrust belt dynamics: The Iglesia basin, Argentina: Basin Research, v. 30, no. 6, p. 1141-
1755 1154, https://doi.org/10.1111/bre.12295.

1756 Sakai, H., Iwano, H., Danhara, T., Hirata, T., and Takigami, Y., 2013, Emplacement of hot
1757 Lesser Himalayan nappes from 15 to 10 Ma in the Jumla–Surkhet region, western Nepal,
1758 and their thermal imprint on the underlying Early Miocene fluvial Dumri Formation:
1759 Island Arc, v. 22, no. 3, p. 361-381, https://doi.org/10.1111/iar.12030.

1760 Sambridge, M., 1999a, Geophysical inversion with a neighbourhood algorithm—I. Searching a
1761 parameter space: Geophysical Journal International, v. 138, no. 2, p. 479-494,
1762 https://doi.org/10.1046/j.1365-246X.1999.00876.x.

1763 Sambridge, M., 1999b, Geophysical inversion with a neighbourhood algorithm—II. Appraising
1764 the ensemble: Geophysical Journal International, v. 138, no. 3, p. 727-746,
1765 https://doi.org/10.1046/j.1365-246x.1999.00900.x.

1766 Sample, J. C., and Fisher, D. M., 1986, Duplex accretion and underplating in an ancient
1767 accretionary complex, Kodiak Islands, Alaska: Geology, v. 14, no. 2, p. 160-163,
1768 https://doi.org/10.1130/0091-7613(1986)14<160:Daauia>2.0.Co;2.

1769 Schelling, D., 1992, The Tectonostratigraphy and Structure of the Eastern Nepal Himalaya:
1770 Tectonics, v. 11, no. 5, p. 925-943, https://doi.org/10.1029/92tc00213.

1771 Scherler, D., Bookhagen, B., and Strecker, M. R., 2014, Tectonic control on 10Be-derived
1772 erosion rates in the Garhwal Himalaya, India: Journal of Geophysical Research: Earth
1773 Surface, v. 119, no. 2, p. 83-105, https://doi.org/10.1002/2013JF002955.

1774 Schill, E., Appel, E., Crouzet, C., Gautam, P., Wehland, F., and Staiger, M., 2004, Oroclinal
1775 bending versus regional significant clockwise rotations in the Himalayan arc—
1776 Constraints from secondary pyrrhotite remanences: Geological Society of America
1777 Special Papers, v. 383, p. 73-85, https://doi.org/10.1130/0-8137-2383-
1778 3(2004)383[73:obvrsc]2.0.co;2.

1779 Searle, M. P., and Godin, L., 2003, The South Tibetan Detachment and the Manaslu
1780 Leucogranite: A structural reinterpretation and restoration of the Annapurna-Manaslu
1781 Himalaya, Nepal: Journal of Geology, v. 111, no. 5, p. 505-523,
1782 https://doi.org/10.1086/376763.

1783 Seeber, L., Armbruster, J. G., and Quittmeyer, R. C., 1981, Seismicity and continental
1784 subduction in the Himalayan arc, Zagros, Hindu Kush, Himalaya: Geodynamic
1785 Evolution, p. 215-242, https://doi.org/10.1029/GD003p0215.

1786 Seeber, L., and Gornitz, V., 1983, River profiles along the Himalayan arc as indicators of active
1787 tectonics: Tectonophysics, v. 92, no. 4, p. 335-367, https://doi.org/10.1016/0040-
1788 1951(83)90201-9.

1789 Shen, L., Jia, D., Zhang, Z., Chen, Z., Yin, H., Wu, X., Wang, Y., Sun, C., Cui, J., and Fan, X.,
1790 2020, Tectonic underplating versus out-of-sequence thrusting beneath the Lesser
1791 Himalaya: Insights from the analogue modeling of the Nepal Himalaya fold-and-thrust
1792 belt: Journal of Asian Earth Sciences, v. 198, p. 104167,
1793 https://doi.org/10.1016/j.jseaes.2019.104167.

1794 Shi, Z., Gao, R., Li, W., Lu, Z., and Li, H., 2020, Cenozoic crustal-scale duplexing and flat
1795 Moho in southern Tibet: Evidence from reflection seismology: Tectonophysics, v. 790,
1796 https://doi.org/10.1016/j.tecto.2020.228562.

1797 Sobel, E. R., Hilley, G. E., and Strecker, M. R., 2003, Formation of internally drained
1798 contractional basins by aridity-limited bedrock incision: Journal of Geophysical
1799 Research: Solid Earth, v. 108, no. B7, https://doi.org/10.1029/2002jb001883.

1800 Soucy La Roche, R., and Godin, L., 2019, Inherited Cross-Strike Faults and Oligocene-Early
1801 Miocene Segmentation of the Main Himalayan Thrust, West Nepal: Journal of
1802 Geophysical Research: Solid Earth, v. 124, no. 7, p. 7429-7444,
1803 https://doi.org/10.1029/2019jb017467.

1804 Soucy La Roche, R., Godin, L., Cottle, J. M., and Kellett, D. A., 2018, Preservation of the Early
1805 Evolution of the Himalayan Middle Crust in Foreland Klippen: Insights from the Karnali
1806 Klippe, West Nepal: Tectonics, v. 37, no. 5, p. 1161-1193,
1807 https://doi.org/10.1002/2017tc004847.

1808 Sreejith, K. M., Sunil, P. S., Agrawal, R., Saji, A. P., Rajawat, A. S., and Ramesh, D. S., 2018,
1809 Audit of stored strain energy and extent of future earthquake rupture in central Himalaya:
1810 Scientific Reports, v. 8, no. 1, p. 16697, https://doi.org/10.1038/s41598-018-35025-y.

1811 Srivastava, P., and Mitra, G., 1994, Thrust geometries and deep structure of the outer and lesser
1812 Himalaya, Kumaon and Garhwal (India): Implications for evolution of the Himalayan
1813 fold-and-thrust belt: Tectonics, v. 13, no. 1, p. 89-109,
1814 https://doi.org/10.1029/93TC01130.

1815 Stevens, V. L., and Avouac, J. P., 2015, Interseismic coupling on the main Himalayan thrust:
1816 Geophysical Research Letters, v. 42, no. 14, p. 5828-5837,
1817 https://doi.org/10.1002/2015GL064845.

1818 Stübner, K., Grujic, D., Dunkl, I., Thiede, R., and Eugster, P., 2018, Pliocene episodic
1819 exhumation and the significance of the Munsiari thrust in the northwestern Himalaya:
1820 Earth and Planetary Science Letters, v. 481, p. 273-283,
1821 https://doi.org/10.1016/j.epsl.2017.10.036.

1822 Subedi, S., Hetényi, G., Vergne, J., Bollinger, L., Lyon-Caen, H., Farra, V., Adhikari, L. B., and
1823 Gupta, R. M., 2018, Imaging the Moho and the Main Himalayan Thrust in Western Nepal
1824 With Receiver Functions: Geophysical Research Letters, v. 45, no. 24, p. 13222-13230,
1825 https://doi.org/10.1029/2018GL080911.

1826 Suppe, J., 1983, Geometry and kinematics of fault-bend folding: American Journal of Science, v.
1827 283, no. 7, p. 684-721, https://doi.org/10.2475/ajs.283.7.684.

1828 Szulc, A. G., Najman, Y., Sinclair, H. D., Pringle, M., Bickle, M., Chapman, H., Garzanti, E.,
1829 Andò, S., Huyghe, P., Mugnier, J. L., Ojha, T., and DeCelles, P., 2006, Tectonic
1830 evolution of the Himalaya constrained by detrital 40Ar–39Ar, Sm–Nd and petrographic
1831 data from the Siwalik foreland basin succession, SW Nepal: Basin Research, v. 18, no. 4,
1832 p. 375-391, https://doi.org/10.1111/j.1365-2117.2006.00307.x.

1833 Taylor, M., Forte, A., Laskowski, A., and Ding, L., 2021, Active Uplift of Southern Tibet
1834 Revealed: GSA Today, v. 31, no. 8, p. 4-10, https://doi.org/10.1130/gsatg487a.1.

1835 Thiede, R., Robert, X., Stubner, K., Dey, S., and Faruhn, J., 2017, Sustained out-of-sequence
1836 shortening along a tectonically active segment of the Main Boundary thrust: The
1837 Dhauladhar Range in the northwestern Himalaya: Lithosphere, v. 9, no. 5, p. 715-725,
1838 https://doi.org/10.1130/L630.1.

1839 Thiede, R. C., Arrowsmith, J. R., Bookhagen, B., McWilliams, M. O., Sobel, E. R., and Strecker,
1840 M. R., 2005, From tectonically to erosionally controlled development of the Himalayan
1841 orogen: Geology, v. 33, no. 8, p. 689-692, https://doi.org/10.1130/G21483.1.

1842 Thiede, R. C., Bookhagen, B., Arrowsmith, J. R., Sobel, E. R., and Strecker, M. R., 2004,
1843 Climatic control on rapid exhumation along the Southern Himalayan Front: Earth and
1844 Planetary Science Letters, v. 222, no. 3-4, p. 791-806,
1845 https://doi.org/10.1016/j.epsl.2004.03.015.

1846 Thiede, R. C., and Ehlers, T. A., 2013, Large spatial and temporal variations in Himalayan
1847 denudation: Earth and Planetary Science Letters, v. 371–372, p. 278-293,
1848 https://doi.org/10.1016/j.epsl.2013.03.004.

1849 Thiede, R. C., Ehlers, T. A., Bookhagen, B., and Strecker, M. R., 2009, Erosional variability
1850 along the northwest Himalaya: Journal of Geophysical Research-Earth Surface, v. 114,
1851 no. F1, https://doi.org/10.1029/2008jf001010.

van der Beek, P., Litty, C., Baudin, M., Mercier, J., Robert, X., and Hardwick, E., 2016, Contrasting tectonically driven exhumation and incision patterns, western versus central Nepal Himalaya: Geology, v. 44, no. 4, p. 327-330, https://doi.org/10.1130/g37579.1.

van der Beek, P., Robert, X., Mugnier, J.-L., Bernet, M., Huyghe, P., and Labrin, E., 2006, Late Miocene – Recent exhumation of the central Himalaya and recycling in the foreland basin assessed by apatite fission-track thermochronology of Siwalik sediments, Nepal: Basin Research, v. 18, no. 4, p. 413-434, https://doi.org/10.1111/j.1365-2117.2006.00305.x.

Vance, D., Bickle, M., Ivy-Ochs, S., and Kubik, P. W., 2003, Erosion and exhumation in the Himalaya from cosmogenic isotope inventories of river sediments: Earth and Planetary Science Letters, v. 206, no. 3-4, p. 273-288, https://doi.org/10.1016/s0012-821x(02)01102-0.

Vannay, J. C., and Hodges, K. V., 1996, Tectonometamorphic evolution of the Himalayan metamorphic core between the Annapurna and Dhaulagiri, central Nepal: Journal of Metamorphic Geology, v. 14, no. 5, p. 635-656, https://doi.org/10.1046/j.1525-1314.1996.00426.x.

Wang, A., Garver, J. I., Wang, G., Smith, J. A., and Zhang, K., 2010, Episodic exhumation of the Greater Himalayan Sequence since the Miocene constrained by fission track thermochronology in Nyalam, central Himalaya: Tectonophysics, v. 495, no. 3–4, p. 315-323, https://doi.org/10.1016/j.tecto.2010.09.037.

Wang, C., Gao, R., Yin, A., Wang, H., Zhang, Y., Guo, T., Li, Q., and Li, Y., 2011, A mid-crustal strain-transfer model for continental deformation: A new perspective from high-resolution deep seismic-reflection profiling across NE Tibet: Earth and Planetary Science Letters, v. 306, no. 3, p. 279-288, https://doi.org/10.1016/j.epsl.2011.04.010.

Wang, X., Wei, S., and Wu, W., 2017, Double-ramp on the Main Himalayan Thrust revealed by broadband waveform modeling of the 2015 Gorkha earthquake sequence: Earth and Planetary Science Letters, v. 473, no. Supplement C, p. 83-93, https://doi.org/10.1016/j.epsl.2017.05.032.

Wang, Y., Day, S. M., and Denolle, M. A., 2019, Geometric Controls on Pulse-Like Rupture in a Dynamic Model of the 2015 Gorkha Earthquake: Journal of Geophysical Research: Solid Earth, v. 0, no. 0, https://doi.org/10.1029/2018JB016602.

Webb, A. A. G., 2013, Preliminary balanced palinspastic reconstruction of Cenozoic deformation across the Himachal Himalaya (northwestern India): Geosphere, v. 9, no. 3, p. 572-587, https://doi.org/10.1130/Ges00787.1.

Webb, A. A. G., Guo, H., Clift, P. D., Husson, L., Müller, T., Costantino, D., Yin, A., Xu, Z., Cao, H., and Wang, Q., 2017, The Himalaya in 3D: Slab dynamics controlled mountain building and monsoon intensification: Lithosphere, v. 9, no. 4, p. 637-651, https://doi.org/10.1130/l636.1.

Whipp, D. M., Ehlers, T. A., Blythe, A. E., Huntington, K. W., Hodges, K. V., and Burbank, D. W., 2007, Plio-Quaternary exhumation history of the central Nepalese Himalaya: 2. Thermokinematic and thermochronometer age prediction model: Tectonics, v. 26, no. 3, p. n/a-n/a, https://doi.org/10.1029/2006TC001991.

1894 Whipple, K. X., Shirzaei, M., Hodges, K. V., and Ramon Arrowsmith, J., 2016, Active
1895 shortening within the Himalayan orogenic wedge implied by the 2015 Gorkha
1896 earthquake: Nature Geoscience, v. 9, no. 9, p. 711-716, https://doi.org/10.1038/ngeo2797.

1897 Williams, C. A., Connors, C., Dahlen, F. A., Price, E. J., and Suppe, J., 1994, Effect of the
1898 brittle-ductile transition on the topography of compressive mountain belts on Earth and
1899 Venus: Journal of Geophysical Research: Solid Earth, v. 99, no. B10, p. 19947-19974,
1900 https://doi.org/10.1029/94jb01407.

1901 Wissinger, E. S., Levander, A., and Christensen, N. I., 1997, Seismic images of crustal duplexing
1902 and continental subduction in the Brooks Range: Journal of Geophysical Research: Solid
1903 Earth, v. 102, no. B9, p. 20847-20871, https://doi.org/10.1029/96jb03662.

1904 Wobus, C., Heimsath, A., Whipple, K., and Hodges, K., 2005, Active out-of-sequence thrust
1905 faulting in the central Nepalese Himalaya: Nature, v. 434, no. 7036, p. 1008-1011.

1906 Wobus, C. W., Hodges, K. V., and Whipple, K. X., 2003, Has focused denudation sustained
1907 active thrusting at the Himalayan topographic front?: Geology, v. 31, no. 10, p. 861-864,
1908 https://doi.org/10.1130/g19730.1.

1909 Wobus, C. W., Whipple, K. X., and Hodges, K. V., 2006, Neotectonics of the central Nepalese
1910 Himalaya: Constraints from geomorphology, detrital40Ar/39Ar thermochronology, and
1911 thermal modeling: Tectonics, v. 25, no. 4, p. n/a-n/a,
1912 https://doi.org/10.1029/2005tc001935.

1913 Xu, Q., Zhao, J., Yuan, X., Liu, H., and Pei, S., 2017, Detailed Configuration of the
1914 Underthrusting Indian Lithosphere Beneath Western Tibet Revealed by Receiver
1915 Function Images: Journal of Geophysical Research: Solid Earth, v. 122, no. 10, p. 8257-
1916 8269, https://doi.org/10.1002/2017jb014490.

1917 Yadav, R. K., Gahalaut, V. K., Bansal, A. K., Sati, S. P., Catherine, J., Gautam, P., Kumar, K.,
1918 and Rana, N., 2019, Strong seismic coupling underneath Garhwal–Kumaun region, NW
1919 Himalaya, India: Earth and Planetary Science Letters, v. 506, p. 8-14,
1920 https://doi.org/10.1016/j.epsl.2018.10.023.

1921 Yin, A., 2006, Cenozoic tectonic evolution of the Himalayan orogen as constrained by along-
1922 strike variation of structural geometry, exhumation history, and foreland sedimentation:
1923 Earth-Science Reviews, v. 76, no. 1-2, p. 1-131,
1924 https://doi.org/10.1016/j.earscirev.2005.05.004.

1925 Zhang, Y., Wang, R., Walter, T. R., Feng, W., Chen, Y., and Huang, Q., 2017, Significant lateral
1926 dip changes may have limited the scale of the 2015 Mw 7.8 Gorkha earthquake:
1927 Geophysical Research Letters, v. 44, no. 17, p. 8847-8856,
1928 https://doi.org/10.1002/2017GL074095.

1929 Zuza, A. V., Wu, C., Wang, Z., Levy, D. A., Li, B., Xiong, X., and Chen, X., 2018,
1930 Underthrusting and duplexing beneath the northern Tibetan Plateau and the evolution of
1931 the Himalayan-Tibetan orogen: Lithosphere, v. 11, no. 2, p. 209-231,
1932 https://doi.org/10.1130/l1042.1.

1933